

University of Kentucky

UKnowledge

Theses and Dissertations--Chemistry

Chemistry

2023

SURFACE MODIFICATION OF CARBON-BASED ELECTRODES FOR ELECTROCHEMICAL CONVERSION PROCESSES: OXYGEN REDUCTION REACTION AND BICARBONATE CONVERSION

Udari Shyamika Kodithuwakku Arachchige

University of Kentucky, Lexington, kaushyamika@gmail.com

Author ORCID Identifier:

 <https://orcid.org/0000-0003-1954-5943>

Digital Object Identifier: <https://doi.org/10.13023/etd.2023.017>

[Right click to open a feedback form in a new tab to let us know how this document benefits you.](#)

Recommended Citation

Kodithuwakku Arachchige, Udari Shyamika, "SURFACE MODIFICATION OF CARBON-BASED ELECTRODES FOR ELECTROCHEMICAL CONVERSION PROCESSES: OXYGEN REDUCTION REACTION AND BICARBONATE CONVERSION" (2023). *Theses and Dissertations--Chemistry*. 175. https://uknowledge.uky.edu/chemistry_etds/175

This Doctoral Dissertation is brought to you for free and open access by the Chemistry at UKnowledge. It has been accepted for inclusion in Theses and Dissertations--Chemistry by an authorized administrator of UKnowledge. For more information, please contact UKnowledge@lsv.uky.edu.

STUDENT AGREEMENT:

I represent that my thesis or dissertation and abstract are my original work. Proper attribution has been given to all outside sources. I understand that I am solely responsible for obtaining any needed copyright permissions. I have obtained needed written permission statement(s) from the owner(s) of each third-party copyrighted matter to be included in my work, allowing electronic distribution (if such use is not permitted by the fair use doctrine) which will be submitted to UKnowledge as Additional File.

I hereby grant to The University of Kentucky and its agents the irrevocable, non-exclusive, and royalty-free license to archive and make accessible my work in whole or in part in all forms of media, now or hereafter known. I agree that the document mentioned above may be made available immediately for worldwide access unless an embargo applies.

I retain all other ownership rights to the copyright of my work. I also retain the right to use in future works (such as articles or books) all or part of my work. I understand that I am free to register the copyright to my work.

REVIEW, APPROVAL AND ACCEPTANCE

The document mentioned above has been reviewed and accepted by the student's advisor, on behalf of the advisory committee, and by the Director of Graduate Studies (DGS), on behalf of the program; we verify that this is the final, approved version of the student's thesis including all changes required by the advisory committee. The undersigned agree to abide by the statements above.

Udari Shyamika Kodithuwakku Arachchige, Student

Dr. Doo Young Kim, Major Professor

Dr. Dong-Sheng Yang, Director of Graduate Studies

SURFACE MODIFICATION OF CARBON-BASED ELECTRODES FOR
ELECTROCHEMICAL CONVERSION PROCESSES: OXYGEN REDUCTION
REACTION AND BICARBONATE CONVERSION

DISSERTATION

A dissertation submitted in partial fulfillment of the
requirements for the degree of Doctor of Philosophy in the
College of Art and Sciences
at the University of Kentucky

By
Udari Kodithuwakku
Lexington, Kentucky
Director: Dr. Doo Young Kim, Professor of Chemistry
Lexington, Kentucky
2022

Copyright © Udari Kodithuwakku 2022
<https://orcid.org/0000-0003-1954-5943>

ABSTRACT OF DISSERTATION

SURFACE MODIFICATION OF CARBON-BASED ELECTRODES FOR ELECTROCHEMICAL CONVERSION PROCESSES: OXYGEN REDUCTION REACTION AND BICARBONATE CONVERSION

Oxygen reduction reaction (ORR) and conversion of bicarbonate into value-added chemicals are two significant electrochemical processes for energy storage and conversion. ORR is an important electrochemical reaction in fuel cells and metal-air batteries that provide power conversion and storage capacity, respectively, for portable electronics, and electric vehicles. However, the performance of catalysts (e.g., platinum-based) is critically limited by slow kinetics, inefficient four-electron pathway, and surface deactivation. This limited performance of platinum-based catalysts, the scarcity of platinum, and vulnerable supply chains for critical minerals require the development of alternative electrocatalysts now more than ever.

Carbon-based materials possess several key properties that are beneficial for catalytic applications such as high electrical conductivity, large surface area, inert electrode surface, and low cost. The catalytic activity of carbon-based electrodes can be promoted by tailoring the surface and structure through the incorporation of heteroatom dopants. Chapters 2 and 3 in this dissertation focus on the synthesis of electrocatalysts and their surface modification to achieve effective ORR performance in alkaline media. Chapter 2 narrates ORR performance of nitrogen (N) and boron (B) co-doped carbon nano onions (CNOs). In this work, annealing temperature was found to be a crucial factor in the synergistic benefit of N and B towards ORR. X-ray photoelectron spectroscopy (XPS), Raman analysis, and high-resolution scanning transmission electron microscopy were conducted to elucidate the role of N-B configurations in promoting ORR activity. Chapter 3 focuses on copper nanoparticles supported by nitrogen-doped CNOs. This chapter discusses the impacts of nitrogen heteroatom and copper nanoparticles on ORR performance.

In chapter 4, electrocatalytic carbon dioxide (CO₂) reduction (CO₂RR) in a membrane electrode assembly was investigated. Atmospheric CO₂ has significantly increased in the last two decades. Since CO₂ is a primary greenhouse gas emitted on earth, it is imperative to suppress the concentration of emitted CO₂. While the regulation of CO₂ emissions is critical, CO₂ capture and storage (CCS), and biological, chemical, and electrochemical conversions are promising approaches to reduce atmospheric CO₂

concentration. In electrochemical conversion, a common method employs the feed of high-purity compressed CO₂ gas into an electrolyzer. This method, however, is not economically viable because it requires the release and/or pressurization of CO₂ from captured CO₂ solution, which is energy-intensive. To resolve this issue, aqueous carbonate/bicarbonate (CO₃²⁻/HCO₃⁻) transported from the upstream carbon capture process can be directly fed into an electrolyzer. We demonstrated that a cation exchange membrane coated with a thin copper film can efficiently convert bicarbonate to C1-C2 products such as formic acid and acetic acid. Both liquid and gas products were quantified by using proton nuclear magnetic resonance (1H NMR) and gas chromatography, respectively.

The studies herein highlight the importance of structural modification of catalysts, surface chemistry, and membrane-electrode interface to improve the efficiency and selectivity of ORR and CO₂RR processes.

KEYWORDS: Oxygen reduction reaction, Heteroatom Doping, Copper, (Bi)carbonate Conversion, XPS, Solvothermal

Udari Kodithuwakku

(Name of Student)

11/07/2022

Date

SURFACE MODIFICATION OF CARBON-BASED ELECTRODES FOR
ELECTROCHEMICAL CONVERSION PROCESSES: OXYGEN REDUCTION
REACTION AND BICARBONATE CONVERSION

By
Udari Kodithuwakku

Dr. Doo Young Kim

Director of Dissertation

Dr. Dong Sheng Yang

Director of Graduate Studies

11/07/2022

Date

DEDICATION

To my parents, husband, daughter, my sister, and brothers.

ACKNOWLEDGMENTS

In reflecting on the process of creating this dissertation, I conducted my research work under the guidance of Prof. Doo Young Kim at the Department of Chemistry in the University of Kentucky. This work is funded by KY NSF EPSCoR RII Track1 (Cooperative Agreement No. 1355438), KY NASA EPSCoR RIDG, NASA Award No. 80NSSC19M0052, and NASA EPSCoR R3, NASA Award No. 80NSSC20M0139. First and foremost, I would like to thank my advisor Prof. Doo Young Kim, for his guidance and feedback to shape my research work into unique projects. Also, his perspectives and guidance have helped me to gain confidence in myself to be an independent researcher throughout my Ph.D. program. I would have never become the scholar I am today without your guidance. This Ph.D. journey is not possible without my committee members, Prof. Dong-Sheng Yang, Prof. Jason DeRouchey, and Prof. Yang-Tse Cheng, thank you for your support and guidance throughout these years.

I also want to thank my collaborators who immensely supported me to add a value to my work. Prof. Beth Guiton and Dr. Melonie Thomas, thank you for your assistance on electron microscopy. Prof. Yang-Tse Cheng and Jacob Hemple, I am grateful for your support of Kelvin probe measurements. I specially need to thank, Prof. Anne-Frances Miller and all fellows for their support in analyzing the NMR. I also appreciate Dr. Dali Qian, Dr. Nicolas, and Jillian Cramer for their assistance and support on XPS and electron microscopy analysis. Furthermore, I thank the Center of Applied Materials at the Department of Physics on XRD, and sputtering experiments.

I also want to thank the teaching supervisors, Dr. Allison Soult, Dr Lisa Blue, Dr April French, and Dr. Manjari Patwardan, for their support in teaching tasks over the

past few years. Also, I could not succeed as a TA without the support of all lab assistants, specially, Ms. Stacy Hinchey and all TAs and lead TAs. Their support helped me gain experience and develop my personal skills so that I could become a competent person.

Moreover, I would like to thank the department managers in the Department of Chemistry. Mr. Daniel Whittaker, Ms. Jenny Owen, Ms. Christine Smothers, Ms. Emily Cheathan, and Ms. Christine Morgan for creating a friendly and supportive environment throughout the past few years. I also thank Steven Maynard for supporting me to design flow plates for the electrolyzer. Also, Arthur Sebesta, I want to thank you for hard work in helping to repair everything. I would like to thank Jeff Babbitt for creating a glassware to design my electrochemical cell.

I would also like to thank my colleagues in my lab for sharing discussions, assisting with measurements and experiments, and providing moral support throughout the year. I would especially like to thank Dr. Namal Wanninayake for initially training me in catalyst preparation, material characterization and electrolyzer operation. I also want to thank Dr. Rosemary Calabro for encouraging me throughout the initial phase of my research. Moreover, I am grateful to work in the lab with the present members Nadeesha Kothalwala and Prakhar Sharma. They always created a friendly and supportive work environment in the last few years to achieve our group's objectives.

This work could have never been completed without the support of my amazing family. I have no words to express my gratitude to my husband, Gayan Karunasinghe for being my strength in every challenging situation we have encountered. You constantly motivate and encourage me with your attention and affection to paint my

future goals. You have been a blessing in my life. I am extremely grateful to have my wonderful little daughter, Dahamdi Alicia Karunasinghe. Since you were a baby, you have been so kind and understanding of your parents' busy lives. Thank you for your patience and for keeping me happy for the last 5 years. Last but not least, I must express my very profound gratitude to my parents, Kulathilake Kodithuwakku, Ranjanie Muhandiram, and my siblings for providing me with enduring support and continuous encouragement throughout my years of study. I am truly thankful for your love and support.

TABLE OF CONTENTS

| | |
|---|-----|
| ACKNOWLEDGMENTS | iii |
| LIST OF TABLES | ix |
| LIST OF FIGURES | x |
| LIST OF ABBREVIATIONS | xv |
| CHAPTER 1. INTRODUCTION AND LITERATURE REVIEW | 17 |
| 1.1 Background..... | 17 |
| 1.2 Electrocatalysis | 19 |
| 1.2.1 Sabatier principle for electrocatalysis..... | 20 |
| 1.3 Electrochemical reactions | 21 |
| 1.3.1 Thermodynamics and potentials of the cells..... | 22 |
| 1.3.2 Kinetics of the reactions..... | 23 |
| 1.3.3 Effects of mass transfer..... | 25 |
| 1.4 Importance of ORR in fuel cells..... | 27 |
| 1.4.1 Platinum-based ORR electrocatalysts..... | 28 |
| 1.4.2 Heteroatom doped carbon materials | 30 |
| 1.4.3 Relevance of CO ₂ capturing and energy conversion | 32 |
| 1.5 Organization of this dissertation..... | 34 |
| CHAPTER 2. SYNERGISTIC INTERACTION OF EDGE NITROGEN AND BORON DOPANTS IN CARBON NANO ONIONS FOR EFFICIENT OXYGEN REDUCTION REACTION | 37 |
| 2.1 Introduction..... | 37 |
| 2.2 Experimental..... | 39 |
| 2.2.1 Chemical oxidation of CNOs..... | 39 |
| 2.2.2 Synthesis of nitrogen doped CNOs (N-CNO) | 39 |
| 2.2.3 Synthesis of nitrogen (N) and boron (B) co-doped CNOs (NB-CNO)..... | 40 |

| | | |
|--|--|----|
| 2.3 | Material characterization | 41 |
| 2.4 | Electrochemical measurements..... | 41 |
| 2.4.1 | Preparation of a rotating ring disk electrode (RRDE) | 41 |
| 2.4.2 | Electrochemical performance test..... | 42 |
| 2.5 | Results and discussion | 42 |
| 2.6 | Conclusion | 56 |
| 2.7 | Acknowledgements..... | 57 |
| 2.8 | Supporting information..... | 57 |
| 2.8.1 | Raman analysis | 57 |
| 2.8.2 | X-ray diffraction | 59 |
| 2.8.3 | Electrochemical measurement | 60 |
| | | |
| CHAPTER 3. COPPER NANOPARTICLES SUPPORTED ON NITROGEN DOPED CARBON NANO-ONIONS FOR OXYGEN REDUCTION REACTION: SYNERGISTIC EFFECTS OF NITROGEN AND CARBON NANO-ONIONS..... | | |
| | | 67 |
| 3.1 | Introduction..... | 67 |
| 3.2 | Experimental..... | 69 |
| 3.2.1 | Synthesis of CNO, Ox-CNO, and N-CNO | 69 |
| 3.2.2 | Synthesis of Cu-NCNO (Cu-NCNO)..... | 70 |
| 3.2.3 | Material characterization | 71 |
| 3.2.3.1 | Electrochemical measurements..... | 71 |
| 3.3 | Results and discussion | 73 |
| 3.4 | Conclusion | 83 |
| 3.5 | Supporting information..... | 84 |
| 3.5.1 | XRD analysis | 84 |
| 3.5.2 | Raman analysis | 84 |
| 3.5.3 | Kelvin probe force microscopy measurements..... | 85 |

| | |
|--|-----|
| CHAPTER 4. COPPER-CATALYZED ELECTROCHEMICAL CONVERSION OF BICARBONATE FEEDSTOCK TO ACETATE AND FORMATE IN A FLOW-TYPE ELECTROLYZER..... | 94 |
| 4.1 Introduction..... | 94 |
| 4.2 Results and discussion | 97 |
| 4.3 Conclusion | 105 |
| 4.4 Supporting information..... | 105 |
| 4.4.1 Experimental methods | 105 |
| 4.4.1.1 Preparation of Cu catalyst..... | 105 |
| 4.4.1.2 Preparation of Pt/C anode electrode | 106 |
| 4.4.1.3 Flow cell setup | 106 |
| 4.4.1.4 Electrochemical test and electrolysis | 107 |
| 4.4.1.5 Product quantification..... | 108 |
| 4.4.1.5.1 NMR analysis for liquid products..... | 108 |
| 4.4.1.5.2 Gas chromatography for gas sample analysis..... | 109 |
| 4.4.1.6 Material characterization | 110 |
| 4.4.1.6.1 Scanning electron microscopy (SEM) | 110 |
| 4.4.1.6.2 X-ray Diffraction (XRD) analysis | 111 |
| 4.4.1.6.3 X-ray photoelectron spectroscopy (XPS) | 111 |
| CHAPTER 5. CONCLUSION AND FUTURE DIRECTIONS..... | 116 |
| APPENDIX..... | 120 |
| REFERENCES | 124 |
| VITA..... | 136 |

LIST OF TABLES

| | |
|--|-----|
| Table 1.1 Electrochemical Reactions and Corresponding ΔG° in an aqueous solution. ^{14, 15} | 23 |
| Table 2.1 ORR performance of various N and B doped samples. | 55 |
| Table S2.1 The summary of Raman analysis | 59 |
| Table S2.2 The atomic percentages of C, O, N. | 62 |
| Table S2.3 XPS N1s related chemical states in the samples. | 62 |
| Table S2.4 XPS B1s related chemical states in the samples. | 63 |
| Table S3.1 Summary of the XPS survey of all catalysts. | 86 |
| Table S3.2 Summary of the XPS high resolution spectra % Area of N1s and Cu2p for NCNO (700), Cu-NCNO-BF, and Cu-NCNO-AF. | 86 |
| Table S3.3 ORR parameters for recently reported Cu based nitrogen doped graphene-based catalysts in alkaline electrolyte. | 87 |
| Table 4.1 Comparison of previous reports and current study on the conversion of bicarbonate/ CO_2 to acetate and formate. | 104 |

LIST OF FIGURES

| | | |
|------------|---|----|
| Figure 1.1 | Transportation emissions of the United State. ² | 17 |
| Figure 1.2 | Global energy consumption by energy source (2010-2050). ³ | 18 |
| Figure 1.3 | Effect of catalyst on potential energy profile. ⁵ | 19 |
| Figure 1.4 | (a) A schematic representation of the qualitative Sabatier principle (b) illustration of the reaction of two molecules (green and orange balls) and its steps. ⁹ | 20 |
| Figure 1.5 | A pathway of the general electrode reactions. ¹¹ | 21 |
| Figure 1.6 | Modes of mass transfer. ²⁰ | 26 |
| Figure 1.7 | Representation of N species in N-doped carbon materials and their XPS binding energies. ³⁵ | 31 |
| Figure 1.8 | Various prototype systems for CO ₂ capturing and converting into valuable products. (The pink arrow represents the bicarbonate conversion process). ⁴³ | 33 |
| Figure 2.1 | Synthetic procedure of CNOs, N-CNO(700) and NB-CNO(X). | 43 |
| Figure 2.2 | (a-c) STEM HAADF micrographs of NB-CNO (700) showing a series of magnified images of the area in yellow square regions in each image, and (d) is the Fourier filtered image of (c) with improved signal-to-noise ratio for enhanced clarity. (e) shows the intensity line-scan profile of the HAADF image across the atoms indicated by the blue dashed rectangle in (d) where the atoms are well in focus. The intensity profile suggests that given the intensity ratios of the highlighted atoms, they are most likely to be N, C, and B as marked in image (e). | 47 |
| Figure 2.3 | High resolution XPS spectra and deconvolutions of (a) N 1s and (b) B 1s in N-CNO(700) and co-doped NB-CNO samples. Total quantities and percentages of (c) N 1s and (d) B 1s. | 48 |

| | |
|---|----|
| Figure 2.4 Peak shift of B1s binding energy in B-O, B-N, and B-C-N configurations of NB-CNO samples. (b) Proposed chemical structures of B-N and B-C-N at low and high B doping temperatures. | 50 |
| Figure 2.5 (a) electron transfer numbers (top), ring currents (middle), and ORR current densities (bottom) for catalysts determined by RRDE experiments and (b) the summary of onset potentials and limiting current densities (at -0.5 V vs. Ag/AgCl). | 54 |
| Figure 2.6 (a) Long-term stability for 6 hours and (b) electrode response upon the addition of methanol (2.5 % v/v) while -0.25 V vs. Ag/AgCl was applied. | 56 |
| Figure S2.1 Raman spectra of CNOs, Ox-CNO, N-CNO(700), NB-CNO(600-1000). | 61 |
| Figure S2.2 (a) I2D/IG ratio, (b) 2D band shift, and (c) G band shift. | 62 |
| Figure S2.3 (a) X-ray diffraction patterns and (b) zoomed-in (002) peak of CNOs, N-CNO(700) and all NB-CNO samples. | 62 |
| Figure S2.4 (a-b) Low-magnification STEM HAADF micrographs of NB-CNO (700). (c-e) High-magnification STEM HAADF micrographs and their respective Fourier filtered images of NB-CNO (700), NB-CNO (800), and NB-CNO (900), respectively. | 63 |
| Figure S2.5 (a) Results of RRDE measurement and (b) comparison of onset potentials and limiting current densities (at -0.5 V vs. Ag/AgCl) of all samples. | 64 |
| Figure 3.1 A schematic illustration of Cu-NCNO synthetic procedure (gray, carbon; blue, nitrogen; orange, copper). | 73 |
| Figure 3.2 (a) HR-TEM image (b) HAADF-STEM image (yellow square represent the selected area for the EDS) (c) EDS mapping of nitrogen and Cu, and (d) EDS spectrum for elemental analysis. | 75 |
| Figure 3.3 High resolution XPS spectra of (a) N1s, (b) Cu2p. | 76 |

| | |
|--|----|
| Figure 3.4 ORR performance of the Cu-NCNO, NCNO and Pt/C (a) CV curves of the Cu-NCNO catalyst in N ₂ - and O ₂ -saturated 0.1 M KOH electrolyte, (b) RRDE for Cu-NCNO, NCNO, and Pt/C before acid washed at rotation rate 1600 rpm (scan rate 5 mV/s), (onset potentials are -0.08,-0.15, 0.03, -0.2 V for Cu-NCNO-BF, NCNO, Pt/C, and Cu-CNO-BF, respectively at -0.3 mA cm ⁻²), (c) electron transfer number, (d) Tafel plots of Cu-NCNO-BF and Pt/C catalysts (J _k is kinetic current density). | 79 |
| Figure 3.5 RRDE at 1600 rpm for Cu-NCNO and Pt/C (a) durability test (b) methanol tolerance test. | 79 |
| Figure 3.6 AM-KPFM images of individual doped CNO clumps. (a-c) Topography images showing the height of each catalyst, NCNO, Cu-CNO and Cu-NCNO, respectively. (d-f) Contact potential difference images of the doped CNO clumps. The inset scale bars in images (a-c, d) | 80 |
| Figure S3.1 XRD patterns for (a) Cu-CNO-BF, (b) Cu-NCNO-BF, (c) Cu reference peaks. ¹³³ | 88 |
| Figure S3.2 XPS survey scans. | 89 |
| Figure S3.3 Raman Spectra of CNO, NCNO, Cu-NCNO-BF, and Cu-NCNO-AF. | 89 |
| Figure S3.4 TGA of Cu-NCNO and Cu-CNO before acid washing. | 90 |
| Figure S3.5 CV curve of NCNO in O ₂ -saturated 0.1 M KOH. | 90 |
| Figure S3.6 LSV curves (a) Pt/C, (b) NCNO, and (c) Cu-NCNO-BF catalyst obtained at different rotating rates (scan rate = 5 mV/s). (d) K-L plots of current density reciprocal (J ⁻¹) versus ω ^{-1/2} at different potentials on Cu-NCNO-BF electrode. | 89 |
| Figure S3.7 RRDE (a) Pt/C, (b) NCNO, and (c) Cu-NCNO catalyst obtained at 1600 rpm rotating rate (scan rate = 5 mV/s). | 92 |

| | | |
|-------------|--|-----|
| Figure S3.8 | AM-KPFM images of Cu-NCNO-BF and Cu-CNO-BF clumps. (a,b) Topography images showing the height of each catalyst, Cu-CNO and Cu-NCNO, respectively. (c,d) Contact potential difference images of the doped CNO clumps. | 93 |
| Figure S3.9 | Block diagram of general KPFM system. | 93 |
| Figure 4.1 | (a) A flow diagram that shows parallel pathways of (i) CO ₂ electrolysis following CO ₂ capture and (ii) bicarbonate electrolysis. (b) the expanded view of a bicarbonate electrolyzer. Expanded flow design for the bicarbonate conversion into products. (c) the photographs of (i) titanium flow field (cathode), (ii) stainless-steel flow field (anode), (iii) Pt/C anode, (iv) Cu cathode, (v) cation exchange membrane (CEM). | 97 |
| Figure 4.2 | (a) A schematic of the bicarbonate electrolyzer, peristaltic pump, and the flow of the reactants and products. The peristaltic pump delivers both 1M KHCO ₃ and 1M KOH at 15 sccm through the cathode flow plate to Cu catalyst and anode flow plate to the anode catalyst, respectively. (b) Diagrammatic representation of the electrolysis process in the electrolyzer. The experimental set up and the workstation have shown in Figure S4.1. | 99 |
| Figure 4.3 | (a) Chronoamperometric curves recorded at fixed potentials under the flow of Ar in 1 M KHCO ₃ , (b) The FE's of H ₂ , formate, and acetate determined from GC and NMR analysis. | 101 |
| Figure 4.4 | Possible mechanism to form acetic acid and formate during the bicarbonate electrolysis. | 103 |
| Figure S4.1 | Experimental setup in the electrochemical workstation. | 111 |

| | |
|---|-----|
| Figure S4.2 SEM images (a) carbon support (b) after Cu deposition on the carbon support. | 111 |
| Figure S4.3 X-ray diffractograms of Cu/C electrocatalyst and the carbon support (control). | 112 |
| Figure S4.4 (a) XPS survey spectrum of Cu/C (b) high resolution Cu2p spectrum. | 112 |
| Figure S4.5 LSVs for Cu/C before and after electrolysis. | 113 |
| Figure S4.6 ¹ H-NMR spectrum of catholyte after electrolysis at -2V for 1 hour. Phenol and DMSO are internal standard. Anolyte 1M KOH and catholyte 1M KHCO ₃ | 113 |

LIST OF ABBREVIATIONS

| | |
|--------------------|---|
| ORR | Oxygen reduction reaction |
| CO ₂ RR | Carbon dioxide reduction reaction |
| HOR | Hydrogen oxidation reaction |
| GHG | Greenhouse gases |
| B-V Equation | Butler-Volmer Equation |
| PEMFCs | Proton exchange membrane fuel cells |
| MAB | Metal-air batteries |
| RRDE | Rotating ring disk electrode |
| CNOs | Carbon nano onions |
| p-CNO | Pristine carbon nano onions |
| Ox-CNO | Oxidized carbon nano onions |
| NCNO | Nitrogen doped carbon nano onions |
| NB-CNO | Nitrogen, boron doped carbon nano onions |
| ND | Nano diamonds |
| PGM | Platinum group metals |
| XPS | X-ray photoelectron spectroscopy |
| XRD | X-ray diffraction |
| SEM | Scanning electron microscopy |
| EDS | Energy dispersive spectroscopy |
| TEM | Transmission electron microscopy |
| STEM | Scanning transmission electron microscopy |
| HAADF | High angle annular dark field |
| HR-TEM | High resolution TEM |
| TGA | Thermogravimetric analysis |
| KPFM | Kelvin probe force microscopy |
| AM-KPFM | Amplitude modulated KPFM |
| ¹ H-NMR | Proton nuclear magnetic resonance |
| GC | Gas chromatography |
| FID | Flame ionization detector |

| | |
|-----|-------------------------------|
| TCD | Thermal conductivity detector |
| CV | Cyclic voltammetry |
| CA | Chronoamperometry |
| LSV | Linear sweep voltammetry |
| RE | Reference electrode |
| CE | Counter electrode |
| WE | Working electrode |
| FE | Faradaic efficiency |
| RHE | Reversible hydrogen electrode |
| BPM | Bipolar membrane |
| AEM | Anion exchange membrane |
| CEM | Cation exchange membrane |
| MEA | Membrane electrode assembly |
| GDE | Gas diffusion electrode |
| GDL | Gas diffusion layer |

CHAPTER 1. INTRODUCTION AND LITERATURE REVIEW

1.1 Background

In modern society, energy production is heavily based on burning fossil fuels such as coal, oil, and natural gas. As a consequence, limited supply of fossil fuels and human-induced climate change are the biggest challenges confronting everyone today.¹ Among the various sources for human-induced greenhouse gases (GHG), transportation is the largest contributor. Figure 1.1 depicts that 29% of total GHG released in the United States in 2019 was due to transportation.²

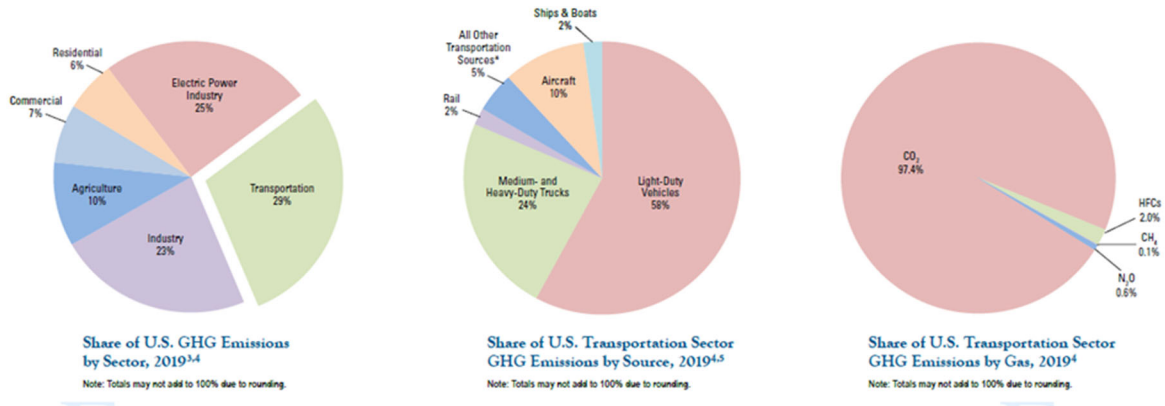


Figure 1.1 Transportation emissions of the United State.² (From U.S transportation sector greenhouse gas emissions 1990-2019. EPA, Ed. 2021).

Various research efforts have been carried out to mitigate the effects of GHG and the subsequent environmental impact. The current rate of non-renewable energy source depletion endangers economic and environmental sustainability. To address the global energy crisis and climate change, there is a strong demand for environmentally sustainable renewable energy systems such as fuel cells and electrolyzers. Figure 1.2

illustrates the trend in energy consumption towards renewable energy sources in the future.³ Special efforts have been devoted to increase renewable energy contributions.

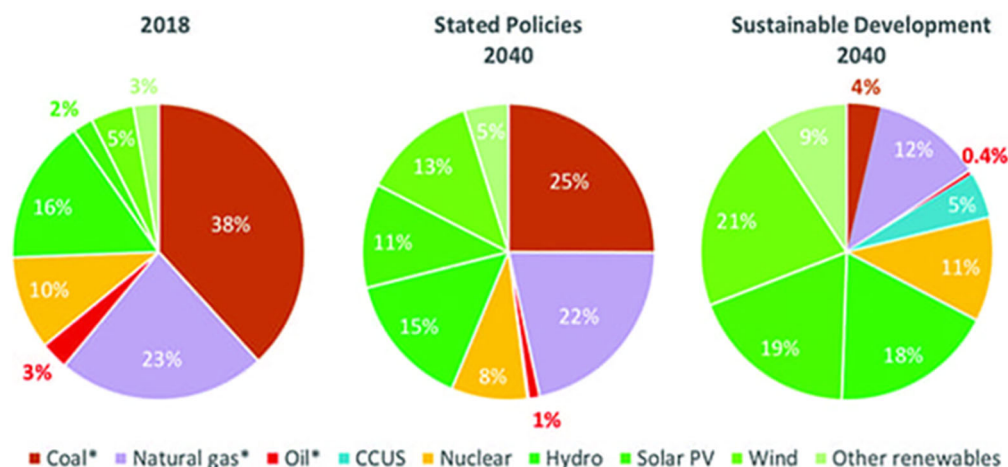


Figure 1.2 Global energy consumption by energy source (2010-2050).³ (From Javaid, U.; Iqbal, J.; Mehmood, A.; Uppal, A. A., Performance improvement in polymer electrolytic membrane fuel cell based on nonlinear control strategies—A comprehensive study. *PLOS ONE* **2022**, *17* (2))

Electrochemical oxygen reduction and carbon dioxide reduction (CO₂RR) are becoming significantly important in achieving future energy goals. These reactions occur at the gas diffusion electrodes of fuel cells and CO₂ electrolyzer, respectively. However, their catalytic activity, long-term stability, and product selectivity have remained challenging. Responding to those challenges requires appropriate catalysts. Electrocatalysis is thus an important aspect in determining the future directions of oxygen reduction reaction (ORR) and CO₂RR research.

1.2 Electrocatalysis

A catalyst is a chemical substance that can boost the rate of a chemical reaction without being consumed. This concept was introduced by the Swedish chemist Jöns Jacob Berzelius in 1835.⁴ Figure 1.3 depicts the effect of a catalyst in a hypothetical exothermic reaction.⁵ Electrocatalysis which is a special case of heterogeneous catalysis, involves redox reactions by transforming electrons across the interface between electrode and electrolyte.⁶

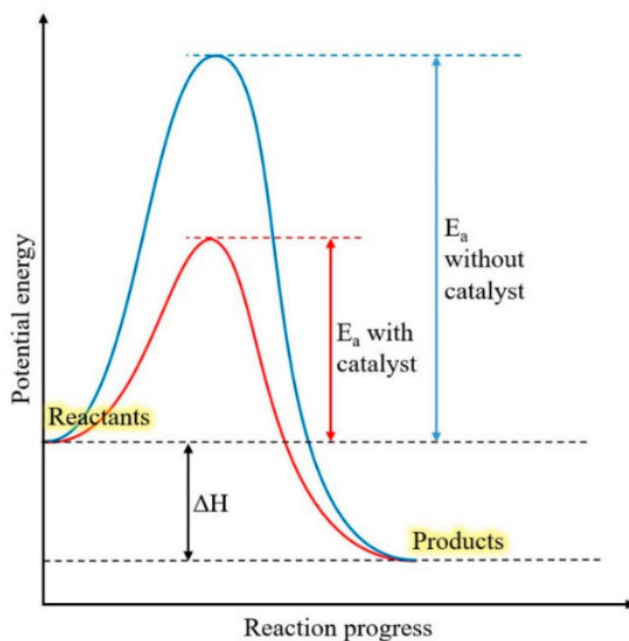


Figure 1.3 Effect of catalyst on potential energy profile.⁵ (From Sinar Mashuri, S. I.; Ibrahim, M. L.; Kasim, M. F.; Mastuli, M. S.; Rashid, U.; Abdullah, A. H.; Islam, A.; Asikin Mijan, N.; Tan, Y. H.; Mansir, N.; Mohd Kaus, N. H.; Yun Hin, T.-Y., Photocatalysis for Organic Wastewater Treatment: From the Basis to Current Challenges for Society. *Catalysts* **2020**, *10* (11), 1260).

1.2.1 Sabatier principle for electrocatalysis

In the early 1900s, French chemist Paul Sabatier introduced the concept of volcano-shaped dependence to identify the optimum catalyst.⁷ Based on this principle, the best catalyst should bind atoms or molecules with an intermediate strength: neither too weak nor too strong.⁸ Figure 1.4 is the representation of the Sabatier principal volcano plot for the reaction of two molecules that occurs on the catalyst surface.⁹ As shown in this representation, the reaction rate is either limited by weakly bound intermediates or strongly bound intermediates.

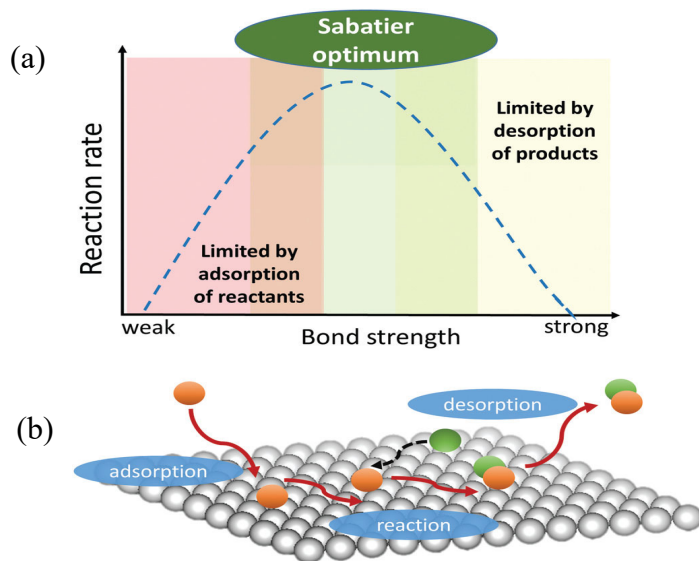


Figure 1.4 (a) Schematic representation of the qualitative Sabatier principle (b) Illustration of the reaction of two molecules (green and orange balls) and its steps.⁹ (From Sebastián-Pascual, P.; Jordão Pereira, I.; Escudero-Escribano, M., Tailored electrocatalysts by controlled electrochemical deposition and surface nanostructuring. *Chemical Communications* **2020**, 56 (87), 13261-13272).

1.3 Electrochemical reactions

Typically, electrochemical reactions comprise two half-reactions, i.e., cathodic and anodic reactions. These reactions occur in an electrochemical cell, which includes cathode, anode, electrolyte, semi-permeable membrane, and an external circuit that allows the transfer of electrons through it. The electrochemical cell is also a redox system. The rate of electron transfer between electrode and redox species is determined by the potential energy gradient across the interface between electrode and electrolyte.¹⁰ A general electrochemical reaction involving mass transport and electron transfer is shown in Figure 1.5.¹¹

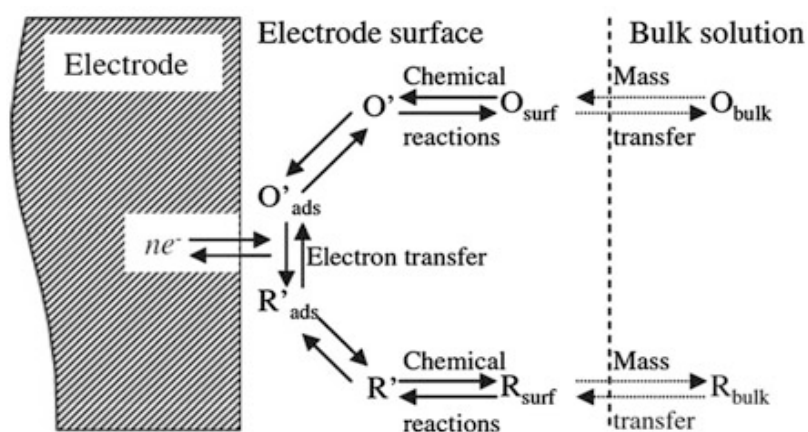


Figure 1.5 A pathway of the general electrode reactions.¹¹ (Brownson, D. A. C.; Banks, C. E., Introduction to Graphene. In *The Handbook of Graphene Electrochemistry*, 2014; pp 1-22).

The cell operates either spontaneously (batteries, fuel cells) or to induce non-spontaneous transformations (electrolysis).¹² As the electrochemical reaction continues,

there is an inherent connection between the thermodynamics and the kinetics of the electrochemical system. Thermodynamics and kinetics determine the feasibility of the reaction and its mechanism.

1.3.1 Thermodynamics and potentials of the cells

In thermodynamic aspect, the reaction Gibbs free energy difference (ΔG) is considered. This is associated with the direction of the net reaction. If $\Delta G < 0$, the forward reaction is thermodynamically favored and the reaction occurs spontaneously. $\Delta G > 0$ indicates that the forward reaction is non-spontaneous which requires the supply of energy to enforce the reaction. The equation of half-reaction for an Ox/Red couple is given below.¹³



where *Ox* is the oxidant, i.e., the form that can gain electrons, ***Red*** is the reductant, i.e., the form that can donate electrons. The Gibbs free energy change (ΔG°) is related to the standard cell potential of the reaction (E°) as shown below.¹³

$$\Delta G^\circ = -nFE^\circ \quad \text{Equation 1.2}$$

where ***n*** is the number of electrons that passed through the electrochemical cell, and ***F*** is the charge on a mole of electrons, which is about 96,500 C.

Table 1.1 shows the ΔG° for some electrochemical reductions in an aqueous electrolyte. The conversion of oxygen gas into water is a spontaneous reaction because ΔG° is negative. On the other hand, CO₂ reduction is thermodynamically not favorable.

Moreover, in a Galvanic cell, reactions occur spontaneously at the electrode when they are externally connected by a conductor.¹² On the other hand, electrolytic cell is in which reactions occur non-spontaneously therefore, it is required to supply external voltage. Therefore, fuel cells are regarded as the Galvanic cell while the CO₂ reduction is the electrolytic cell.

Table 1.1 Electrochemical Reactions and Corresponding ΔG° in an aqueous solution.^{14, 15}

| Reduction reaction | E° (V) vs SHE | ΔG° (kJ mol ⁻¹) ^a |
|--|----------------------|---|
| $\text{H}^+ + 2\text{e} \rightarrow \text{H}_2$ | 0 | 0 |
| $\text{O}_2 + 4\text{H}^+ + 4\text{e} \rightarrow 2\text{H}_2\text{O}$ | 1.23 | -474.8 |
| $\text{O}_2 + 2\text{H}^+ + 4\text{e} \rightarrow 2\text{H}_2\text{O}_2$ | 0.34 | -129.3 |
| $\text{CO}_2 + 2\text{H}^+ + 2\text{e} \rightarrow \text{CO} + \text{H}_2\text{O}$ | -0.10 | 19.3 |
| $\text{CO}_2 + 2\text{H}^+ + 2\text{e} \rightarrow \text{HCOOH}$ | -0.19 | 36.6 |

Note: ^a Gibbs free energy of the reaction for a mole of O₂ and CO₂ at 298 K, 1 atm, in 1M solution.

1.3.2 Kinetics of the reactions

Reaction kinetics are important for determining the reaction rate. Kinetics related to the faradaic current and the overpotential (η). Oxidation or reduction reaction generates the Faraday current, and the magnitude of the Faraday current is governed by the Faraday's law.¹³ In a given electrochemical reaction, the overpotential (η) means the electrode potential difference between the applied potential (E) and equilibrium potential (thermodynamic potential) (E_e) to drive a certain current in the electrochemical cell.¹⁶

$$\eta = E - E_e$$

Equation 1.3

The overpotential is determined by three factors.¹⁷

(1) Activation overpotential (η_a) – this originates from the activation energy of the electrochemical redox reactions.

(2) Concentration overpotential (η_c) – this arises due to the mass transport (charge carriers) limitations from the bulk to the electrode surface.

(3) Ohmic loss (η_o) – this is also known as IR drop which originates due to electrolyte and external electrical contacts. (*Note: I – current, R-resistance, IR – voltage*)

In an electrochemical cell, minimization of η_c and η_o is a technical problem. When η_c and η_o are negligible, therefore, the main purpose of electrocatalysis is to find a better electrode material to ensure that η_a is minimum. In this situation, the following relationship between current (i) and activation overpotential can be derived. This equation is often referred to as the Butler-Volmer (B-V) equation in electrochemistry.¹⁸

$$i = i_o \left\{ e^{|-(\alpha)F\eta_a/RT|} - e^{|(1-\alpha)F\eta_a/RT|} \right\} \quad \text{Equation 1.4}$$

where α is transfer coefficient, i_o is exchange current density which is an indication of electron transfer rate at equilibrium potential. “Clearly, the larger the i_o for a given α , the lower is the overpotential required to maintain a certain current density, therefore the better the catalyst.”¹⁶ The first and second exponential terms correspond to reduction and oxidation, respectively. i is a net current when both reduction and oxidation occur.

When the reduction dominates in the electrochemical process, the following linear relationship is taken.

$$i = i_o e^{-(\alpha)F\eta_a/RT} \quad \text{Equation 1.5}$$

$$\log|i_c| = -\left(\frac{(\alpha)F}{RT}\right)\eta_a + \log(i_o) \quad \text{Equation 1.6}$$

The B-V equation agrees with the Tafel equation when either the cathodic or anodic term dominates.¹⁹ When the electrochemical system moves further from its equilibrium, typically for highly irreversible reactions (very low exchange current density) and for large η (i.e., $|\eta| \geq 50 \text{ mV}$), the B-V equation is re-arranged to obtain the Tafel equation below.

$$\eta = a + b \log i \quad \text{Equation 1.7}$$

$$\text{where } a = \frac{2.3RT}{\alpha F} \log i_o \quad b = \frac{-2.3RT}{\alpha F}$$

In the Tafel equation, b is the slope which allows determines α , and the interpolation of the linear segment to $\eta = 0$, which is the equilibrium potential, gives i_o . Consequently, The Tafel equation is useful to assess the kinetic parameters of the catalyst.

1.3.3 Effects of mass transfer

In an electrochemical reaction, it is necessary to have sufficient reagents in close proximity to electrode interface to facilitate continuous charge transfer. Therefore, mass

transport of redox species in and out of the interface is an important factor to proceed an electrochemical reaction. Figure 1.6 illustrates three modes of mass transport including diffusion, convection, and migration.^{13, 20} However, in an electrochemical cell, diffusion is the most dominant mass transport mode.²¹ Diffusion occurs due to the concentration gradient, which is the driving force to transport materials from the electrode surface to the bulk solution and vice versa.

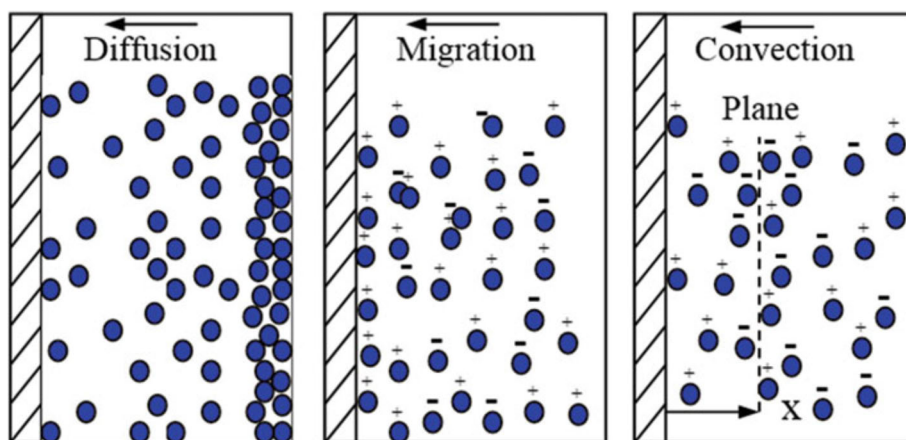


Figure 1.6 Modes of mass transfer.²⁰ (From Perez, N., Mass Transport by Diffusion and Migration. Springer International Publishing: 2016; pp 151-197).

The above-mentioned B-V equation was derived assuming that the effect of mass transport was negligible. When a reaction is “forced” to progress at high rates by applying a high overpotential, the B-V equation predicts that the current will increase exponentially as a function of η .⁶ However, there is always a limit to the achievable reaction rate where the “limiting current” originates due to the mass transport limitation.

$$j_{lim} = \frac{FD_A[A]}{\delta}$$

Equation 1.8

where j_{lim} is the limiting current density, D_A the diffusion coefficient of the reactants, $[A]$ its concentration, and δ the diffusion layer thickness. The diffusion layer is the layer of electrolyte where the concentration of reactant differs from the bulk solution. The δ depends on the hydrodynamics of the solution and the electrode shape. Mostly, kinetics and diffusion together contribute to the reaction rate. Mostly, kinetics and diffusion together contribute to the reaction rate. Experimentally, the mass transport to electrode surface can be enhanced by enforcing convectional flow of electrolyte. One common way is to employ a rotating-ring-disk-electrode (RRDE).

1.4 Importance of ORR in fuel cells

Proton exchange membrane fuel cells (PEMFCs) and metal-air batteries (MAB) are considered as next generation energy devices for clean power generation. ORR is a critical process in both devices. These devices are regarded as pollution-free devices with high energy densities. PEMFCs is a two-electrode system (cathode and anode) which converts chemical energy of hydrogen directly and efficiently into electrical energy, heat, and water as a byproduct.²² FC require the continuous feeding of H₂ and O₂ to support their chemical reactions, while in MAB, chemical energy usually comes from ORR with metal ions or oxides.²³ In these electrochemical processes, ORR occurs at the cathode, where O₂ molecules are reduced by electrons. To undergo this reaction, the O=O bond must break electrochemically, which is difficult because the O₂ molecule has a strong binding energy (486 kJ/mol).²⁴ Therefore, it is necessary to use an appropriate electrocatalyst to reduce the barriers of bond activation and cleavage.

1.4.1 Platinum-based ORR electrocatalysts

Various electrocatalysts have been reported for ORR in literature. Among those, platinum supported on carbon support (Pt/C) is the state-of-the-art catalyst for ORR because of its high current density and low overpotential.²⁵ Pt/C drives ORR through a direct four electron pathway (Equation 1.10), while an indirect process (Equation 1.11 and 1.12) occurs on glassy carbon electrode.^{15, 26, 27} Both pathways undergo in acidic and alkaline media. In the alkaline medium, the proton (H^+) source is water (H_2O) as shown below.



Direct pathway



In direct pathway



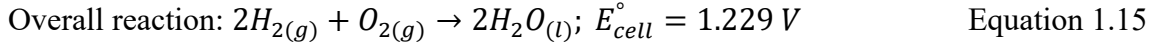
In PEMFCs that run in acidic condition, ORR occurs at the cathode (Equation 1.13), while hydrogen oxidation reaction (HOR) takes place at the anode (Equation 1.14).

Cathode (reduction)



Anode (oxidation)





The 4-electron and 2-electron ORR selectivity are governed by the competitive reactions given in Equation 1.16 and 1.17.



For the 4-electron pathway (Equation 1.16), the O-O bond in the intermediate *OOH should be broken, and a catalyst with the capability to adsorb *O rather than OOH is required. For the 2-electron pathway (Equation 1.17), the *OOH intermediate O-O bond needs to be preserved, and a catalyst that promotes *OOH adsorption is necessary. This is an important aspect to design to understand the fundamentals of ORR catalysis in terms of reaction mechanism and intermediates.

Apart from catalyst materials, the overall energy efficiency of PEMFCs is governed by the favorable kinetics of ORR and HOR at the cathode and anode, respectively. In general, ORR is considered as the limiting factor in overall performance of PEMFC due to the unfavorable kinetics of the four-electron pathway.²⁸ However, due to the sluggish kinetics of ORR, it requires a higher Pt/C catalyst loading to achieve excellent performance. Moreover, Pt/C suffers from several drawbacks including fuel crossover, carbon monoxide (CO) poisoning, Pt Ostwald ripening,²⁹ Pt dissolution/detachment, high cost, and durability.³⁰ Thus, the improvement of Pt based catalysts and the development of their alternatives have become the central issue in PEMFCs.

1.4.2 Heteroatom doped carbon materials

Recently, there has been considerable interests in the approaches that incorporate single dopants such as nitrogen (N), sulfur (S), phosphorus (P), boron (B) and dual heteroatoms into carbon nanostructure, to create defects and abundant active sites for ORR.^{31, 32} Dai's et al. reported nitrogen doped carbon-based materials for the first time as a promising candidate for ORR because these materials possess high surface area, good conductivity, tunable morphology, and economic viability.³³ Incorporating electronegative nitrogen (N) atoms into carbon nanotubes creates a relatively high positive charge density on the carbon atom next to N, which change the adsorption mode of O₂ to facilitate ORR.³⁴ Figure 1.7 shows typical N configurations in N-doped carbon and their X-ray photoelectron spectroscopy (XPS) binding energies.³⁵ Thereafter, graphene-based N-doped materials were reported to be effective electrocatalysts for ORR in alkaline fuel cells. These catalysts had a promising catalytic activity, stability, tolerance to methanol, after much effort was devoted to synthesizing carbon materials from heteroatoms.

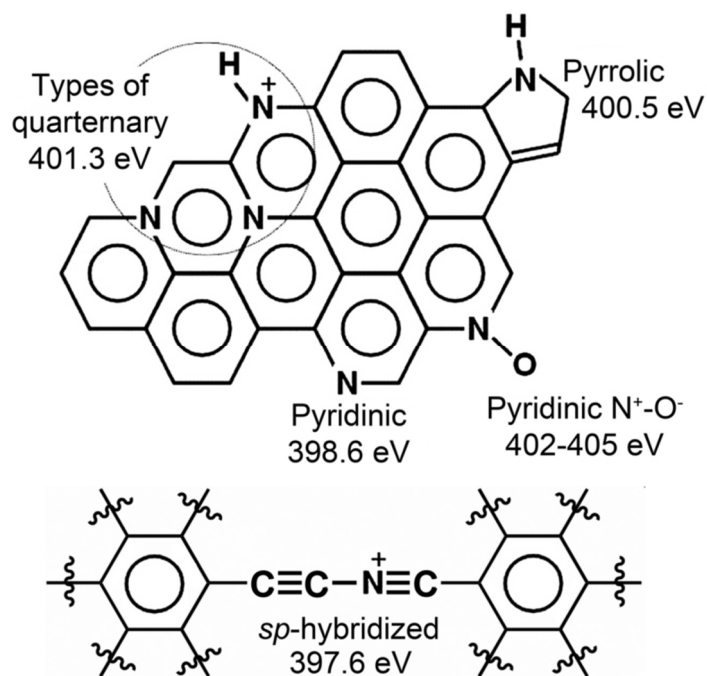


Figure 1.7 Representation of N species in N-doped carbon materials and their XPS binding energies.³⁵ (From Hu, C.; Dai, L., Carbon-Based Metal-Free Catalysts for Electrocatalysis beyond the ORR. *Angewandte Chemie International Edition* **2016**, 55 (39), pp 11736-11758).

Over the past few years, a lot of efforts have been made to further improve catalytic performance of N-doped carbon materials by co-doping. Among those, N and B co-doping has been given considerable attention due to their synergistic effect on the ORR activity. Qiao *et al.* studied a higher activity for graphene doped with B- and N because the B and C atoms bound to N dopants act as the active sites, respectively.³⁶ However, there are limited studies for doping conditions such as temperature, pressure, and composition of each precursor. Jin *et al.* reported that the B and N configurations can be easily adjusted to obtain dominant active sites with a proper mass ratio range by

changing the synthesis temperature.³⁷ Therefore, it is imperative to bridge the gap in the knowledge of how synthesis temperature influences the doping and electrochemical performance of electrocatalysts for ORR.

1.4.3 Relevance of CO₂ capturing and energy conversion

Climate models call for a huge demand for zero GHG emissions by the year 2050 to slow down the rate of rapidly increasing global temperature.³⁸ However, the processes of CO₂ capture and utilization (CO₂ conversion and product separation) require a substantial energy input. Thus, it is difficult to minimize the energy needed at all of the above stages. There are many designs that have been constructed and suited to perform both CO₂ capture and transformation.³⁹⁻⁴²

Most research employs experimental set-ups that utilize pressurized, gaseous CO₂ as a chemical feedstock that is fed into CO₂ electrolyzer for the conversion into products. Very few studies were reported on the integration of CO₂ capture with the conversion process. In these studies, (1) gaseous CO₂ is dissolved into an adsorber that is a basic solution to obtain bicarbonate or carbonate, and (2) bicarbonate/carbonate is electrochemically converted to syngas, formate, or other valuable fuels and chemicals.⁴³ Figure 1.8 showed the various prototype systems to illustrate CO₂ capture, concentrated into either pressurized gas or valuable products.

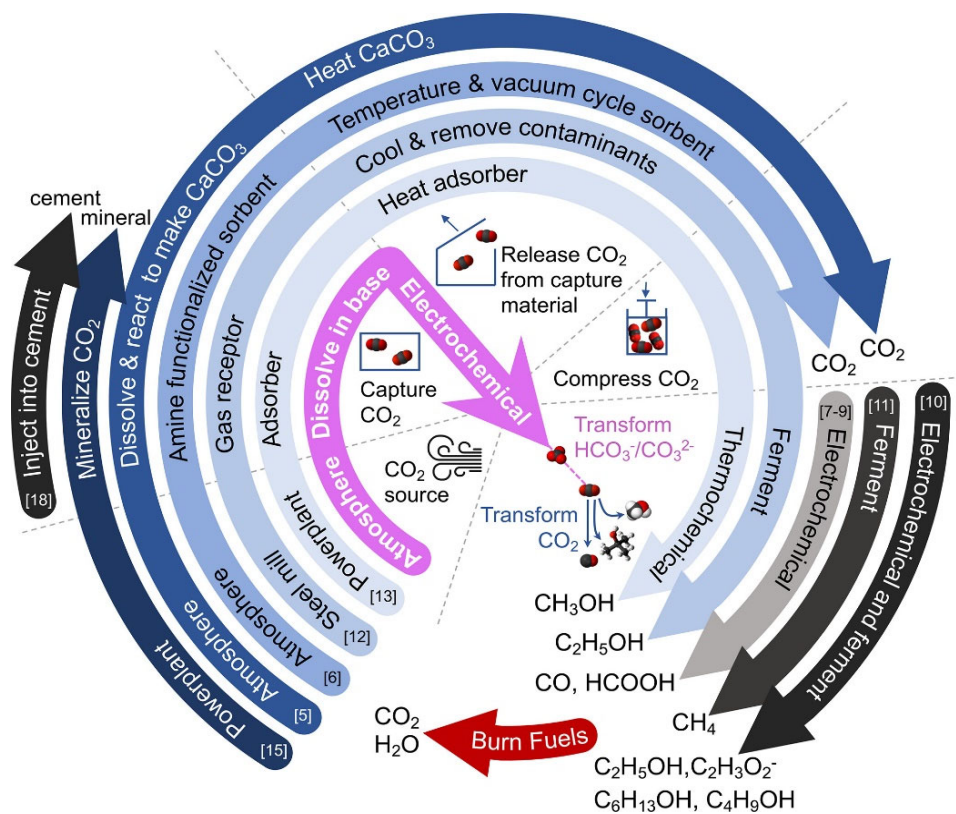
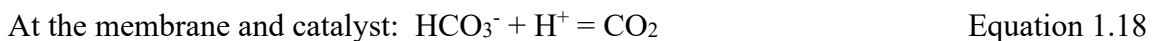
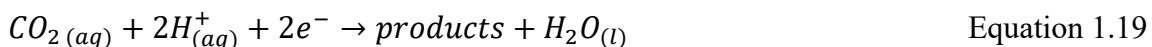


Figure 1.8 Various prototype systems for CO₂ capturing and converting into valuable products. (The pink arrow represents the bicarbonate conversion process).⁴³ (From Welch, A. J.; Dunn, E.; DuChene, J. S.; Atwater, H. A., Bicarbonate or Carbonate Processes for Coupling Carbon Dioxide Capture and Electrochemical Conversion. *ACS Energy Letters* **2020**, 5 (3), pp 940-945).

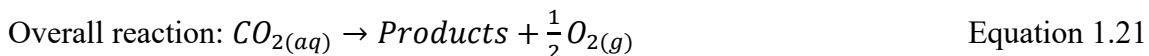
In the bicarbonate conversion process the following reactions are predicted at the membrane, anode, and cathode.



At cathode reaction (reduction)



At anode reaction (oxidation)



This approach is still new and there is ample room for development in terms of catalyst, membrane and electrolyzers. So, it is better to study this new approach to understand challenges and outcomes.

1.5 Organization of this dissertation

In electrocatalysis, activity, selectivity, and durability are recognized as important metrics to determine the performance of an optimum catalyst. In comparison with precious metal-based catalysts, heteroatom doped, or heteroatom supported non-noble metal catalysts offer unique advantages for ORR and CO₂RR. However, there is still room for the improvement of these catalysts. Therefore, electrochemical reactors and electrodes should be continuously developed for achieving high current densities and activities relevant for industrial applications. Among various electrode materials, carbon-based materials have shown extensive potential for electrocatalytic ORR and CO₂RR. To promote electrocatalytic activity of carbon-based catalysts, modulating electroneutrality of carbon atoms with promoted spin and charge densities is required.

This dissertation focuses on developing facile and versatile methods to synthesize heteroatom doped carbon-based catalysts with promising performance for ORR. Furthermore, the dissertation aims to study electrolysis reactors and electrodes for bicarbonate conversion into valuable products. Heteroatom doped metal-free catalysts

are suitable because of their superior electrochemical performance, cost effectiveness, and stability in working in electrochemical conditions. The aim of introducing heteroatoms to carbon-based materials is to break the electroneutrality of the carbon support and boost the extent of defects and active sites. Also, different heteroatom combinations acquire different amounts of spin and charge densities to enhance the catalytic performance.

Chapter 2 of this dissertation investigates the impact on doping temperature to synthesize nitrogen (N) and boron (B) doped carbon nano-onions (NB-CNOs) catalysts and their performance for ORR. Furthermore, the catalyst microstructure was examined using X-ray photoelectron spectroscopy (XPS), and Raman spectroscopy. To visualize the chemical structure of the active sites, the catalysts were analyzed using scanning transmission electron microscopy (STEM). The ORR performance was evaluated using rotating ring disk electrode (RRDE).

In Chapter 3, N-doped CNO (N-CNOs) was used as a support for copper (Cu) nanoparticles. N is the most popular dopant element for carbon-based materials due to its size similar to that of carbon atoms and larger electronegativity than carbon. N-doped carbon materials are typically more electrically conductive and have more active sites. The size and crystallinity of Cu catalysts were analyzed by X-ray diffraction patterns (XRD). Transmission electron microscopy (TEM) was used to detect small Cu nanoparticles (< 3 nm). Contact potential difference (CPD) of the doped and undoped catalysts was probed by Kelvin Probe Force Microscopy (KPFM). The ORR performance of catalyst was investigated.

Chapter 4 investigates bicarbonate conversion into valuable products and identifies challenges and motivations. Bicarbonate is a product of the alkaline CO₂ capturing process. In this fundamental study, customized gas diffusion electrode (GDE) was used to perform electrolysis. Cu coated carbon paper was used as the cathode while platinum supported on carbon was employed as the anode. Both catalyst microstructures were investigated using scanning electron microscopy (SEM) and other characterizations. Finally, chapter 5 will be devoted to the future aspects of these studies.

CHAPTER 2. SYNERGISTIC INTERACTION OF EDGE NITROGEN AND BORON DOPANTS IN CARBON NANO ONIONS FOR EFFICIENT OXYGEN REDUCTION REACTION

The author would like to thank Dr. Beth Guiton and Dr. Melonie Thomas for their help with scanning transmission electron microscopy (STEM) analysis.

2.1 Introduction

Oxygen reduction reaction is a key process in energy conversion and storages, corrosion, and electrochemical biosensing.^{22, 44, 45} For example, fuel cells require fast electron-transfer and 4-electron route of ORR occurring at cathode.^{25, 46} Although platinum (Pt) is still state-of-the-art metal for ORR, Pt-based electrocatalysts pose serious drawbacks including high cost, low availability, and poor long-term stability due to surface deactivation.⁴⁷ In addition to these issues, the recent disruption in global supply chains for critical minerals is increasingly demanding the development of metal-free catalysts.

The incorporation of heteroatom dopants such as N, B, S, or P was recognized as an attractive strategy to boost up catalytic activity of metal-free carbon-based catalysts. This approach generally involves the creation of active sites by placing atoms with dissimilar electronegativity next to carbon atoms.³³ Recently, this doping approach was extended to incorporate multiple elements for synergistic effects.²⁴ For example, co-doped N and S further enhanced ORR activity due to the distribution of spin density and charge density from two dopants.^{48, 49} N and B are another popular pair of co-dopants in generating active sites in carbon by taking advantage of dissimilar electronegativities of N, B, and C.^{45, 50} Compared to C (electronegativity(χ) = 2.55), N is more electron-rich (χ

= 3.04) and B is more electron-deficient ($\chi = 2.04$). Boric acid and ammonia are common precursors of N and B, respectively. The incorporation of N and B can be done simultaneously or sequentially.^{37, 46}

Carbon nano onions are highly defective and disordered, consisting of a hollow core surrounded by concentric graphitic shells.⁵¹ Due to surface curvature, strain energy, and large surface area, CNOs demonstrated high chemical reactivity and electrochemical activity.⁵² Curvature is the consequence of arrangement of six membered and five membered rings, which shifts π electron density towards the outer surface and enhances reactivity.⁵³ Incorporation of N and B into curved, high-strain CNOs through a single-step annealing has potential for an excellent electrochemical performance and long-term stability.⁵⁴ Yu *et al.* claimed that catalytic performance of N, B co-doped carbon nanotube was controlled by the locations of heteroatoms, i.e., whether two dopants were directly bonded (N-B) or separated (N-C-B).⁵⁵

Despite previous studies, the role of N and B dopants and their structure-function relation are not clearly understood. To shed light on the role of N and B dopants in catalytic activity, the locations and chemical configurations of the two dopants should be precisely controlled.³⁷ Also, essential information may be obtained by visualizing heteroatoms using an advanced technique such as high-resolution scanning transmission electron microscopy (HR-STEM). We recently illustrated the presence of scattered or clustered N and S atoms in N and S- co-doped CNOs using an aberration-corrected STEM.⁴⁹ In the current study, we employed STEM to identify edge and bulk dopants and to illustrate their impacts on active site formation towards ORR.

Herein, we report the first systemic study on the effects of annealing temperature on the doping level, type, and the location of active site in N, B co-doped CNOs (NB-CNO). The synthesis of NB-CNOs was done by sequential doping. These results provide an insight on the interaction between B and N and how they alter the catalytic activity. Based on XPS, edge N-B clusters are the most active for ORR and these sites have transformed to bulk N-B clusters as temperature increases. Raman analysis confirms the availability of relatively high carrier density in NB-CNO supporting catalytic performance for ORR in alkaline media via 4-electron transfer pathway.

2.2 Experimental

2.2.1 Chemical oxidation of CNOs

Pristine CNOs (p-CNO) were prepared from nanodiamond powders (dynalene NB50, nanostructured and amorphous materials, Inc). Oxidized CNOs (Ox-CNO) were prepared by refluxing CNOs with saturated HNO₃. Typically, 100 mg CNOs were dispersed in the mixture of 50 mL saturated HNO₃ (ACS grade) and 50 mL de-ionized (DI) water in a three-neck flask and sonicated for 15 minutes to prepare a homogenous solution. After that, the mixture was refluxed at 105°C for 4 hours and 30 minutes. Ox-CNOs were washed with DI water until the mixture became neutral. Then, Ox-CNO were dried in an oven at 60 °C overnight

2.2.2 Synthesis of nitrogen doped CNOs (N-CNO)

N-CNO were prepared by thermally annealing Ox-CNO after mixing with urea (Sigma Aldrich, ACS reagent, 99.0-100.5%). Typically, 100 mg of Ox-CNO were

completely grinded with 500 mg of urea and mounted on a quartz boat. Then, the quartz boat with the mixture was loaded in a tube furnace (Thermo Scientific Lindberg/Blue M™ Mini-Mite™). After evacuating the furnace for 30 minutes, argon gas flew for 30 minutes to remove water and oxygen. Then, the mixture was thermally annealed at 700 °C for 3 hours under argon atmosphere in the furnace. The annealing rate was 3 °C/min. During this treatment, urea was decomposed to provide nitrogen containing gaseous products as a source of nitrogen dopant. After the annealing process, the tube furnace was cooled to room temperature under the same condition. Powder taken from the tube furnace after annealing were centrifuged with DI water 2 times to remove any soluble impurities. The purified powder was dried in the oven at 60 °C overnight. This sample is denoted as N-CNO(700) where the number in the parenthesis indicates the annealing temperature used for nitrogen incorporation.

2.2.3 Synthesis of nitrogen (N) and boron (B) co-doped CNOs (NB-CNO)

NB-CNO were prepared by annealing N-CNO(700) in the presence of boric acid, H_3BO_3 (Sigma Aldrich, 99.999% trace metals basis) at different temperatures (600°C, 700°C, 800°C, 900°C, and 1000°C). These products were denoted by NB-CNO(X), where X in the parenthesis is the annealing temperature. Prior to the treatment, 100 mg of N-CNO(700) were ground with 500 mg of H_3BO_3 to prepare a fine powder. Then, this powder was transferred to a quartz boat and loaded in the furnace. The temperature was increased to X with a ramp rate of 3 °C/min. Then, the powder mixture was annealed for 3 hours. During the annealing process, H_3BO_3 decomposes to diboron trioxide, $\text{B}_2\text{O}_3(\text{g})$, to generate boron atoms to replace carbon atoms by interacting with nitrogen dopants in

N-CNO(700). After the treatment, the tube furnace was cooled to room temperature under the same condition. Any B₂O₃ byproduct was removed by washing with boiled DI water followed by ethanol. The purified product was dried in the oven for 24 to 48 hours.

2.3 Material characterization

Raman spectroscopy was performed with a micro-Raman spectrometer (Thermo Scientific DXR). A diode-pumped Nd:YVO₄ laser was used as excitation source at 532 nm excitation (laser power: 5 mW). The elemental composition and the chemical states of Ox-CNO, N-CNO(700), and NB-CNO were probed by X-ray photoelectron spectroscopy (XPS, a Thermo Scientific K-alpha X-ray photoelectron spectrometer) with a monochromatic Al K α radiation. The spot diameter analyzed by XPS was 400 μ m. The crystalline structure and phases of all samples were analyzed using BRUKER AXS x-ray spectrometer equipped with Cu tube (1.54 Å) and energy dispersive LYNXEYE (1D mode) detector. STEM sample preparation, characterization, and Fourier filtering process is mentioned elsewhere.⁴⁹

2.4 Electrochemical measurements

2.4.1 Preparation of a rotating ring disk electrode (RRDE)

RRDE was prepared for electrochemical measurements as follows. A glassy carbon disk electrode (geometric area: 0.126 cm²) and a Pt ring electrode were polished with 0.05-micron alumina powder. Then, catalyst (5 mg) and nafion (50 μ L, fuel cell store, 5 wt% in ethanol) were mixed in 2.5 ml of DI water and sonicated for 1 hour to prepare homogenous catalyst ink (2 mg/ml). Subsequently, 40 μ L of the ink was mounted

on the glassy carbon by drop-casting. Then, the electrode was dried in the oven at 60°C overnight.

2.4.2 Electrochemical performance test

Electrochemical characterization for ORR was performed in 0.1 M KOH (VWR chemicals BDH) under the purge of N₂ gas or O₂ gas with a CHI 760D potentiostat (CH Instruments, USA). KOH electrolyte was purged with either N₂ or O₂ gas for 45 min prior to electrochemical measurements. Ag/AgCl (CH instruments), Pt wire and RRDE served as the reference (RE), counter (CE), and working electrodes (WE), respectively. Linear sweep voltammograms (LSVs) were recorded with the rotation of the RRDE. LSVs were recorded at the potential sweep rate of 5 mV/s. The rotation rate of the electrode varied from 400 rpm to 3600 rpm. In RRDE measurement, LSV and chronoamperometry were simultaneously performed at the disk and the ring, respectively. RRDE was rotated at 1600 rpm for the convective flow of O₂ and the fixed potential (0.35 V) was applied to the ring. This ring current corresponds to the oxidation of HO₂⁻ formed from ORR at the disk. The percentage of HO₂⁻ was used to calculate the electron transfer number (*n*) (equations 3 and 4 in the supporting information).

2.5 Results and discussion

NB-CNO was converted from p-CNO through sequential doping of N and B. First, p-CNOs were derived from detonation nanodiamond (ND) by thermal annealing at 1700 °C (Figure 2.1). During this process, sp³-bonded ND particles transformed into sp²-hybridized CNOs.⁵⁵ NDs are converted to fully graphitized carbon onions when annealing temperature is above 1500 °C.⁵³ Typically, p-CNO are inert, so direct doping

of heteroatoms is difficult. Therefore, it is necessary to elevate surface energy of CNOs by forming surface oxygenated groups and defects to facilitate the incorporation of dopants.⁵⁶ In this work, Ox-CNO were synthesized by a modified Hummers method and used for the sequential N and B doping (Figure 2.1).⁵⁵

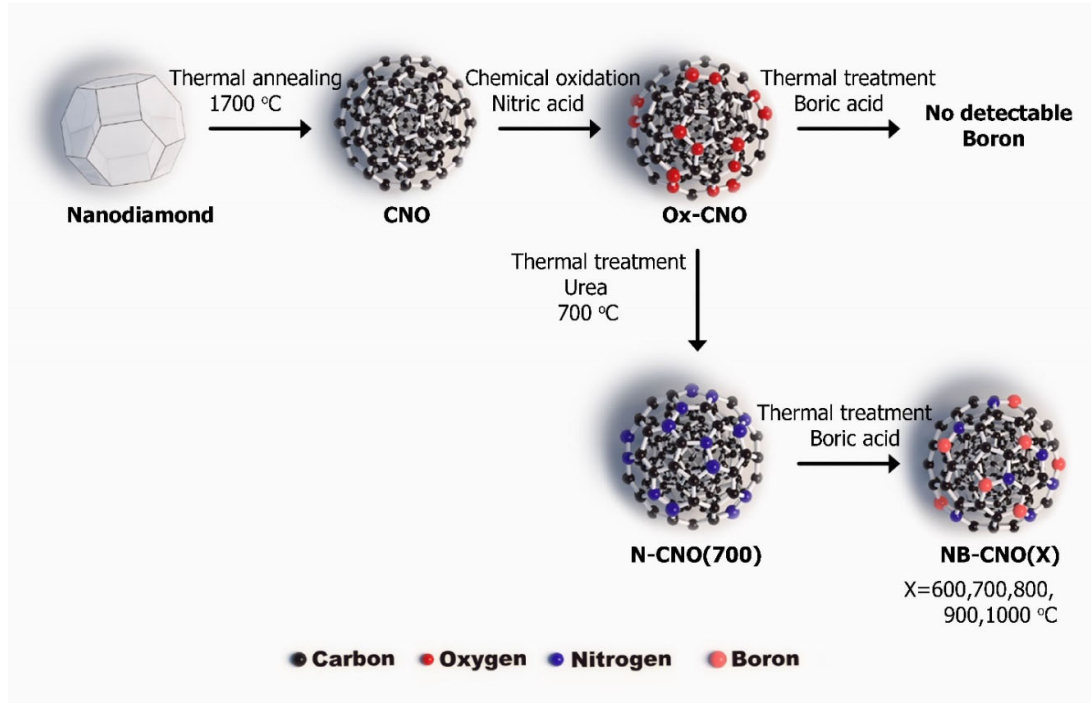


Figure 2.1 Synthetic procedure of CNOs, N-CNO(700) and NB-CNO(X).

We have tested the incorporation of B in two ways: (1) direct B doping into Ox-CNO and (2) sequential B doping following N doping. In the first approach, Ox-CNO were annealed in the presence of boric acid (temperature varying from 600 °C to 1000 °C). XPS analysis of this product didn't show any trace of B. The failure of incorporating B is attributed to the convex curvature of CNOs.⁵⁷ Also, a size mismatch between B and C may slow down the kinetics of B incorporation.³⁷ Due to these factors, the

incorporation of B involves high activation barrier and typically requires temperature above 1650 °C.⁵⁸⁻⁶⁰ In the second approach, B doping was sequentially conducted after N doping to take advantage of an interaction between N and B. As shown in Figure 2.1, B was incorporated as a function of annealing temperature (600 °C – 1000 °C) after the N doping was completed at 700 °C. The incorporation of B was only successful in the presence of N, implying a strong interaction between N and B. Boron doping temperature was identified as a crucial factor to influence chemical configurations of N and B.

Raman spectroscopy is a useful tool to characterize defects, microstructural disorder, charge carrier density, and electronic structure of graphene-based materials.⁶¹ In Figure S2.1, Raman spectra of p-CNO, Ox-CNO, N-CNO and all NB-CNO present three prominent peaks which are assigned to D, G, and 2D bands.⁶² D band at 1334-1340 cm^{-1} originates from the microstructural disorder and defects of materials. G band at 1565-1578 cm^{-1} is related to doubly degenerate E_{2g} at the center of the Brillouin zone, which originates from lattice vibration of sp^2 - carbon atoms in aromatic carbon rings.⁶³ The G band has a shoulder at the higher wavenumber ($\sim 1603 \text{ cm}^{-1}$), which is commonly observed in carbon materials under a strain.⁶⁴ In our materials, D* band arises due to strain together with the interaction between the localized vibration modes of dopants (N and B) or some impurities (defects or surface groups (O-H)) and the extended phonon modes G band for CNOs.^{65, 66} 2D band at 2670 – 2677 cm^{-1} is due to momentum conservation of the scattering of two phonons with opposite wave vectors. Unlike D band, the 2D band intensity is influenced by electron-electron interaction and it is not affected by defects in the carbon materials.⁶¹

The I_D/I_G ratio in Figure S2.1 is an indicator of defect density, degree of disorder, and the level of graphitization of graphitic carbon materials. The I_D/I_G ratio of N-CNO(700) is higher than that of the p-CNO, indicating that the density of defects increases as the result of nitrogen doping since substitutional nitrogen may disrupt sp^2 network and cause sp^3 defect regions.⁶⁷ Hence, the heteroatom doping raises the disorder of CNOs by generating defects due to different bond lengths of C-C/N-B/C-B/C-N.⁵⁴ In the case of B doping, the I_D/I_G ratio decreases after B incorporation into the lattice of N-CNO at 600 °C since substitutional B has shown enhanced graphitization of CNOs.^{55, 68} The I_D/I_G ratio of NB-CNO(700) is comparable to N-CNO(700). This is an indication of high substitutional doping in NB-CNO(700) sample. In contrast, the I_D/I_G ratio significantly decreases at 800 °C indicating that graphitization has enhanced which could be due to the high amount of B. At 800 °C, the degree of disorder increases again due to the formation of new defects since removing of heteroatoms from the surface. More detailed Raman analysis of (i) I_{2D}/I_G ratio, (ii) 2D band shift, and (iii) G band shift is summarized in Table S2.1 and Figure S2.2.

X-ray diffraction patterns (Figure S2.3(a)) provide information about phase and crystallinity of p-CNO and doped CNOs. All the samples show four different characteristic peaks at 2θ : 26.0°, 43.5°, 53.6°, and 78.2° attributable to (002), (100), (004), and (110) graphitic planes of CNOs, respectively.⁶⁹ XRD patterns display an intense peak at 26.0° for (002) and a broad asymmetric peak at 43.5° for the (100).⁷⁰ The incorporation of heteroatoms, N and B, into carbon nanostructure decreases an interlayer spacing between graphitic layers.^{54, 55, 71} It is noted that in all NB-CNO samples the peak position of the (002) plane slightly shifts toward higher 2θ angles compared to CNOs,

confirming that graphene stacking becomes more compacted in doped CNOs (Figure S2.3(b)). Based on Raman and XRD, NB-CNO(700) has active sites due to N and B dopants with high disorder which are consistent with XPS results shown in Figure 2.2. As a result, NB-CNO(700) has shown promising electrochemical performances for ORR.

Aberration-corrected STEM is a powerful technique that can resolve individual atoms owing to its spatial resolution up to the sub-atomic range. Z contrast or high-angle annular dark field (HAADF) imaging technique in STEM uses the detection of signals scattered at high angles, thus, the image intensity can be correlated to the atomic numbers (Z) of the elements present in the region of interest. HAADF imaging technique gives a perspective of the elemental composition of the sample. The intensity of the image signal (I) in a HAADF micrograph relates to the corresponding atomic number (Z) of the element as $I \propto Z^x$, where x is ~ 2 . Figure S2.4 (a-b) depicts the homogenous distribution of CNOs in the sample and Figure S2.4 (c-e) shows that even after the doping process the concentric shell structure is retained in samples NB-CNO (700, 800, and 900). The respective Fourier filtered images in Figure S2.4 (c-e) provide enhanced clarity by filtering out the noise, thus, some single atom dopants are visible in the doped CNOs. Figure 2.2 (a-c) shows a series of high-resolution HAADF micrographs of NB-CNO (700) collected in a manner that the subsequent image is a magnified image of the yellow square area in the previous image for better visualization. Figure 2.2 (d) is the Fourier filtered image of (c). It should be noted that the Fourier filtering has been performed to further increase the resolution of the row of atoms that is well in focus (the area inside the blue dashed rectangle) and the line scan showing the image contrast profile across the above-mentioned row of atoms is shown in Figure 2.2 (e). According to the intensity

ratios measured for each atom inside the blue-dashed square, the Z-contrast imaging suggests that the atom sequence is most likely to be N, C, N, C, C, B as marked in (e).

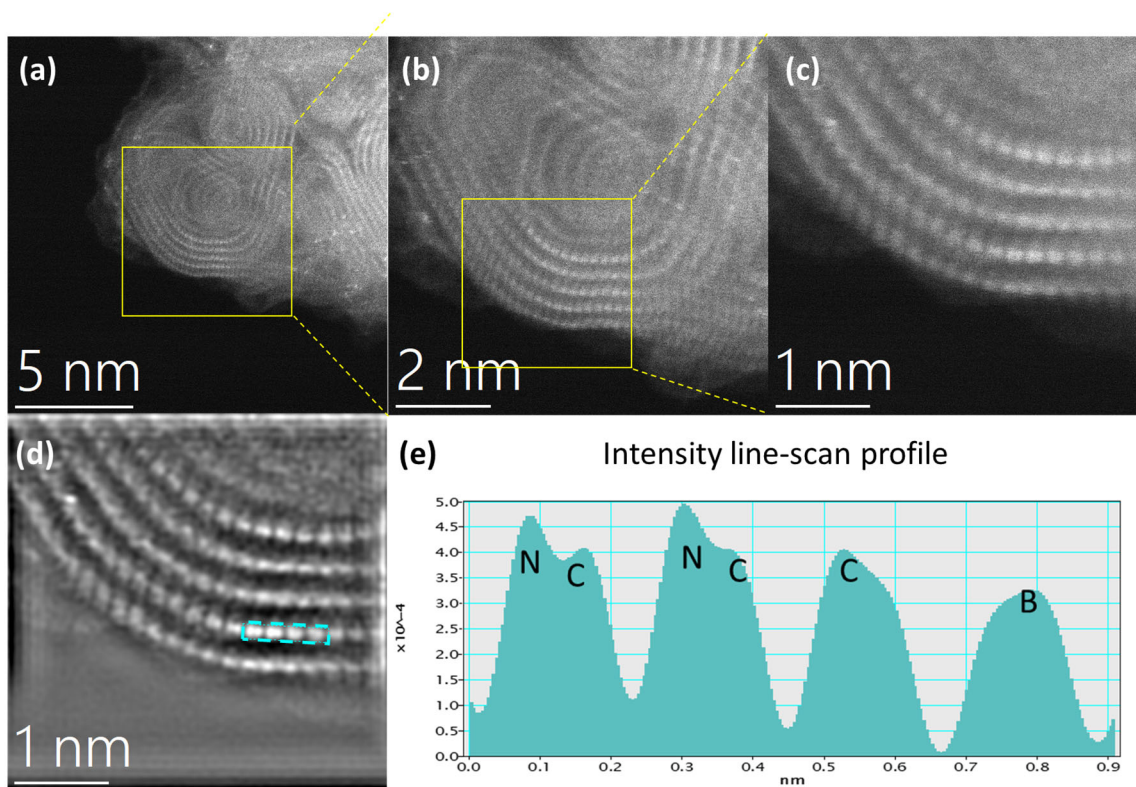


Figure 2.2 (a-c) STEM HAADF micrographs of NB-CNO (700) showing a series of magnified images of the area in yellow square regions in each image, and (d) is the Fourier filtered image of (c) with improved signal-to-noise ratio for enhanced clarity. (e) shows the intensity line-scan profile of the HAADF image across the atoms indicated by the blue dashed rectangle in (d) where the atoms are well in focus. The intensity profile suggests that given the intensity ratios of the highlighted atoms, they are most likely to be N, C, and B as marked in image (e).

XPS was performed for the analysis of elemental compositions and dopant chemical states. XPS results are summarized in supporting information (Table S2.2 and

S2.3). This confirms the successful doping of N and B. N atomic percentages of N-CNO(700), NB-CNO(600), NB-CNO(700), NB-CNO(800), NB-CNO(900) and NB-CNO(1000) are 2.9, 2.7, 2.7, 2.0, 1.1 and 0.7 at. %, respectively. B atomic percentages for the above samples are 0, 0.9, 1.1, 1.4, 0.9 and 0.9 at. %, respectively (Table S2.2 and S2.3). It is noteworthy that the N content gradually decreases and the B content increases as the annealing temperature is elevated from 600 °C to 800 °C. At 900 °C and 1000 °C, both N and B contents are reduced. The reduced B content at these temperatures is attributed to the decrease of N. This indicates that pre-existent N attracts B into CNOs.⁷²

Figure 2.3(a) and (b) present high-resolution XPS N 1s and B 1s spectra along with their deconvoluted peaks. All N 1s and B 1s spectra were deconvoluted by peaks with fixed FWHM of 1.2 -1.3 eV, respectively, to obtain the best fit. N-CNO(700) consists of four major peaks at around 398.7 (pyridinic-N), 399.7 (pyrrolic-N), 401.1 (graphitic-N), and 402.7 eV (N-O).^{54, 73, 74} Besides from aforementioned peaks, co-doped NB-CNO present the emergence of an additional peak at 397.7 eV corresponding to edge N-B configuration (Figure 2.3(a)).⁷⁵ The edge N-B clusters refer to B atoms next to pyridinic-N/pyrrolic-N and are formed at low B doping temperature.²⁵

As doping temperature increases, N and B dopants become internalized into the core of CNOs.⁷⁶ This bulk N-B configuration presents slightly higher N 1s binding energy than edge N-B configuration due to the donated electrons from the internalized N (graphitic-N).⁷⁷ Based on this, the position of N-B can be tracked as a function of B doping temperature. It is observed that the normalized edge N-B peak area increases up to 700 °C and then diminishes completely at 1000 °C (Figure 2.3c). The binding energy of bulk B-N clusters merges with that of pyridinic-N. Therefore, it is difficult to

accurately deconvolute bulk N-B from the pyridinic-N under this XPS resolution. The highest number of edge N-B clusters are found in NB-CNO(700) sample (Figure 2.3c).

This configuration change driven by annealing temperature can be also verified from the chemical shift in high-resolution B 1s spectra. The deconvoluted B1s XPS spectra (Figure 2.3b) shows three main peaks at around 189.8-190.5 (B-C-N), 191.1-191.5 (B-N) and 192.5 (B-O).^{25, 37, 78} Although the relative distribution of each chemical state does not change with the temperature (Figure 2.3d), peak shifts can be observed for B-C-N and B-N bonding configurations.

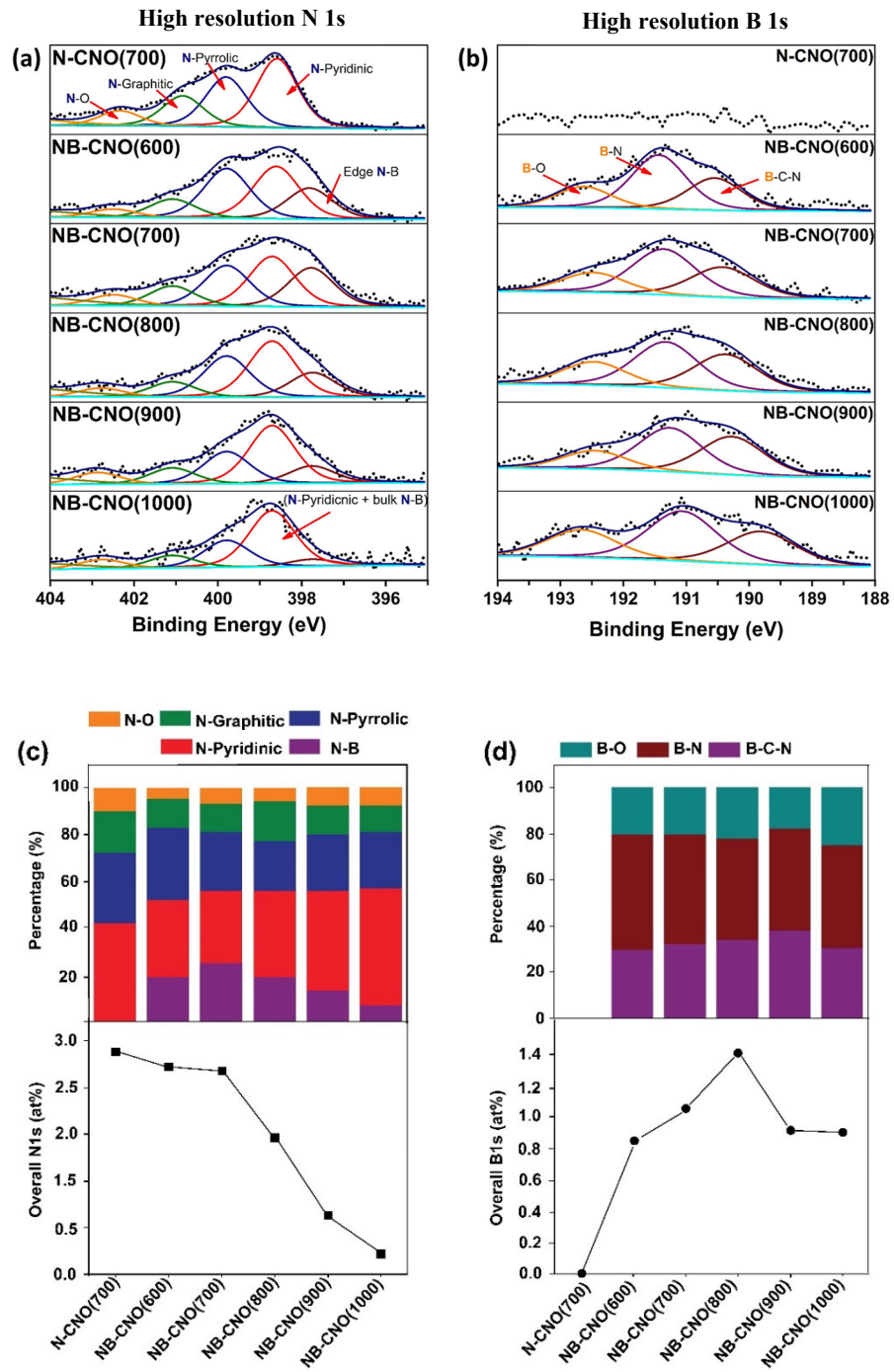


Figure 2.3 High resolution XPS spectra and deconvolutions of (a) N 1s and (b) B 1s in N-CNO(700) and co-doped NB-CNO samples. Total quantities and percentages of (c) N1s and (d) B 1s.

The effects of B doping temperature on the shift of B1s binding energy in B-O, B-N, B-C-N configuration are presented in Figure 2.4. Clearly, B binding energies in both B-C-N and B-N configurations are gradually shifted to lower as B doping temperature increases (Figure 2.4(a)). This gradual shift suggests that N and B dopants migrate from the edge of CNOs to core.⁷⁹ At high temperature, internalized N donates more electron to the neighboring B and C-B.⁷⁷ Therefore, B 1s core electron's binding energy decreases as it gains more valence electrons. However, B atoms directly bonded to oxygen atoms are not significantly affected by this process due to high electronegativity of oxygen, resulting in negligible shift in B binding energy. Figure 2.4(b) depicts the proposed chemical configurations of N-B and N-C-B clusters at low and high temperatures. The largest number of isolated edge N-B clusters is generated at 700 °C. These edge N-B clusters may act as primary active sites for ORR.²⁵

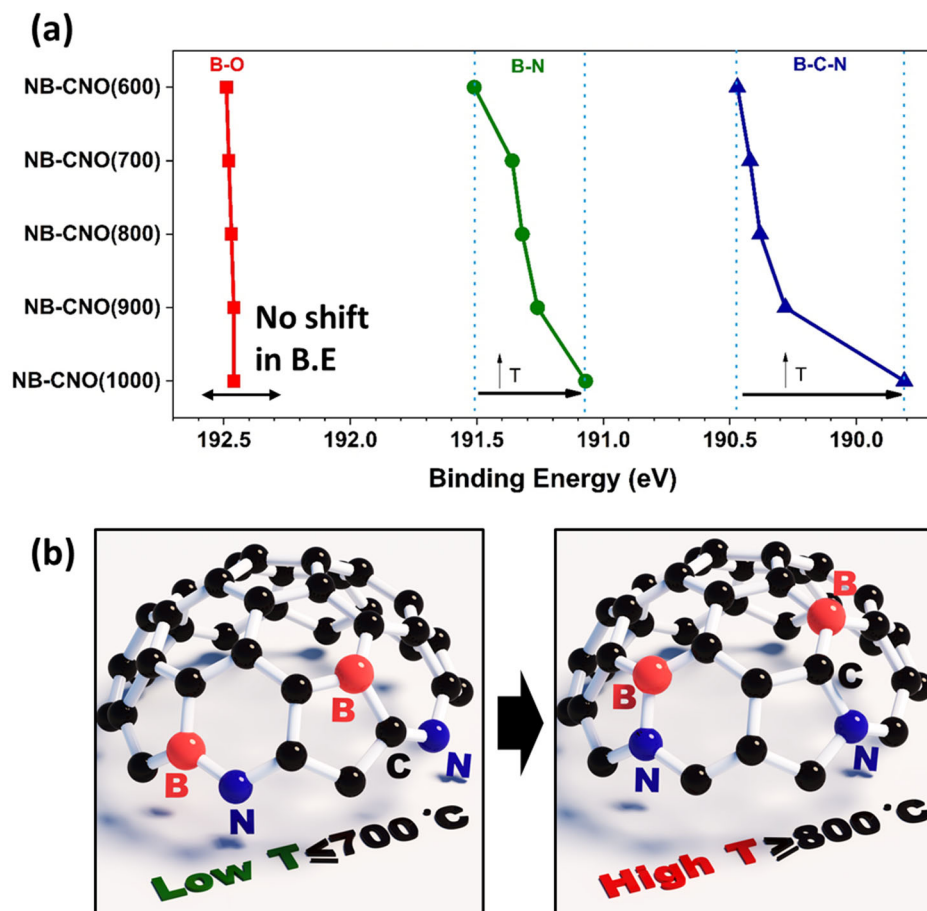


Figure 2.4 Peak shift of B1s binding energy in B-O, B-N, and B-C-N configurations of NB-CNO samples. (b) Proposed chemical structures of B-N and B-C-N at low and high B doping temperatures.

Figure 2.5 (a) shows cyclic voltammogram of NB-CNO(700) under N_2 and O_2 saturated electrolyte. The performances of doped CNOs and Pt/C are summarized in Figure 2.5(b). All N, B co-doped CNOs manifest lower onset potentials than N-CNO(700) reflecting the synergy of N and B in lowering an activation barrier towards ORR. Among co-doped samples, NB-CNO(700) surpasses other catalysts in terms of both onset potential and current density. Edge N-B clusters abundant in NB-CNO(700)

play a key role in promoting activity.²⁵ Electrocatalytic activity of each catalyst for ORR was determined by RRDE experiment in 0.1 M KOH (pH = 13). Figure 2.5(c) displays electron transfer numbers, n , and onset potentials for each sample was depicted in Figure 2.5 (d). While the RRDE was rotated (1600 rpm) for the convective flow of O₂, LSV and chronoamperometry were simultaneously performed at the disk and the ring, respectively. NB-CNO(700) yielded less than 5 % HO₂⁻ (Figure 2.5(b) top), which is very close to that of commercial Pt/C. NB-CNO(700) gives the n of 3.9, demonstrating nearly complete 4 electron transfer in ORR.

In Table 2.1, the performance of NB-CNO(700) is compared with other N, B doped catalysts reported in literature. Among various N, B co-doped carbon catalysts, NB-CNO(700) shows outstanding performance in terms of onset potential, limiting current density, and electron transfer number.

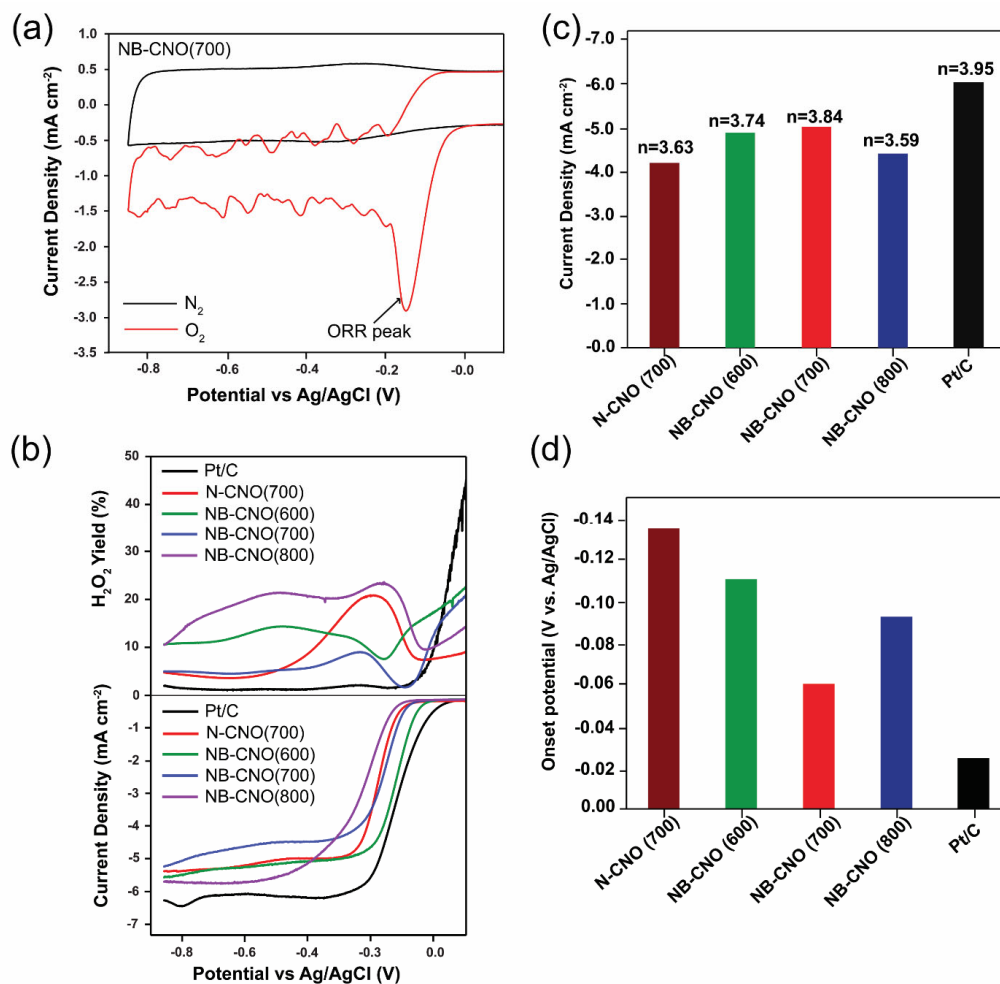


Figure 2.5 (a) Cyclic voltammetry of NB-CNO(700) in N_2 and O_2 saturated 0.1 M electrolyte, (b) peroxide yield (top), and ORR current densities (bottom) for catalysts determined by RRDE experiments and (c) limiting current densities (at -0.5 V vs. Ag/AgCl) and electron transfer number, (d) the summary of onset potentials.

Table 2.1 ORR performance of various N and B doped samples.

| Catalyst | Catalyst loading (mg/cm ²) | Rotation speed (rpm) | Scan rate (mV/s) | E ^a (V) | J ^b (mA/cm ²) | ETN ^c (<i>n</i>) |
|--|--|----------------------|------------------|--------------------|--------------------------------------|-------------------------------|
| B/N-codoped CNO ⁵⁴ | 0.5 | 2500 | 5 | -0.21 | 2.3 | 3.9 |
| B/N-codoped GNR ²⁵ | Not shown | 900 | 5 | 0.1 | 3.5 | 3.8 |
| BCN-graphene ⁷⁸ | Not shown | 1000 | 10 | 0.008 | 5.5 | 3.8 |
| Crumpled B/N- graphite ³⁷ | 0.283 | 1600 | 10 | 0.047 | 6.2 | 3.6 |
| B/N-doped graphene ⁷² | 0.283 | 1500 | 5 | 0.120 | 5.2 | 3.5 |
| B ₃ CNT-NH ₃ ⁴⁶ | 0.102 | 2500 | 10 | 0.188 | 2.4 | 2.5 |
| NBCNO-700 (This work) | 0.696 | 1600 | 5 | 0.050 | 5.5 | 3.9 |

Note: 0.1 M KOH is the electrolyte for all experiments given in the table. ^a onset potential, ^b limiting current density, ^c electron transfer number (ETN)

Although Pt is currently a state-of-the-art catalyst with lowest onset potential, highest current density, and *n* of 4, Pt-based catalysts suffer from critical issues: (1) long-term instability and (2) surface deactivation. For example, Pt/C displays gradual activity decrease in the long run due to particle aggregation, detachment and dissolution. Surface deactivation originates from the poisoning of Pt surface by products that are generated at anode and transferred across membrane (e.g. methanol in direct methanol fuel-cell).^{29, 80} The long-term stability and catalyst response against surface poisoning of NB-CNO(700) were examined in comparison with Pt/C. For 6 hours continuous operation, ORR currents of Pt/C and NB-CNO(700) were decayed about 9 % and 2 %, respectively (Figure 2.6(a)). NB-CNO(700) exhibits remarkable long-term stability. The responses of Pt and

NB-CNO(700) were monitored upon the addition of 2.5 % v/v methanol (Figure 2.6(b)). ORR currents of Pt/C and NB-CNO(700) were dropped by 45 % and 0.4%, respectively, suggesting the excellent resistance of NB-CNO against methanol poisoning.

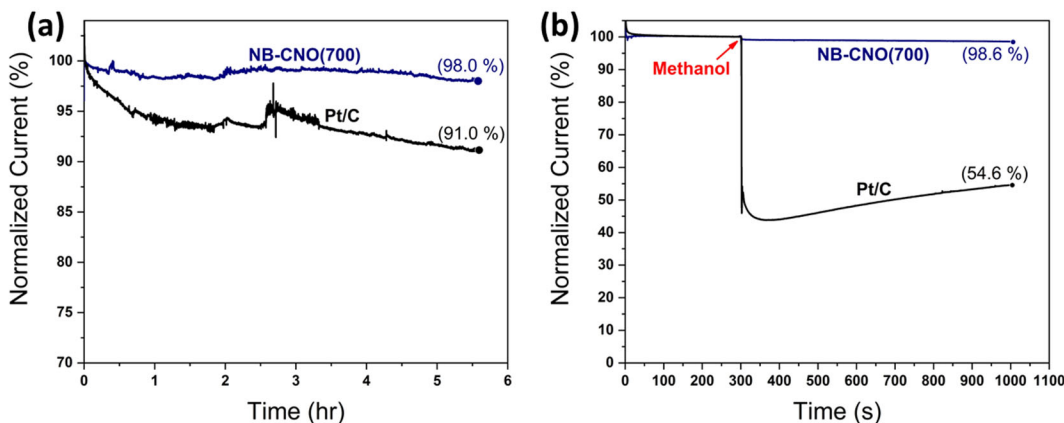


Figure 2.6 (a) Long-term stability for 6 hours and (b) electrode response upon the addition of methanol (2.5 % v/v) while -0.25 V vs. Ag/AgCl was applied.

2.6 Conclusion

In this work, we have successfully synthesized N and B co-doped CNO by sequential doping. The number of dopants, dopant chemical states, and locations of active sites were effectively modulated by manipulating annealing temperatures from 600 °C to 1000 °C. NB-CNO(700) exhibited the best ORR performance in terms of onset potential (-0.05 V) and limiting current density (5.5 mA cm^{-2}) compared to N-CNO and other co-doped CNOs. The outstanding performance comes from abundant edge N-B sites and synergistic coupling of N and B. NB-CNO(700) demonstrated complete 4-electron route for ORR with excellent durability and great tolerance against methanol crossover.

2.7 Acknowledgements

This work was supported by the National Science Foundation under DMR 1455154 (MPT, BSG), and OIA 1355438 (MPT). Partial salary was provided by NASA Kentucky under NASA award no.NN15AK28A (MPT) and the US Department of Energy under award number DE-SC0022315 (BSG). STEM characterization was conducted at the Center for Nanophase Materials Sciences, which is a DOE Office of Science User Facility.

2.8 Supporting information

2.8.1 Raman analysis

Raman spectroscopy provides information about electronic and phonon structure in doped and p-CNO.⁶³ Table S2.2 presents detailed summary of Raman analysis for all samples. 2D band intensity (I_{2D}) is sensitive to the charge carrier density because the I_{2D} is influenced by the electron-electron interactions.^{61, 81} I_{2D}/I_G ratios of samples are shown in Figure S2.2 (a). I_{2D}/I_G is a measure of change of Fermi energy level (E_f) and it is indirectly related to the amount of charge carrier density.⁵⁹ In this work, we observed that the I_{2D}/I_G ratio decreased after doping N and B compared to the p-CNO, which confirmed changing of the charge carrier density. It is worthy of mentioning that graphitic nitrogen is behaving as electron donor providing excess valence delocalized electrons to the graphene materials while pyridinic and pyrrolic nitrogen are behaving as electron acceptors.^{82, 83} Also, B doping leads to enhance electron deficiency in the carbon network. It is noted that a lower I_{2D}/I_G of all doped samples are lower than that of p-CNO. This is consistent with the increase of charge carrier concentration in the doped samples.

In summary, doping N and B increases the amount of charge carriers near the Fermi level, as compared to that of p-CNO.

The 2D band of the pristine and doped carbon materials depends on the dispersive nature and slight perturbation of electronic and/or phonon structure.⁶¹ Lin et al. reported that the 2D band for boron doped onion-like carbon (B-OLC) was downshifted (2662 cm^{-1} for undoped OLC and 2654 cm^{-1} for B-OLC), suggesting E_f is lowered after boron doping. The shift of 2D band in doped and pristine CNOs was illustrated in Figure S2.2 (b). In the case of doped CNOs, the 2D band upshifts compared to p-CNO leading to increase electron acceptors.⁸⁴ Combined with XPS analysis, 2D band position of N-CNO(700) upshifted due to single and double vacancies induced by pyridinic and pyrrolic nitrogen, respectively.^{67, 85} Upon B doping, the 2D band has further upshifted since charge carriers are high at elevated temperature due to the B and defects (removal of dopants).

Furthermore, the G band position is an important tool to probe surface charge carriers, temperature effect, and strain effect since G band can represent C-C expansion (or contractions) and changes of electronic structure. It is noted that the G bands in Figure S2.2 (c) are downshifted for all the doped and pristine CNOs compared to highly oriented pyrolytic graphite (HOPG 1582 cm^{-1}).⁸⁶ This indicates inherent tensile strain induced by the curvature which perturbs electronic band structure and therefore disturbs the Raman resonance condition of CNOs.^{86, 87} The G band is upshifted for doped CNOs at low temperatures (600 °C to 800 °C) compared to p-CNO. This observation is due to the changes in carrier concentration and the structural disorder caused by the formation new bonds with N and B dopants.⁶²

Moreover, as the annealing temperature increased, the position of G band varied. There are several reasons for this observation. 1) the loss of atoms from the CNOs' shells which may induce the relaxation of atoms around vacancies/ defects that can rearrange the CNOs structure. Therefore, the carrier's concentration decreased, and the Fermi level was rearranged. 2) a pressure hysteresis effect because CNOs are more sensitive to pressure due to the curvature effect caused by their small size.^{52, 88} As the internal pressure increases, it could become energetically favorable to distort the CNOs structure to minimize the empty space to accommodate the pressure.⁸⁸ Consequently, the doped CNOs could break their original structure therefore, NB-CNO catalysts are not potentially active at the elevated temperature. This is further illustrated XPS analysis in Figure 2.2. In brief, G band Raman shift is greatly influenced by the doping level of N and B and annealing temperature which can change the electronic and chemical structures which determine the reactivity of doped CNOs.

2.8.2 X-ray diffraction

X-ray diffraction pattern of doped and p-CNO probes the influence of doping on the microstructural variation.⁶⁹ CNOs have curved graphene layers where interlayer spacing of the layers are not uniform compared to flat hexagonal graphite layers such as GNPs. $(002)_g$ peaks of CNOs are broad and centered at around 26.0° . The interlayer spacing in CNOs is slightly larger than that of d spacing of graphite (3.36 \AA originated at 26.5°).⁸⁹ In Figure S2.3(b), the position of $(002)_g$ diffraction peak was shifted towards higher 2θ after boron doping at 600°C and 700°C , implying a decrease in the d spacing

of CNOs layers. This may be due to the disruption of the curved surface of CNOs. At the elevated temperature, this peak was shifted back to the original position.

2.8.3 Electrochemical measurement

The overall electron transfer number (n) for one oxygen molecule was calculated from the slope of a Koutecky-Levich (K-L) plot as shown in the equation 2.1:

$$1/j_D = 1/j_K + 1/B\omega^{1/2} \quad \text{Equation 2.1}$$

where, j_D = measured current (A) on RDE,

j_K = kinetic current (A) at constant potential,

ω = rotating speed in rpm,

B = slope for K-L equation which can be calculated using the equation 2.2.

$$B = 0.2nFA\nu^{-1/6}C_{O_2}D_{O_2}^{2/3} \quad \text{Equation 2.2}$$

where, 0.2 constant is multiplied when the rotation speed is denoted in rpm,

n = number of electrons,

F = Faradaic constant (96485 C/mol),

A = Surface area of the electrode,

ν = Kinetic viscosity of 0.1 M KOH (0.01 cm²/s),

C_{O_2} = Bulk concentration of O₂ in the electrolyte (1.2 × 10⁻⁶ mol/cm³),

D_{O_2} = Diffusion coefficient of O₂ molecule in 0.1 M KOH solution.

The percentage of the HO₂⁻ was calculated using equations 2.3 and 2.4.

$$n = 4 \times \frac{I_d}{I_d + I_r/N} \quad \text{Equation 2.3}$$

$$\%HO_2^- = 200 \times \frac{I_r/N}{I_d + I_r/N} \quad \text{Equation 2.4}$$

where, I_d = disk current, I_r = ring current, and N = current collection efficiency of the Pt ring (0.42).

Table S2.1 The summary of Raman analysis.

| Sample | D-band shift (cm ⁻¹) | G-band shift (cm ⁻¹) | 2D-band shift (cm ⁻¹) | I _D /I _G | I _{2D} /I _G | 2D-band FWHM (cm ⁻¹) |
|--------------|----------------------------------|----------------------------------|-----------------------------------|--------------------------------|---------------------------------|----------------------------------|
| CNOs | 1334 | 1572 | 2665 | 1.1 | 0.7 | 72.4 |
| Ox-CNO | 1336 | 1573 | 2668 | 1.2 | 0.5 | 64.7 |
| N-CNO(700) | 1338 | 1580 | 2672 | 1.4 | 0.4 | 78.1 |
| NB-CNO(600) | 1336 | 1574 | 2669 | 1.2 | 0.4 | 74.4 |
| NB-CNO(700) | 1337 | 1574 | 2669 | 1.3 | 0.4 | 63.3 |
| NB-CNO(800) | 1336 | 1572 | 2671 | 1.2 | 0.6 | 58.2 |
| NB-CNO(900) | 1339 | 1577 | 2673 | 1.3 | 0.5 | 63.3 |
| NB-CNO(1000) | 1339 | 1580 | 2677 | 1.5 | 0.4 | 69.4 |

Table S2.2 The atomic percentages of C, O, N.

| Sample | C (at.%) | O (at.%) | N (at.%) | B (at.%) |
|--------------|------------|-----------|-----------|-----------|
| N-CNO(700) | 95.9 ± 0.1 | 1.3 ± 0.1 | 2.9 ± 0.1 | |
| NB-CNO(600) | 94.3 ± 0.3 | 2.1 ± 0.4 | 2.7 ± 0.1 | 0.9 ± 0.1 |
| NB-CNO(700) | 93.2 ± 0.1 | 2.4 ± 0.2 | 2.7 ± 0.1 | 1.1 ± 0.3 |
| NB-CNO(800) | 93.5 ± 0.1 | 2.5 ± 0.1 | 1.9 ± 0.2 | 1.4 ± 0.1 |
| NB-CNO(900) | 94.9 ± 0.2 | 2.6 ± 0.2 | 1.1 ± 0.3 | 0.9 ± 0.1 |
| NB-CNO(1000) | 95.9 ± 0.3 | 2.4 ± 0.1 | 0.7 ± 0.1 | 0.9 ± 0.3 |

Table S2.3 XPS N 1s related chemical states in the samples based to area of the peak.

| Sample | N-B(%) | N-pyridinic | N-pyrrolic(%) | N-Graphitic(%) | N-O(%) |
|--------------|--------|-------------|---------------|----------------|--------|
| N-CNO(700) | 0 | 42 | 30 | 18 | 10 |
| NB-CNO(600) | 19 | 33 | 31 | 12 | 5 |
| NB-CNO(700) | 25 | 31 | 25 | 12 | 7 |
| NB-CNO(800) | 17 | 39 | 28 | 10 | 6 |
| NB-CNO(900) | 13 | 43 | 24 | 12 | 9 |
| NB-CNO(1000) | 7 | 50 | 24 | 11 | 8 |

Table S2.4 XPS B 1s related chemical states in the samples based on the area of the peak.

| Sample | B-C-N(%) | B-N(%) | B-O(%) |
|--------------|----------|--------|--------|
| N-CNO(700) | 0 | 0 | 0 |
| NB-CNO(600) | 30 | 50 | 20 |
| NB-CNO(700) | 32 | 48 | 20 |
| NB-CNO(800) | 34 | 44 | 22 |
| NB-CNO(900) | 38 | 44 | 18 |
| NB-CNO(1000) | 30 | 45 | 25 |

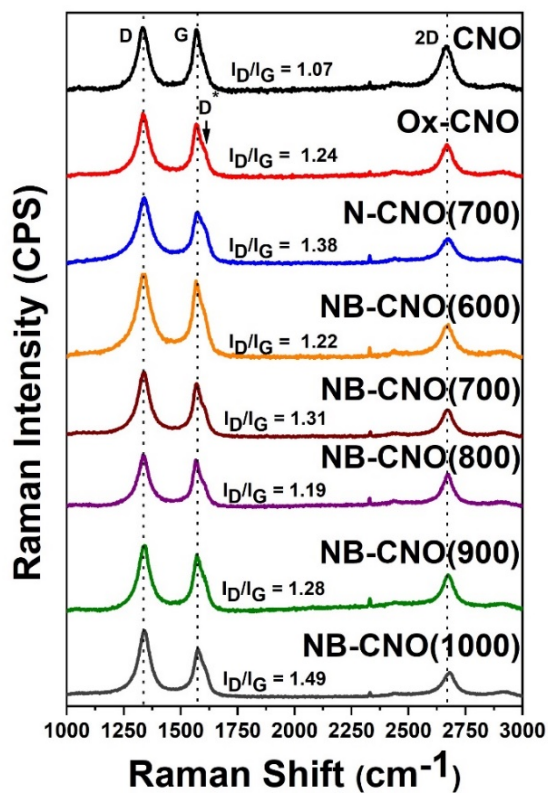


Figure S2.1 Raman spectra of CNOs, Ox-CNO, N-CNO(700), NB-CNO(600-1000).

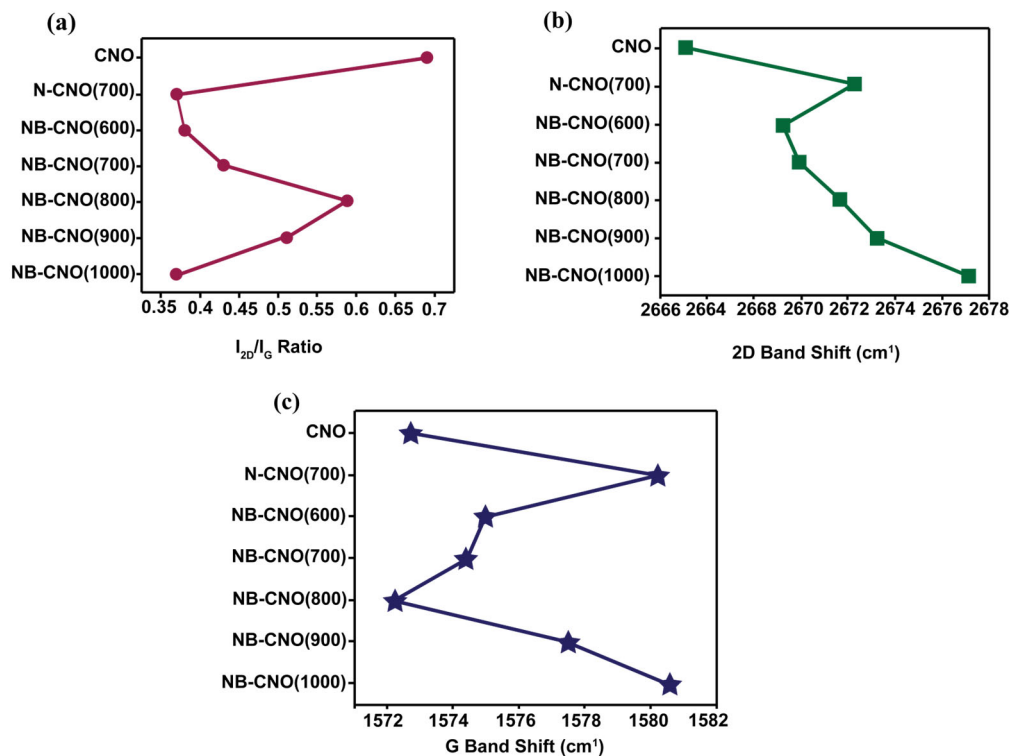


Figure S2.2 (a) I_{2D}/I_G ratio, (b) 2D band shift, and (c) G band shift.

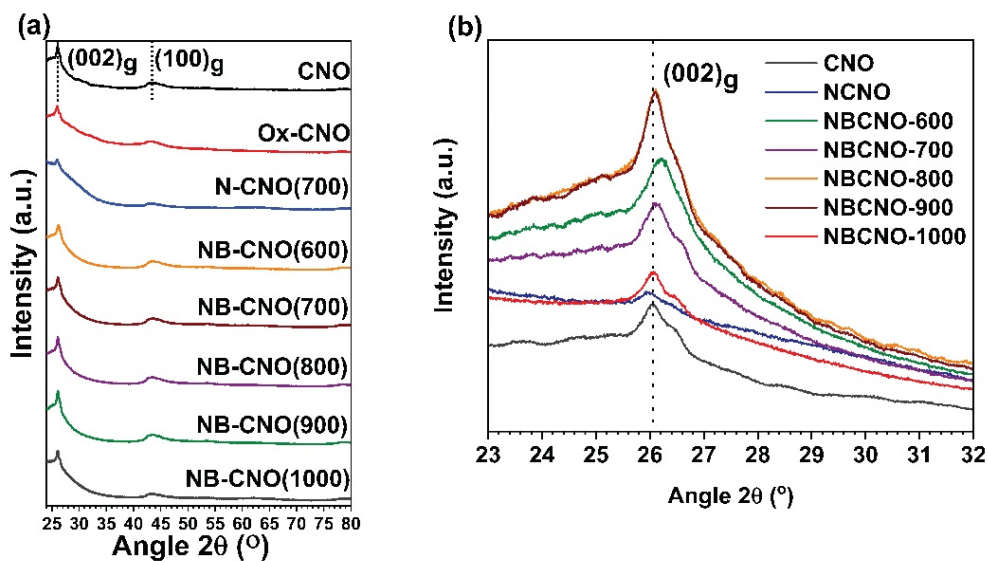


Figure S2.3 (a) X-ray diffraction patterns and (b) zoomed-in (002) peak of CNOs, N-CNO(700) and all NB-CNO samples.

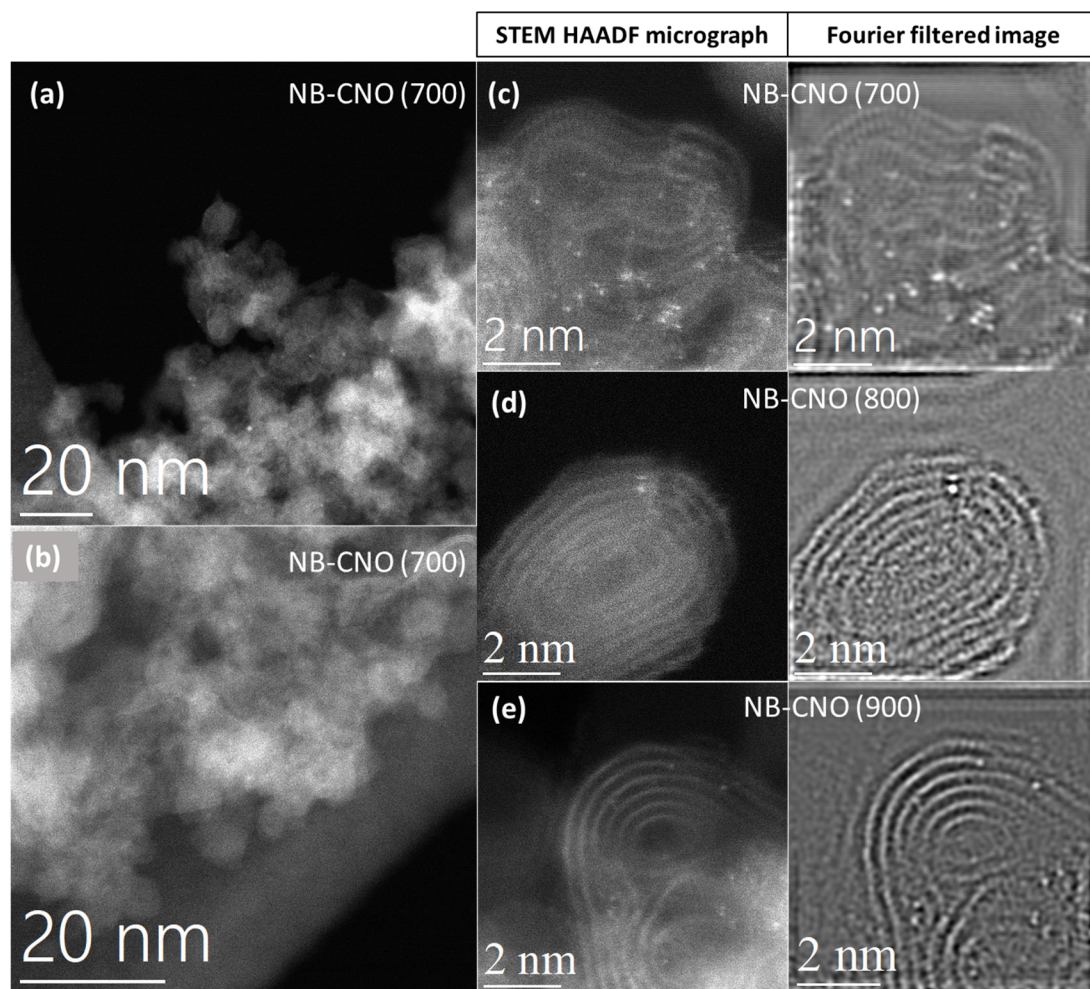


Figure S2.4 (a-b) Low-magnification STEM HAADF micrographs of NB-CNO (700). (c-e) High-magnification STEM HAADF micrographs and their respective Fourier filtered images of NB-CNO (700), NB-CNO (800), and NB-CNO (900), respectively.

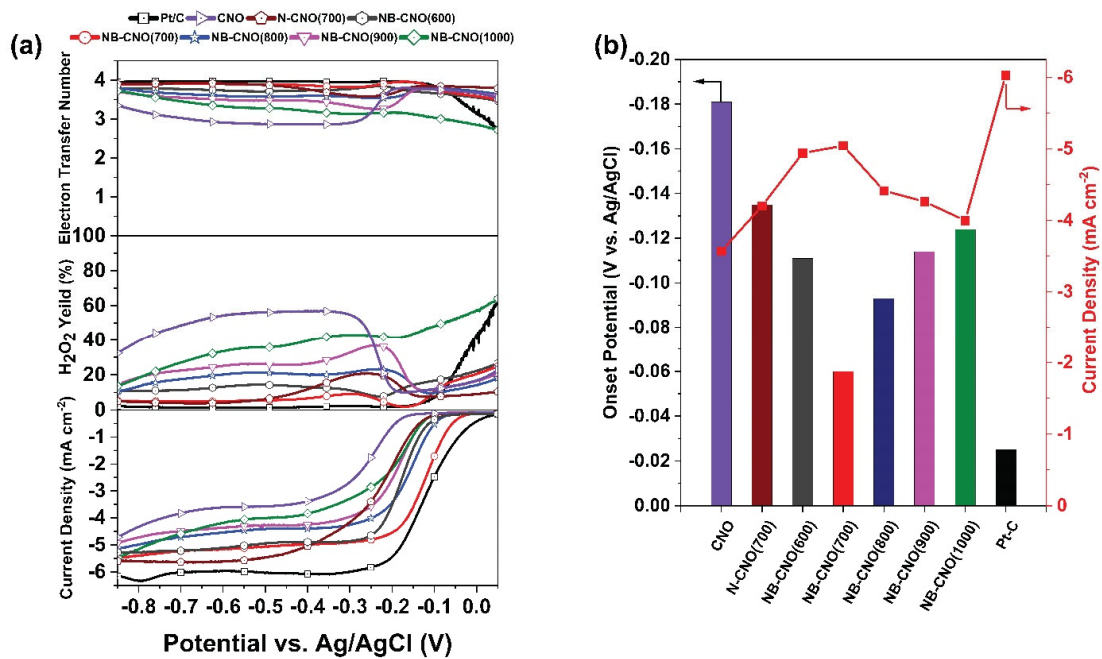


Figure S2.5 (a) Results of RRDE measurement and (b) comparison of onset potentials and limiting current densities (at -0.5 V vs. Ag/AgCl) of all samples.

CHAPTER 3. COPPER NANOPARTICLES SUPPORTED ON NITROGEN DOPED CARBON NANO-ONIONS FOR OXYGEN REDUCTION REACTION: SYNERGISTIC EFFECTS OF NITROGEN AND CARBON NANO-ONIONS

The author would like to thank Dr. Yang-Tse Cheng and Jacob Hemple for their help with Kelvin probe force microscopy analysis (KPFM).

3.1 Introduction

Electrocatalysis is a promising technology for advanced chemical synthesis and energy conversion processes such as water splitting, greenhouse CO₂ gas conversion, and fuel cells.⁹⁰ Electrocatalysis has several advantages over other traditional processes (e.g., thermal, chemical, etc) such as direct control of voltage for optimal efficiency and selectivity, promoted mass transport by adopting an advanced electrolyzer, and easy separation of products from a reactor.⁹¹ In such electrochemical processes, catalysts are one essential component to minimize the kinetic barrier of the reaction and to increase energy efficiency.^{92, 93} Platinum-group metals (PGMs) are the most frequently used electrocatalysts for energy and chemical conversion devices.^{29, 90, 94-96} However, sustainable utilization of PGMs for electrocatalysis is greatly challenged by the cost, scarcity, and the instability of these materials,⁹⁷⁻⁹⁹ that are aggravated by the recent interruption in critical mineral supply chains.^{96, 100}

So as to solve this challenge, it is imperative to replace PGMs with efficient and stable non-noble materials. One promising approach is to manipulate the interaction between non-noble metal nanostructures and supports.¹⁰¹⁻¹⁰⁵ The performance and long-term stability of catalysts are affected by catalyst particle size, crystalline planes, and dispersion.¹⁰⁶ Considerable efforts have been made to reduce the size of metal particles

and to engineer the morphology of the catalyst to reach low-coordinated metal sites at the surface.^{101, 102, 105, 107, 108}

Heteroatom doped (N, S, B etc.) carbon supports have received considerable attentions because of their potential as a support to enable improved dispersion of metal nanoparticles.^{83, 105, 108, 109} Incorporation of these dopants in carbon surface may modify acid-base character, hydrophilicity-hydrophobicity, and electronic properties of carbon surface.¹¹⁰ Qiao et al. reported that the ORR activity can be boosted by the cooperative effect of copper and nitrogen in a Cu oxide/N-doped reduced graphene oxide catalysts.¹¹¹ Previous studies reported that nitrogen dopants act as nucleation sites of metal nanoparticles on the carbon support.^{112, 113} Nitrogen dopants also promote the dispersion of metal nanoparticles as well those modifications can modulate the Fermi level, enhance the chemical activity, and tend to trap metal atoms.^{67, 95, 101, 114} Literature reported that the most favorable sites for Cu nucleation are the rough edges of carbon support.¹⁰¹ This demonstrates that the availability of the edge pyridinic and pyrrolic nitrogen in the host material can play a crucial as electron donors to enhance the interaction between the support and metal nanoparticles.^{109, 110, 115}

Herein, we investigated the role of nitrogen doping on carbon nano onions (CNO) for copper deposition and catalytic activity. We here report the results of the study conducted on CNO, nitrogen doped CNO (NCNO), and NCNO supported Cu nanoparticles (Cu-NCNO) for the oxygen reduction reaction in alkaline medium. Our objectives are to demonstrate the effect of nitrogen on the reduction of the particle size and how Cu-N doped CNO's surface potential (or work function) affects the catalytic properties. The morphology, microstructure, and chemical states of nitrogen doped

electrocatalysts were characterized by AFM, TEM, SEM, Raman, and X-ray photoelectron spectroscopy. Our results show that nitrogen heteroatom on the host CNO reduces the size of the metal nanoparticles to boost the electrocatalytic performance. Based on our experimental results, we conclude that the copper nanoparticle size is ~2 nm which is located in close proximity to nitrogen. These findings provide novel insights on the effect of nitrogen on CNO toward ORR in the alkaline electrolyte.

3.2 Experimental

3.2.1 Synthesis of CNO, Ox-CNO, and N-CNO

Carbon nano-onions were derived by annealing nanodiamond powders (Nanostructured and Amorphous Materials, Inc (Dynalene NB50)). After annealing CNO were subject to chemical oxidation to produce oxidized CNO (Ox-CNO). This was done by refluxing CNO with HNO₃. For this purpose, 100 mg CNO were mixed with 50 mL HNO₃ (ACS grade, 68.0 -70.0 %) and 50 mL de-ionized (DI) water in a three-neck flask and sonicated for 1 hour to prepare a homogenous mixture. After that, the mixture was refluxed at 110°C for 4 hours and 30 minutes. Ox-CNO was washed with DI water until the mixture became neutral. Then, Ox-CNO was dried in an oven at 60 °C overnight.

N-CNO were prepared by thermally annealing Ox-CNO with urea (Sigma Aldrich, ACS reagent, 99.0-100.5%). Typically, 100 mg of Ox-CNO were completely ground with 500 mg of urea and mounted on a quartz boat. Then, the quartz boat with the mixture was loaded in a tube furnace (Thermo Scientific Lindberg/BlueM Mini-Mite™ Tube Furnace). After evacuating the furnace for 30 minutes, argon gas was introduced to remove any remaining moisture and oxygen. The mixture was then thermally annealed at

700°C for 3 hours with the annealing rate of 3°C/min under an argon atmosphere in the furnace. After the annealing process, the tube furnace was cooled to room temperature under the same condition. The powder obtained from the heating treatment was centrifuged with DI water two times to remove any soluble impurities. The purified powder was dried in the oven at 60 °C overnight, which is denoted as NCNO (700).

3.2.2 Synthesis of Cu-NCNO (Cu-NCNO)

In a typical synthesis, 5 mg of copper acetate (Sigma Aldrich) and 95 mg of NCNO was mixed with tetra hydro furan (THF) (Sigma Aldrich) by sonicating it 1 hour to get a homogeneous solution. The solution was loaded in a Teflon vessel that was sealed and placed in a vacuum oven. The temperature of the oven was maintained at 75°C for 24 hours. When the time was finished, the mixture was placed in an oven at 60°C overnight to evaporate the extra solvent and further dry. After that, the dried powder was loaded into a quartz boat and thermally annealed under 5% H₂ in the tube furnace at 300 °C for 15 min to remove the extra precursor ligand (acetate from copper acetate) and reduce copper nanoparticles. After the heat treatment, the tube furnace was cooled to room temperature, the product was powder, washed with DI water. The purified product was dried in the oven at 60°C for 24 hours. Cu-CNO was synthesized by following the same method with carbon nano onions instead of NCNO. Acid treatment was done for 5 with O₂-saturated 5% HCl to obtain acid washed samples as Cu-CNO-AF and Cu-NCNO-AF.

3.2.3 Material characterization

Raman spectroscopy was performed with a Thermo Scientific DXR micro-Raman spectrometer. A diode-pumped NdYVO₄ laser was used as excitation source at 532 nm excitation and with a power 5 mW. The elemental composition and the chemical states of the prepared samples were determined by X-ray photoelectron spectroscopic measurement (XPS Thermo Scientific K-alpha) which uses an aluminum monochromatic X-ray source (energy of 1,486.6 eV) and an electron flood gun for charge neutralization. Wide survey scans were performed at a pass energy of 160 eV and high-resolution scans were performed at a pass energy of 20 eV. The XPS analyzed spot diameter was 400 μm. The crystalline structure of all samples was analyzed using BRUKER AXS X-ray spectrometer equipped with Cu tube (1.54 Å) and energy dispersive LYNXEYE (1D mode) detector, increment 0.01°. TEM, HRTEM, STEM, and EDS analysis were investigated using transmission electron microscope (TEM FET Talos F200X) which was operated at 200 KeV. Amplitude Modulated Kelvin Probe Force Microscopy (AM-KPFM) measurements were taken on a Bruker Dimension icon housed in a glovebox (O₂, H₂O < 1 ppm) using their electrical lift mode. Doped CNO samples were first immersed in isopropanol. They were then subjected to 15 minutes of ultrasonication. The solutions were then dropped onto silicon wafers. After the solvent dried, the region left behind contained clumps of nanoparticles which were then imaged using AM-KPFM. The lift height was chosen to be 35 nm to improve the lateral resolution.

3.2.3.1 Electrochemical measurements

These electrochemical measurements were recorded on a CHI760 D Potentiostat (CH Instruments, Inc., USA). Rotating ring disk electrode (RRDE) was polished with

0.05-micron Alumina powder before a catalyst drop cast. Then, 2 mg of catalyst, 20 μL of Nafion (FuellCellStore, ~ 5 wt. %), and 1 ml of DI water were mixed and sonicated for 1 hour to prepare the homogenous catalyst ink (2 mg/ml). Subsequently, 60 μL of the ink was drop cast onto the disk electrode (geometric surface area: 0.126 cm^2). The electrode was dried in the oven at 60°C overnight. All the current densities in the electrochemical curves were normalized to the geometric area of the electrode. The potential reported in this work were referred to the RHE, based on the Nernst equation 3.1:

$$E(\text{vs. RHE}) = E(\text{vs. Ag/AgCl}) + .0592 \times \text{pH} + 0.222\text{V} \quad \text{Equation 3.1}$$

The electrolyte, 0.1 M KOH (VWR chemicals BDH) was saturated by purging N_2 for approximately 30 min before the experiment. After that, Ag/AgCl, Pt wire, and RRDE were placed as reference (RE), counter (CE), and working (WE) electrodes respectively. The working electrode was activated by 40 CV cycles under a potential range from 0.0 to 1.0 V at a scan rate of 50 mV s^{-1} . Cyclic voltammograms (CVs) were collected in the presence of N_2 as a control test to compare. Subsequently, the electrolyte was saturated with O_2 for 30 min. CVs, linear sweep voltammograms (LSVs) with a rotating disk electrode (RDE) were collected. The CVs were collected at 20 mV/s scan rate and RDE was conducted at 5 mV/s scan rate with the rotation speed of 400 rpm, 800 rpm, 1200 rpm, 1600 rpm, 2000 rpm, 2400 rpm, 2800 rpm, 3200 rpm, and 3600 rpm. Koutecky-Levich (K-L) plots (J^{-1} vs $\omega^{-1/2}$) were analyzed at various electrode potentials. The electron transfer number (n) was calculated by based on the K-L equation 2.1 and

2.2.¹¹¹ RRDE measurement at 1600 rpm were used to obtain the Tafel plot for Cu-NCNO and Pt/C.

3.3 Results and discussion

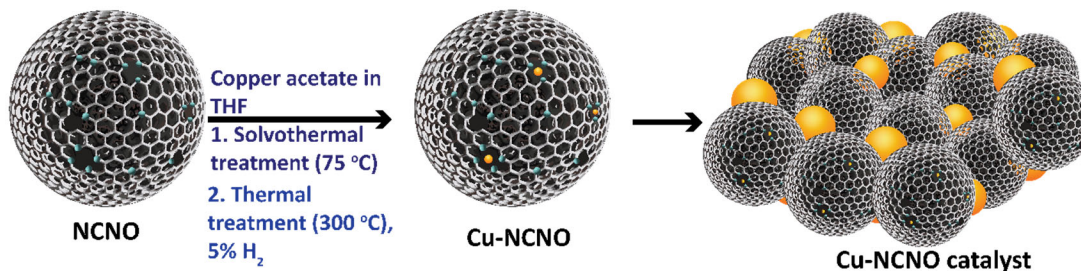


Figure 3.1 A schematic illustration of Cu-NCNO synthetic procedure (gray, carbon; blue, nitrogen; orange, copper).

Untreated carbon-based materials are not suitable for attaching metal nanoparticles because of their inertness and hydrophobic surface.¹¹⁰ Thus nitrogen doped CNOs (N-CNOs) were synthesized to deposit copper nanoparticles in this study. Experimental and theoretical studies reported the effectiveness of substitutional doping in tuning physical and chemical properties of CNOs.¹¹² For example, nitrogen incorporation enhanced polarity and basicity of catalyst surface, that would promote the nucleation and growth of catalytic particles.¹¹⁶ Nitrogen-doped CNOs were prepared by thermally treating the mixture of urea and oxidized carbon nano-onions at 700 °C with urea under the flow of argon. During thermal treatment, urea decomposes into NH₃ and CO₂, NH₃ further reacts with oxygen functional groups of oxidized CNOs (Ox-CNO) to form N-C bonds and are then internalized.¹¹⁷

Figure 3.1 depicts synthetic procedure of Cu-NCNOs. Cu-NCNOs were synthesized through a solvothermal treatment for 18 hours in tetrahydrofuran at 75°C.^{118, 119} Copper (II) acetate was used as a precursor for Cu growth. Presumably, Cu²⁺ is nucleated at the sites of pyridinic N and pyrrolic N (Figure 3.1) due to their Lewis basicity and continues to grow into Cu nanoparticles. For the removal of unreacted ligands as well as complete reduction of unbound copper ions, the powder was further annealed in the furnace at 300 °C under the flow of H₂/Ar gas (5:95 v:v).¹²⁰ Afterwards, Cu-NCNOs were washed with acid. Cu-NCNOs before and after the acid washing are denoted as Cu-NCNO-BF, and Cu-NCNO-AF, respectively.

XRD pattern of Cu-CNO and Cu-NCNO have shown in Figure S3.1. Both Cu-CNO and Cu-NCNO display peaks at 26°, 44°, 62°, and 78° for (002), (100), (004), and (110), planes of graphitic materials, respectively. In addition, Cu-CNO presents a sharp peak at 36°, that corresponds to Cu (111) plane. On the contrary, Cu-NCNO doesn't show any characteristic peak of copper. Based on EDS, TGA, and XPS results in the later section, the absence of copper peaks should be interpreted as the indication of very small Cu particles in Cu-NCNO. The size of copper particles in Cu-NCNO is smaller than the detection limit (~3 nm in diameter) of XRD analysis. Basicity of pyridinic-N and pyrrolic-N as well as electron-rich concentric surface of carbon onions create a unique environment that promotes the nucleation of copper. Furthermore, the strong interaction between Cu-N and between copper nanoparticles and concentric carbon surface stabilize particles, preventing their growth into bigger particles.

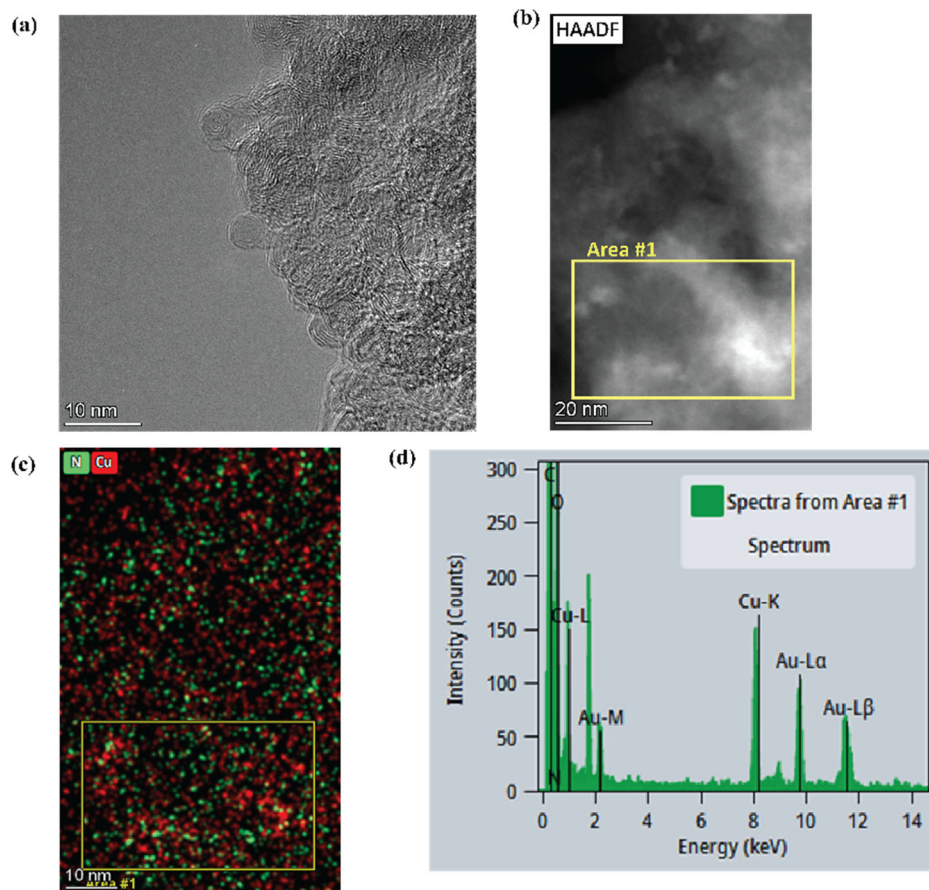


Figure 3.2 (a) HR-TEM image (b) HAADF-STEM image (yellow square represent the selected area for the EDS) (c) EDS mapping of nitrogen and Cu, and (d) EDS spectrum for elemental analysis.

High-resolution transmission electron microscopy (HR-TEM) of Cu-NCNO is shown in Figure 3.2a, revealing onion-like, concentric shells of carbon onions. The structure of CNOs with multi-layered concentric shells is retained during the synthesis. High-angle annular dark field (HAADF) is a STEM imaging mode that collects scattered electrons by an annular detector. In HAADF-STEM image, the scattering intensity of electrons on this detector is approximately proportional to the atomic number (Z) of the

element.⁴⁹ Therefore copper atoms in the image are brighter than the region of concentric carbon shells. Individual Cu atoms and Cu nanoparticles are identified in Figure 3.2b and 3.2c. The diameter of Cu nanoparticle has the range of 1.8 – 2.1 nm. This diameter is beyond the detection limit of XRD (Figure S3.1). The EDS mapping of N and Cu in Figure 3.2c suggests that both elements are uniformly distributed in the sample. The EDS spectrum in Figure 3.2d displays the presence of C, O, N and Cu in CNOs, verifying that N dopants serve as nucleation sites for Cu. Several Au peaks in Figure 3.2d come from Au layer coated on TEM substrates.

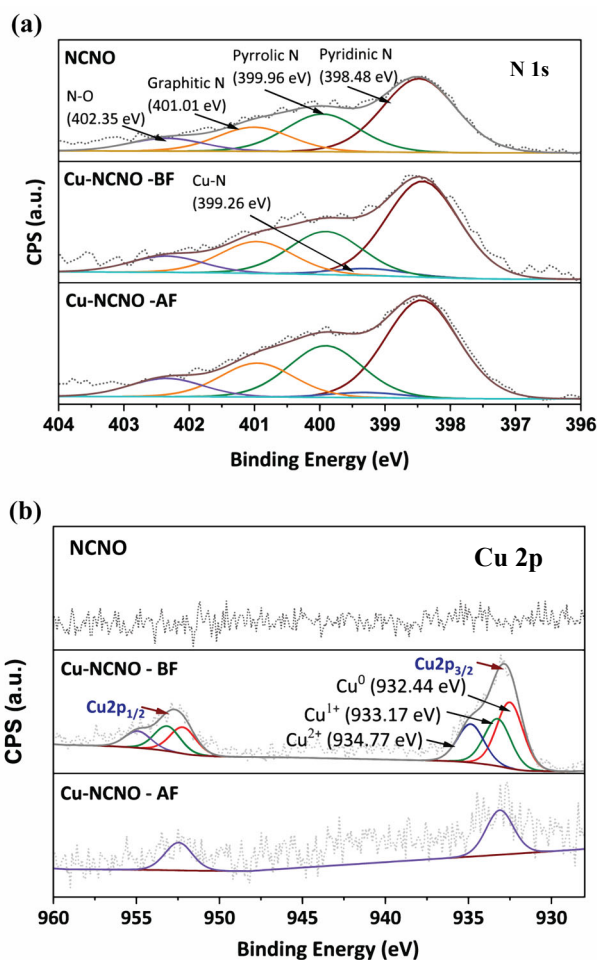


Figure 3.3 High resolution XPS spectra of (a) N 1s, (b) Cu 2p.

XPS analyses were performed to determine elemental composition and chemical state of the catalysts. XPS survey scans are shown in Figure S3.2 and elemental contents are summarized in Tables S3.1 and S3.2. All catalysts contain C and O as major elements. Besides C and O, Cu-NCNO shows the presence of both N and Cu, which is consistent with the EDS analysis (Figure 3.2c and 3.2d). The contents of Cu in Cu-NCNO-BF, Cu-NCNO-AF, Cu-CNO-BF, and Cu-CNO-AF are 1.54 at.%, 0.10 at.%, 0.14 at.%, and 0.02 at.% respectively. Acid washing removed nearly all the copper from both Cu-NCNO and Cu-CNO, indicating the copper is attached to the surface of support. The contents of N in N-CNO, Cu-NCNO-BF, and Cu-NCNO-AF are 3.9 at.%, 3.8 at.% and 3.5 at.%, respectively. There is a negligible change of N in Cu-NCNO after acid washing.

Figures 3.3(a) and 3.3(b) show high-resolution XPS N1s and Cu2p spectra of N-CNO (top), Cu-NCNO-BF (middle), and Cu-NCNO-AF (bottom), respectively. The analysis of N chemical states present in catalysts is summarized in Table S3.2. In Figure 3(a), each XPS N1s spectrum is deconvoluted into 4 basis functions centered at 398.5 eV, 400.0 eV, 401.0 eV, and 402.4 eV, that are assigned to pyridinic N, pyrrolic N, graphitic N, and N-O, respectively.⁶⁷ In addition to the four peaks, a broad peak centered at 399.3 eV appears with small intensity in both Cu-NCNO-BF and Cu-NCNO-AF. This peak is assigned to N (either pyridinic N or pyrrolic N) that is directly bound to Cu. After acid washing, this N-Cu peak is still retained but lesser intensity, indicating that N-Cu may be stable in acid washing.

In Figure 3.3b, NCNO shows no trace of Cu. In both Cu-NCNO-BF and Cu-NCNO-AF, Cu 2p XPS spectra have two groups of peaks, Cu 2p_{1/2} and Cu 2p_{3/2}. The XPS Cu 2p_{3/2} spectrum is deconvoluted into 3 basis functions centered at 932.44 eV, 933.2 eV

and 934.8 eV, that are assigned to Cu(0), Cu⁺, and Cu²⁺, respectively. While Cu(0) is from bulk copper nanoparticle, Cu⁺ (933.2 eV) is due to copper atoms at the bottom of nanoparticles that are directly bound to N as Cu-N. This is in a good agreement with previous reports.^{103, 109, 121} Cu²⁺ may be from copper oxide. After acid treatment with O₂-saturated 5 % HCl, both Cu(0) and Cu²⁺ peaks disappear while Cu-N is retained. This implies the strong interaction between Cu and N. The Cu-N interaction and high CNO surface-strain promote the nucleation of small Cu particles for enhanced ORR activity.

Thermogravimetric analysis (TGA) was conducted to measure the total amount of copper present in catalysts. Before acid washing, TGA analysis (Figure S3.3) indicates 4 wt% of Cu content in Cu-NCNO. This amount is consistent with XPS showing 3.5 wt% Cu. In TGA curves, Cu-NCNO decomposes at 300 °C while Cu-CNO decomposes at 450 °C. This demonstrates that well-dispersed and small copper nanoparticles catalyze thermal oxidation of Cu-NCNO.

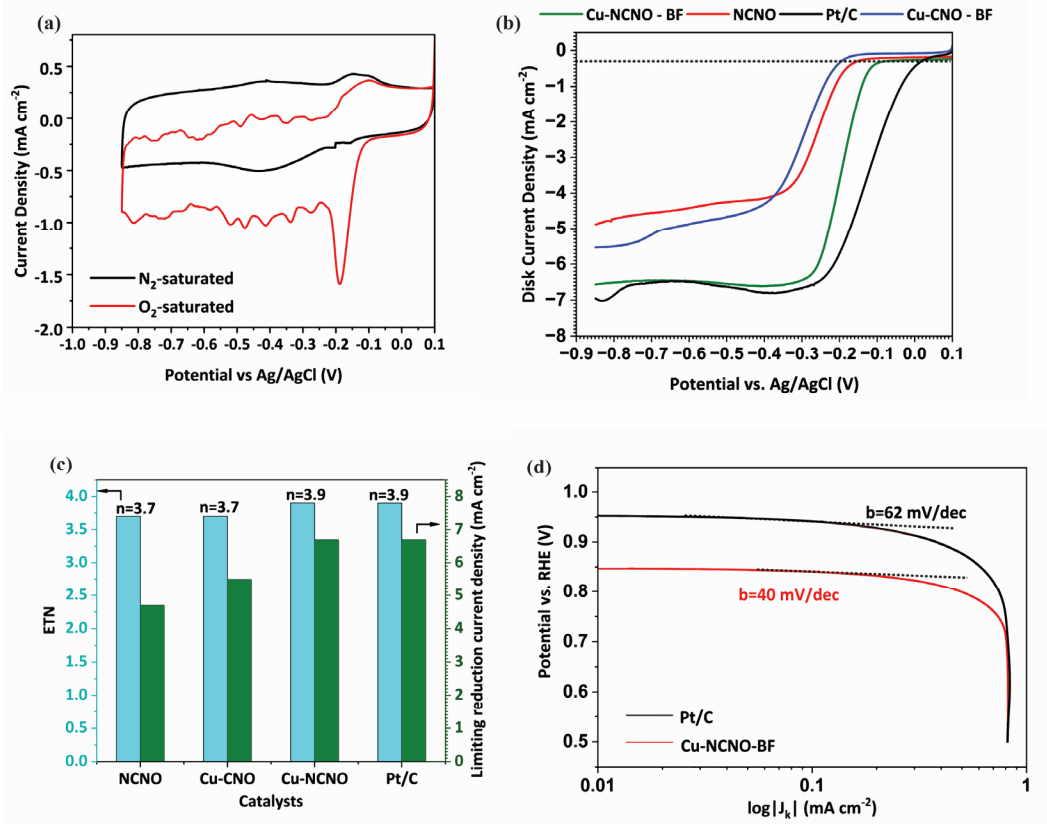


Figure 3.4 ORR performance of the Cu-NCNO, NCNO and Pt/C (a) CV curves of the Cu-NCNO catalyst in N_2 - and O_2 -saturated 0.1 M KOH electrolyte, (b) RRDE for Cu-NCNO, NCNO, and Pt/C before acid washed at rotation rate 1600 rpm (scan rate 5 mV/s), (onset potentials are -0.08,-0.15, 0.03, -0.2 V for Cu-NCNO-BF, NCNO, Pt/C, and Cu-CNO-BF, respectively at -0.3 mA cm^{-2}), (c) electron transfer number, (d) Tafel plots of Cu-NCNO-BF and Pt/C catalysts (J_k is kinetic current density).

Catalytic performances of catalysts for ORR were evaluated by cyclic voltammetry (CV), rotating disk electrode (RDE), and rotating ring disk electrode (RRDE) measurements. All electrochemical experiments were performed in alkaline electrolyte, 0.1 M KOH. The solution was saturated with either N_2 or O_2 prior to each measurement. CV curves of Cu-NCNO in N_2 - and O_2 -saturated solution are shown in

Figure 3.4(a). In the CV of O₂-saturation, Cu-NCNO clearly shows a reduction peak originating approximately at -0.2 V vs Ag/AgCl. ORR peak of Cu-NCNO locates ~17 mV higher than that of NCNO by ~ 20mV (Figure S3.4), showing that the improved activity of Cu-NCNO. Linear sweep voltammetry (LSV) graphs of NCNO, Cu-NCNO, Pt/C and other catalysts have been depicted in Figure 3.4(b) and Figures S3.5 and S3.6, respectively. After nitrogen is introduced to the carbon nano onions, nitrogen could act as a catalytic site for ORR as well as a nucleation site for copper deposition. This performance originates due to the different nitrogen configurations (pyridinic, pyrrolic, and graphitic). It is noted that NCNO exhibits a high catalytic activity for ORR compared to Cu-CNO. The onset potential of NCNO (-0.15 V vs. Ag/AgCl) for ORR shifts 50 mV toward positive direction compared to Cu-CNO (-0.2 V vs. Ag/AgCl). Furthermore, after introducing copper into NCNO, Cu-NCNO shows the onset potential at -0.08 V vs Ag/AgCl with the limiting current density about 6.5 mA cm⁻².

The Tafel plots in Figure 3.4(d) show that the Tafel slopes of Cu-NCNO and Pt/C are 40 mVdec⁻¹ and 62 mV dec⁻¹, respectively. Consequently, the reaction mechanism of ORR on Cu-NCNO is comparable to the Pt/C catalyst. Figure 3.4(d) represents the Tafel plots of log J_k (mA cm⁻²) vs. electrode potential, plotted from the polarization curves of Figure 3.4(b) measured at rotation rate of 1600 rpm. Generally, this plot is useful for evaluating kinetic parameters of catalysts. In the low overpotential region, the disk current density is independent of the mass transfer limitation therefore, the current densities are considered as electrochemical kinetic current densities. The figure has depicted that the reaction mechanism of ORR on Cu-NCNO is comparable to the Pt/C

catalyst. Furthermore, this kind of slope variation generally can be explained with respect to the change in the coverage degree of adsorbed oxygen.¹²²

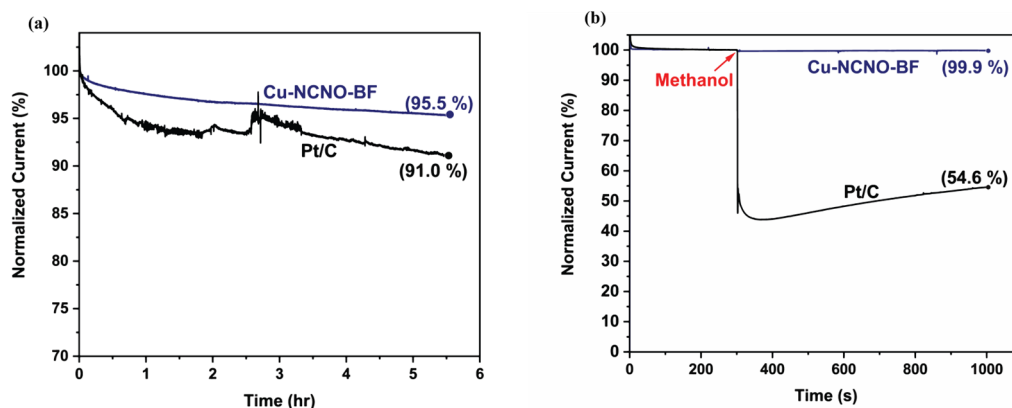


Figure 3.5 RRDE at 1600 rpm for Cu-NCNO and Pt/C (a) durability test (b) methanol tolerance test.

One of the most critical issues in PGM catalysts are poor long-term stability and surface deactivation. In the long term, Pt activity gradually deteriorated, due to particle detachment, dissolution, and agglomeration. Pt catalysts in direct methanol fuel cells may experience severe deactivation by methanol transported from anode through the membrane. Figure 3.5(a) shows the stability of Cu-NCNO in comparison with Pt/C. for 5 hours of operation, ORR currents of Cu-NCNO and Pt/C decay about 4.5 % and 9 %, respectively, showing the improved stability of Cu-NCNO. The responsiveness of catalyst against surface deactivation is also shown in Figure 3.5(b). For this experiment, methanol (2.5 % v/v) was injected into the solution. Cu-NCNO and Pt/C show the decays of currents by 0.1 % and 45.4%, respectively, indicating remarkable tolerance of Cu-

NCNO against surface deactivation. These results highlight excellent long-term stability and tolerance against methanol crossover.

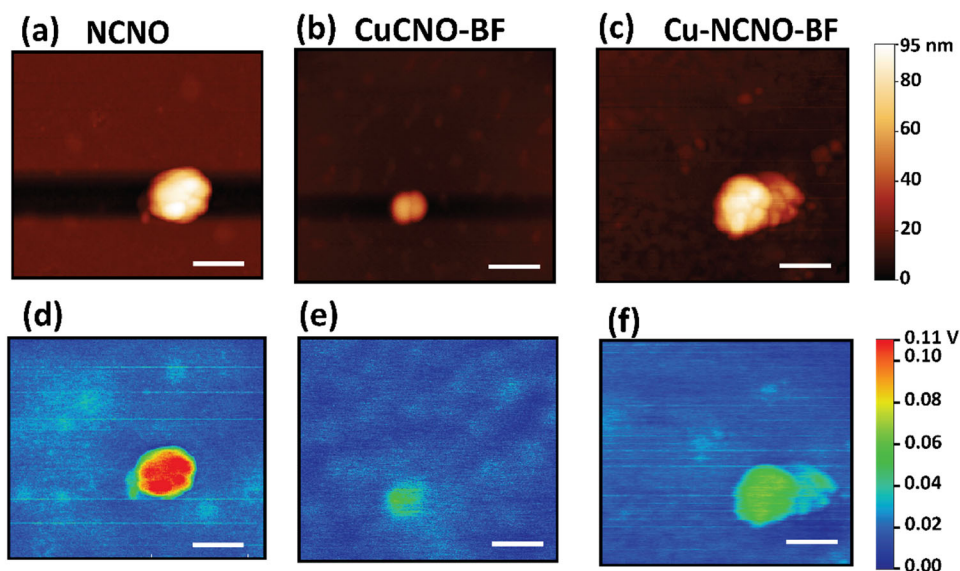


Figure 3.6 AM-KPFM images of individual doped CNO clumps. (a-c) Topography images showing the height of each catalyst, NCNO, Cu-CNO and Cu-NCNO, respectively. (d-f) Contact potential difference images of the doped CNO clumps. The inset scale bars in images (a-c, d)

KPFM measures contact potential difference (CPD) between a sample surface and a conducting cantilever tip. The CPD is directly related to the difference between the work functions of the sample surface and the tip.¹²³⁻¹²⁵ KPFM mapping provides spatially resolved images local work function simultaneously taken with topographic image.¹²⁶ In Figure 3.6, contact potential difference of NCNO, Cu-NCNO, and Cu-CNO as 58.5 ± 18.4 , 57.4 ± 10.5 , and 43.8 ± 2 mV, respectively. The CPD of NCNO has shown

significant variations which may be associated with the inhomogeneity of charge distribution.

3.4 Conclusion

In this work, we were able to synthesize Cu-NCNO by using NCNO followed by post-loading methods such as impregnation and deposition of copper deposit. Nitrogen contributes as a catalytic site for ORR performance and as a nucleation site for copper deposition. In this study, XPS illustrates that the pyridinic and pyrrolic nitrogen configurations, which relate to a significant impact on this ORR activity and copper deposition. Consequently, a modulating nitrogen configuration can improve copper loading to stimulate catalytic activity. The oxygen reduction on the Cu-NCNO catalyst undergoes four electron transfer paths to form water as a byproduct. Additionally, Cu-NCNO has better stability and tolerance to methanol than Pt/C. This work highlights the great capabilities of using the surface potential in Kelvin method. But the V_{CPD} can vary with respect to the surface charge distribution and particle size. Therefore, this study is not sufficient to conclude the work function of each catalyst. should be further continued to find the correlation between the particle size of metal nanoparticles and the work function of each catalyst.

3.5 Supporting information

3.5.1 XRD analysis

The FWHM and 2θ angles of Cu (111) peak were used in Scherrer's equation (Equation 3.4) to determine average crystallite diameter.

$$D = \frac{\kappa\lambda}{\beta\cos\theta} \quad \text{Equation 3.2}$$

Where D is the crystallite dimension, λ is the XRD wavelength, θ is the scattering angle (in radians), β is the FWHM (in radians of theta), and κ is a Scherrer constant (0.94). It can be seen from Figure S3.7 that crystallite size of Cu in Cu-CNO is ~ 17.53 nm based on Cu (111) peak.¹²⁷

3.5.2 Raman analysis

Typically, the Raman spectra of carbon materials show three main bands: D, G, and 2D. The D band at ~ 1350 cm^{-1} is originated with the degree of disorder due to impurities, edges, and defects, etc. The G band at ~ 1500 cm^{-1} indicates the presence of the graphitic layers, therefore the band is associated with the first order scattering of the E_{2g} mode of sp^2 carbon.¹⁰⁵ The D and G band intensity ratios (I_D/I_G) for CNO, NCNO, Cu-NCNO-BF, and Cu-NCNO-AF were 1.02, 1.60, 1.63, and 1.59, respectively. These results indicate that the defect density of CNO was significantly increased after doping nitrogen and that the defect in Cu-NCNO materials do not decrease in comparison with the NCNO sample.

3.5.3 Kelvin probe force microscopy measurements

KPFM measures the electrostatic surface potential of a sample at the micro- to nanoscale. KPFM system is very similar to the general AFM system. The electrostatic surface potential is measured by detecting the electrostatic force imparted on a conducting cantilever tip which is mostly caused by the differences in the work function between a tip and the sample.^{12, 128} In the standard Kelvin method, two plates, namely a vibrating reference electrode on a cantilever beam and a sample, are aligned to create a capacitor (Figure S3.14). Then, a DC bias is applied between them.¹²⁸ By the vibrating reference electrode, an electrical current $i(t)$ is generated with ω the frequency of vibration (equation 3.5).

$$i(t) = V_{CPD} \omega \Delta C \cos \omega t \quad \text{Equation 3.3}$$

where ΔC is vibration of capacitance and V_{CPD} is contact potential difference between two plates. The V_{CPD} is defined as shown in equation 3.6.

$$V_{CPD} = \frac{\phi_1 - \phi_2}{-e} \quad \text{Equation 3.4}$$

where ϕ_1 and ϕ_2 are work functions of the tip and sample, and e is electrical charge of an electron. The V_{CPD} is varied until the current $i(t)$ is minimized.

Table S3.1 Summary of the XPS survey of all catalysts.

| Sample | C (at. %) | O (at. %) | N (at. %) | Cu (at.%) |
|------------|------------|-----------|-----------|------------|
| NCNO (700) | 95.2 ± 0.3 | 0.9 ± 0.3 | 3.9 ± 0.2 | - |
| Cu-NCNO-BF | 93.7 ± 0.4 | 1.7 ± 0.1 | 3.8 ± 0.2 | 1.5 ± 0.2 |
| Cu-NCNO-AF | 94.7 ± 0.1 | 1.7 ± 0.3 | 3.5 ± 0.3 | 0.1 ± 0.1 |
| Cu-CNO-BF | 98.5 ± 0.1 | 1.4 ± 0.1 | - | 0.1 ± 0.1 |
| Cu-CNO-AF | 98.9 ± 0.1 | 1.1 ± 0.1 | - | 0.02 ± 0.1 |

Table S3.2 Summary of the XPS high resolution spectra % Area of N 1s and Cu 2p for NCNO (700), Cu-NCNO-BF, and Cu-NCNO-AF.

| Sample | Pyri N* | Cu-N* | Pyrr N* | Grap N* | N-O* | Cu ⁰ * | Cu ⁺¹ * | Cu ⁺² * |
|------------|---------|-------|---------|---------|------|-------------------|--------------------|--------------------|
| NCNO | 50 | - | 25 | 16 | 9 | - | - | - |
| Cu-NCNO-BF | 49 | 4 | 22 | 16 | 8 | 44 | 31 | 25 |
| Cu-NCNO-AF | 47 | 2 | 22 | 16 | 9 | - | - | - |

*% area for each nitrogen configuration and copper oxidation state, Pyri N = pyridinic nitrogen, Pyrr N = pyrrolic nitrogen, Grap N = graphitic nitrogen.

The element composition and configurations were consistent in NCNO before and after acid washing.

Table S3.3 ORR parameters for recently reported Cu based nitrogen doped graphene-based catalysts in alkaline electrolyte.

| Catalyst | Electrolyte | Limiting current density (mA/cm ²) | Onset potential (V vs. RHE) | Tafel slope (mV dec ⁻¹) | Ref. |
|---------------------------|-------------|--|-----------------------------|-------------------------------------|-----------|
| Cu-NCNO | 0.1 M KOH | 6.5 | 0.83 | 40.0 | This work |
| Cu-N-C ^a | 0.1 M KOH | 5.6 | 0.87 | 37.0 | 129 |
| Cu SAC ^b | 0.1 M KOH | 7.0 | 0.84 | 48.0 | 105 |
| Cu SAC ^c | 0.1 M KOH | 5.6 | 0.97 | - | 130 |
| Cu-NC ^d | 0.1 M KOH | 3.9 | 0.89 | 72.5 | 131 |
| 2 wt% Cu-N-C ^e | 0.1 M KOH | 5.3 | 0.92 | 37.0 | 132 |

Note: support material of each catalyst; (a) ultrathin nitrogenated 2D carbon matrix, (b) graphene oxide (c) nitrogen doped carbon nanotube, (d) nitrogen doped carbon support, (e) 2,6-diaminopyridine (DAP) and silica, (f) ZIF-8.

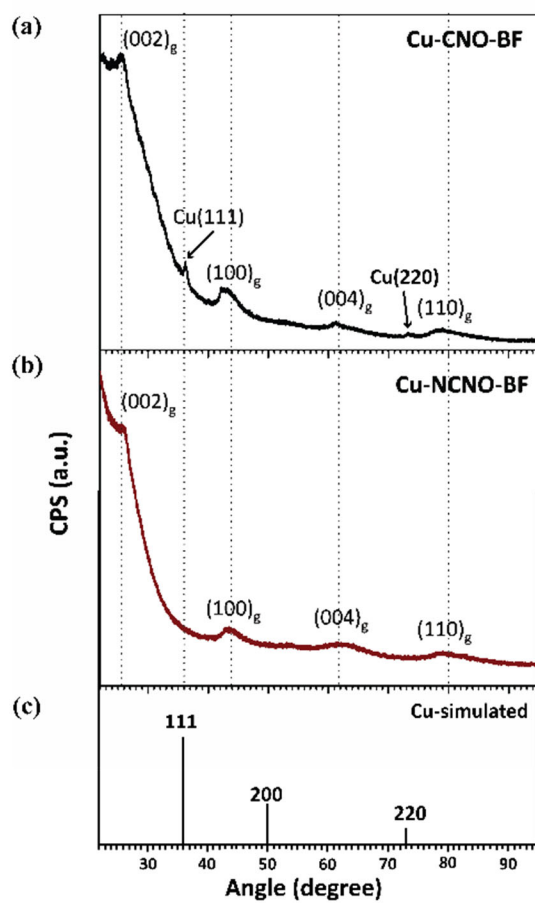


Figure S3.1 XRD patterns for (a) Cu-CNO-BF, (b) Cu-NCNO-BF, (c) Cu reference peaks.¹³³

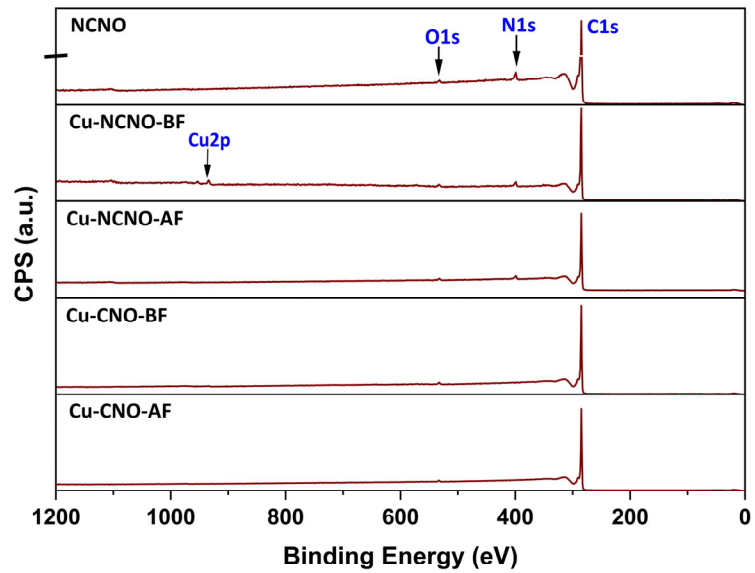


Figure S3.2 XPS survey scans.

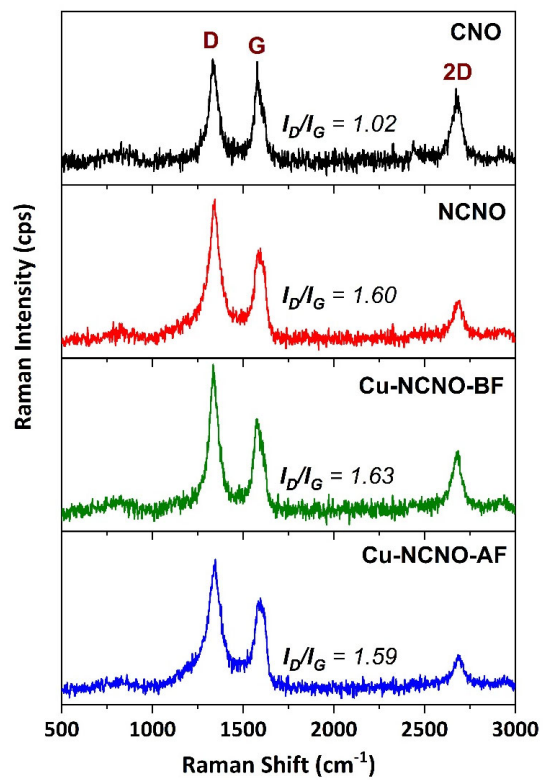


Figure S3.3 Raman Spectra of CNO, NCNO, Cu-NCNO-BF, and Cu-NCNO-AF.

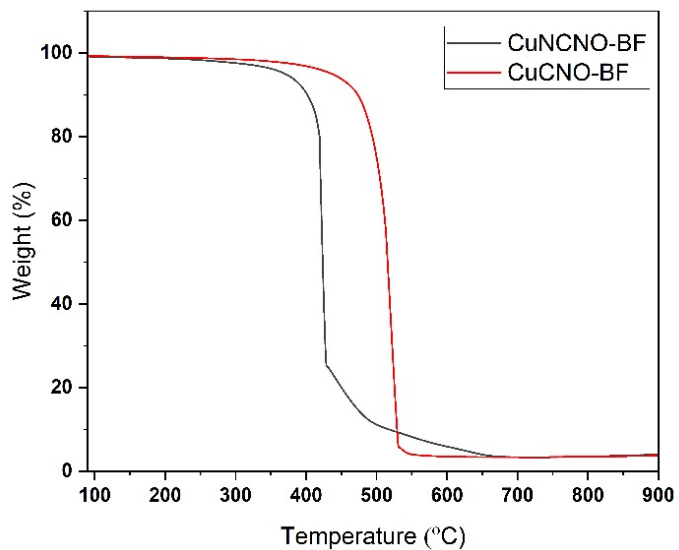


Figure S3.4 TGA of Cu-NCNO and Cu-CNO before acid washing.

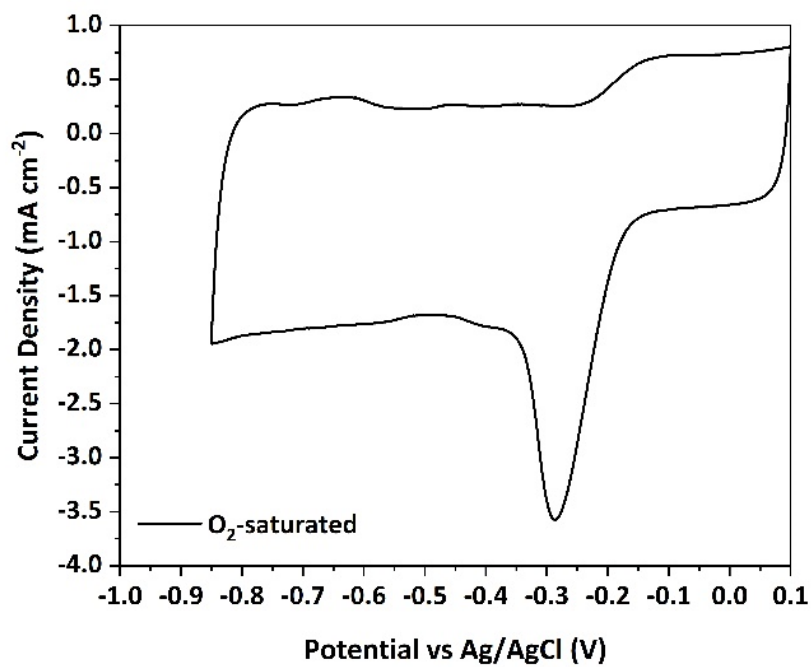


Figure S3.5 CV curve of NCNO in O₂-saturated 0.1 M KOH.

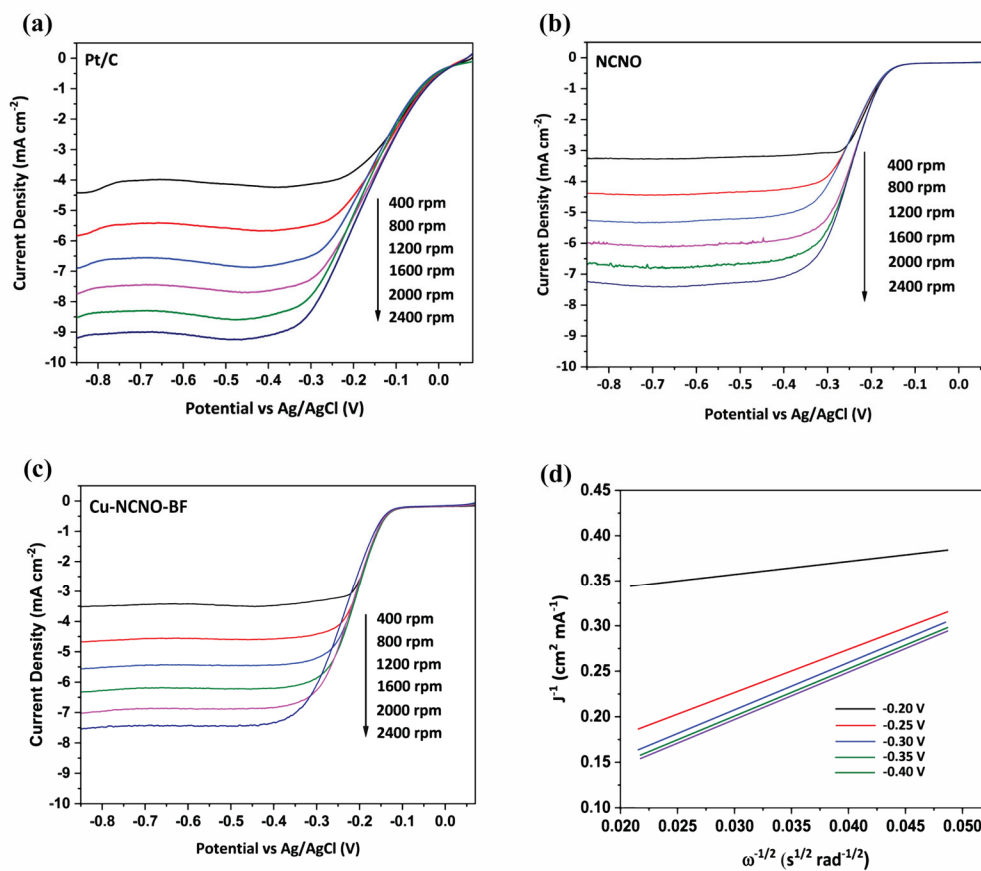


Figure S3.6 LSV curves (a) Pt/C, (b) NCNO, and (c) Cu-NCNO-BF catalyst obtained at different rotating rates (scan rate = 5 mV/s). (d) K-L plots of current density reciprocal (J^{-1}) versus $\omega^{-1/2}$ at different potentials on Cu-NCNO-BF electrode.

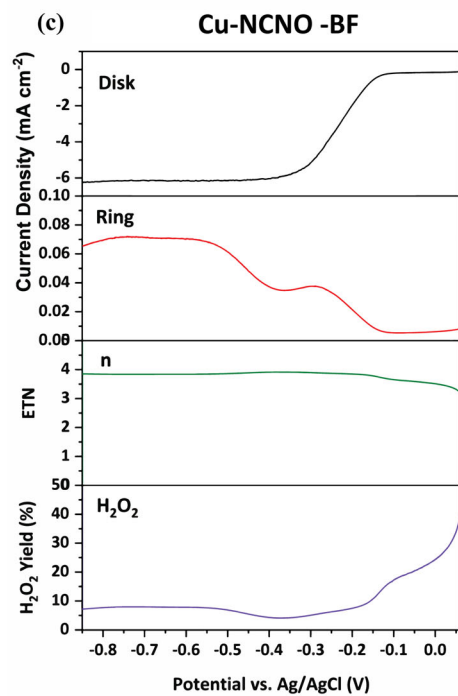
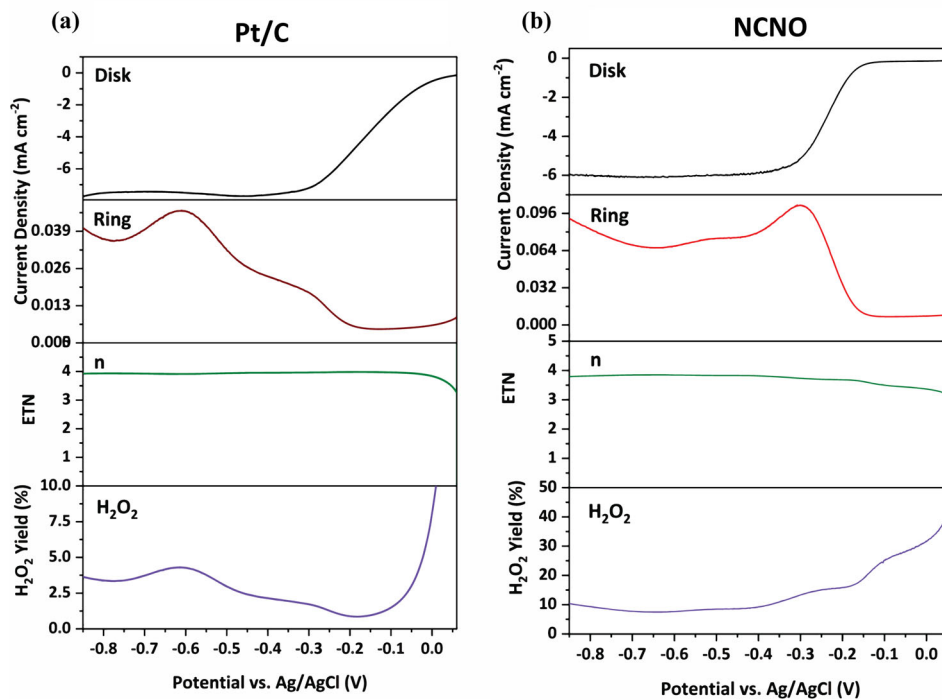


Figure S3.7 RRDE (a) Pt/C, (b) NCNO, and (c) Cu-NCNO catalyst obtained at 1600 rpm rotating rate (scan rate = 5 mV/s).

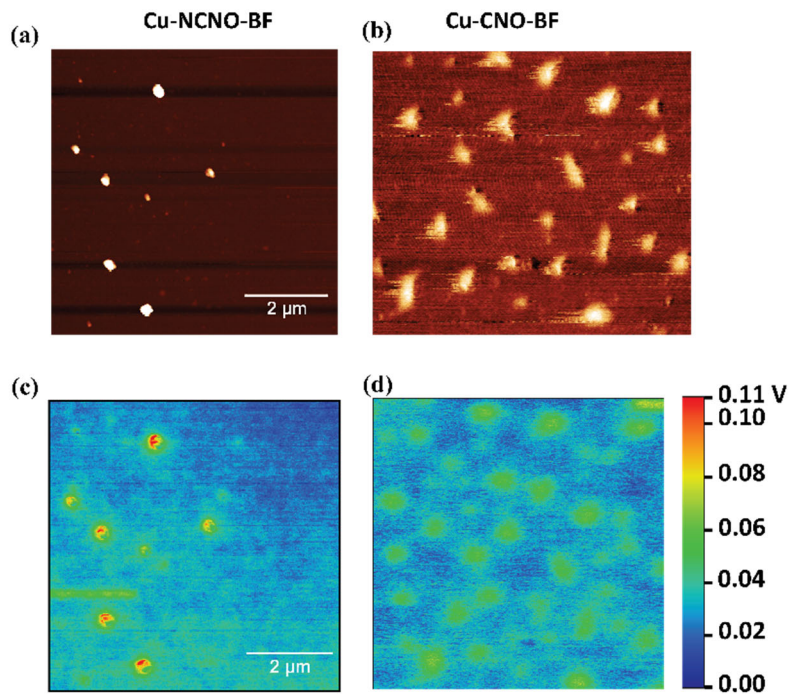


Figure S3.8 AM-KPFM images of Cu-NCNO-BF and Cu-CNO-BF clumps. (a,b) Topography images showing the height of each catalyst, Cu-CNO and Cu-NCNO, respectively. (c,d) Contact potential difference images of the doped CNO clumps.

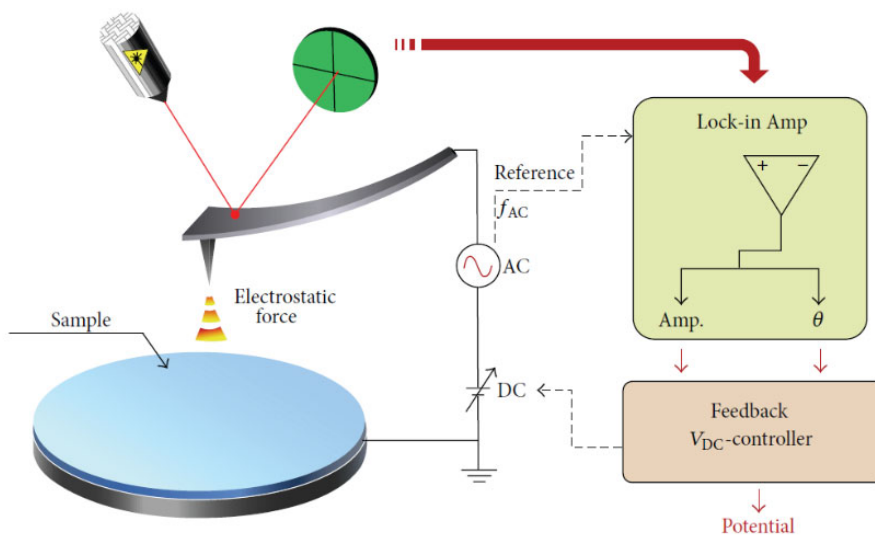


Figure S3.9 Block diagram of general KPFM system.

CHAPTER 4. COPPER-CATALYZED ELECTROCHEMICAL CONVERSION OF BICARBONATE FEEDSTOCK TO ACETATE AND FORMATE IN A FLOW-TYPE ELECTROLYZER

4.1 Introduction

Electrocatalytic conversion of emitted CO₂ into valuable chemicals and fuels powered by renewable energy offers a promising route towards reducing carbon emission, storing renewable energy, and leveraging our existing infrastructure.⁴³ Substantial research efforts have been devoted for the development of heterogeneous catalysts and electrolyzers for efficient carbon dioxide reduction reaction (CO₂RR). Heterogeneous catalysts are a critical component in CO₂RR, providing active sites for efficient adsorption and structural transformation of CO₂ into C1 products such as carbon monoxide (CO), methane (CH₄) and formate (HCOO⁻).^{134, 135} Further reduction of C1 products into C₂+ hydrocarbons and oxygenates such as ethylene, ethanol, and acetate is generally challenging, due to low concentration of adsorbed CO₂, short lifetime of adsorbed intermediate species, and sluggish kinetics of carbon-carbon (C-C) coupling.¹³⁶ To overcome this limitation, several parameters need to be controlled such as catalysts, local pH, electrolyzer etc.^{137, 138} At present, copper (Cu) is considered as the most promising catalyst to promote C-C coupling to produce C₂+ chemicals.¹³⁸⁻¹⁴⁰

Most of the pilot-scale CO₂RR electrolyzers use gaseous CO₂ as a feedstock.¹⁴¹ One approach is to purge CO₂ gas into electrolyte. This approach is generally limited by low reduction current due to low solubility of CO₂ in aqueous electrolyte.¹⁴² The second approach is to adopt a gas-diffusion-electrode (GDE) in the electrolyzer. In this configuration, compressed CO₂ gas diffuses through a gas-compartment and a porous GDE to reach a three-phase boundary where CO₂RR takes place. Despite the advantage

of high reduction currents, the approach of using gaseous CO₂ (typically compressed) as a feedstock is economically incompetent because the release and pressurization of CO₂ gas are energetically uphill processes.¹⁴³ The enthalpy (ΔH) of 178.3 kJ mol⁻¹ is required to release CO₂ gas from upstream CO₂ captured solution. Both release and pressurization requires highly endothermic calcination step.¹⁴⁴

To address this issue, the current study demonstrates the feasibility of utilizing bicarbonate (HCO₃⁻) as a feedstock. This bicarbonate solution can be transported from an upstream carbon capture process and directly fed into an electrolyzer. At present, only a few studies have been reported with HCO₃⁻/CO₃²⁻ solution as a feedstock. Dunwell et al. demonstrated that bicarbonate is at a rapid equilibrium with dissolved CO₂ and supplied CO₂. In the process of bicarbonate electrolysis, bicarbonate serves as an electrolyte, a proton donor, and improves CO₂RR rates by increasing the reducible CO₂ in the solution.¹⁴⁵ Silver is one of popular catalysts for bicarbonate reduction and it commonly generates CO.^{141, 143, 146, 147} Silver nanoparticles supported on carbon produced CO with the FE of ~80 % at current densities (J) of 25 mAcm⁻².¹⁴⁷ Zhang et al. reported the bicarbonate conversion into CO by silver catalyst with the FE of 15% for CO production at current density of 500 mA cm⁻² at -2.2 V.¹⁴⁶ A few studies have been conducted on the conversion of bicarbonate with tin (Sn) and bismuth (Bi) catalysts where the formation of formate is dominant.^{143, 148} Tengfei et al. reported that converting bicarbonate to formate on bismuth nanocrystals with FE of 62% at 100 mAcm⁻².¹⁴³ The FE towards formic acid formation when Sn as the catalyst was 47% in 1.5 M KHCO₃ with the saturated CO₂.¹⁴⁸

This work reports the conversion of bicarbonate using copper catalyst supported on carbon paper. Bicarbonate was converted to C1-C2 products using copper electrocatalyst. Bicarbonate electrolysis produced acetate and formate with the total CO₂RR faradaic efficiency (FE) of 38 % and H₂ with the FE of 27 %. The FE's of acetate formation and formate formation at -2 V are 32 % and 6 %, respectively. Anodic catalyst, Pt/C, was for the production of protons via hydrogen oxidation reaction (HOR). The protons were transported to catholyte through cation exchange membrane (CEM). In the cathode, bicarbonate becomes protonated to CO₂(g) which undergoes CO₂RR.

4.2 Results and discussion

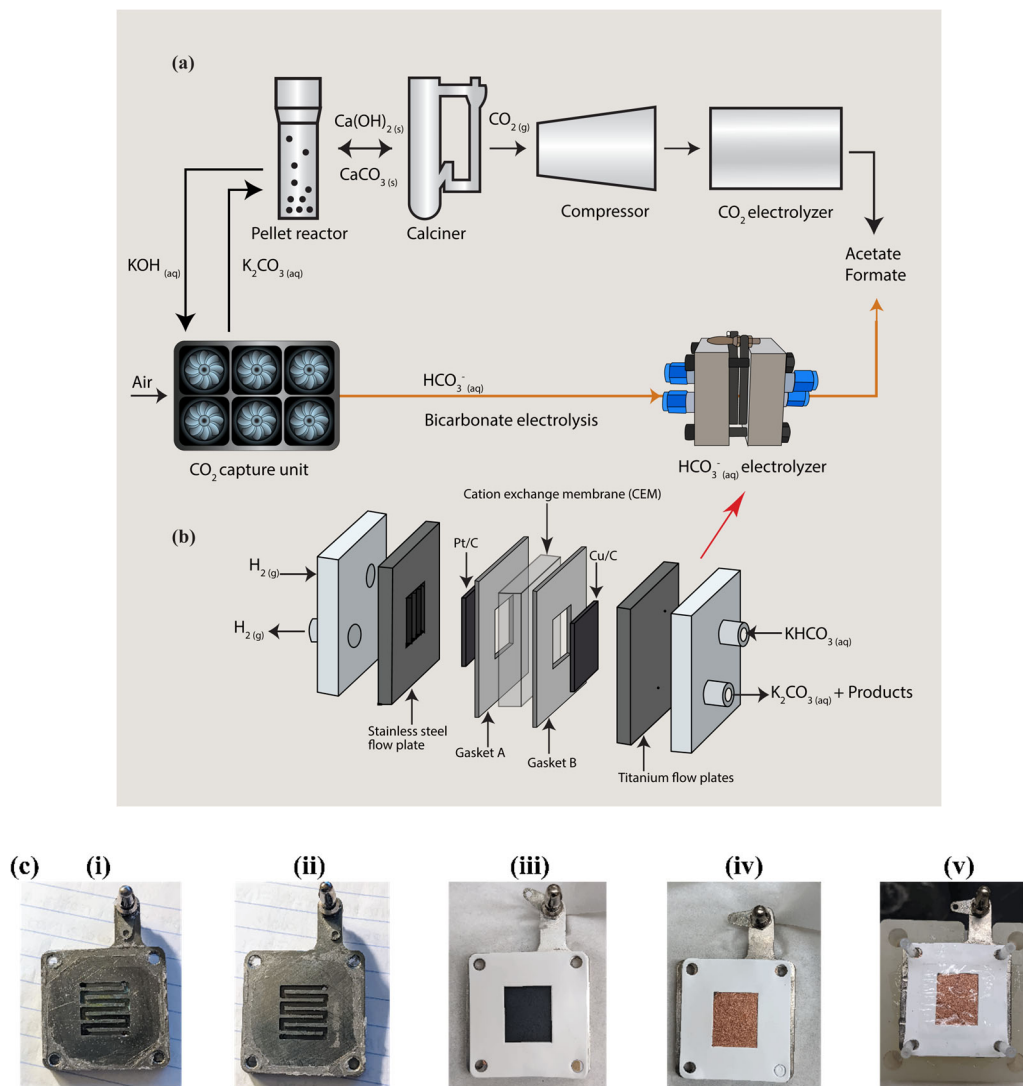


Figure 4.1 (a) A flow diagram that shows parallel pathways of (i) CO₂ electrolysis following CO₂ capture and (ii) bicarbonate electrolysis. (b) the expanded view of a bicarbonate electrolyzer. Expanded flow design for the bicarbonate conversion into products. (c) the photographs of (i) titanium flow field (cathode), (ii) stainless-steel flow field (anode), (iii) Pt/C anode, (iv) Cu cathode, (v) cation exchange membrane (CEM).

In alkaline CO₂ capture process, caustic soda (NaOH) is used as a CO₂ captured materials which offers rapid absorption, producing aqueous (bi)carbonate solutions.¹⁴⁹ The release of CO₂ from the captured solution and pressurization require a lot of energy because of highly endothermic calcination reaction (Figure 4.1a).⁴³ Therefore, it is highly desirable to use the concentrated bicarbonate solution directly as the feedstock in the electrolyzer as shown in Figure 4.1(b). The components of our electrolyzer are shown in Figure 4.1(c). One critical component in the electrolyzer is the MEA which is also known as the “zero gap” electrode.¹⁵⁰ A stainless steel flow plate and a titanium flow plate are designed to deliver humidified hydrogen gas to the anode and 1M KHCO₃ to the cathode, respectively.

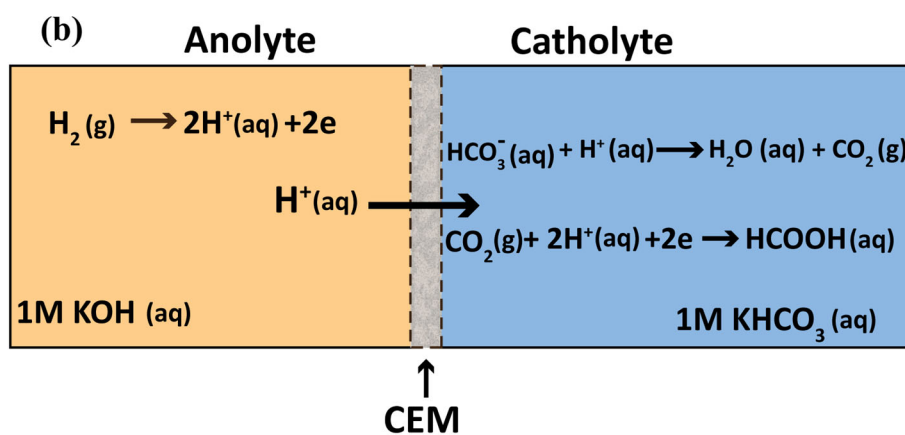
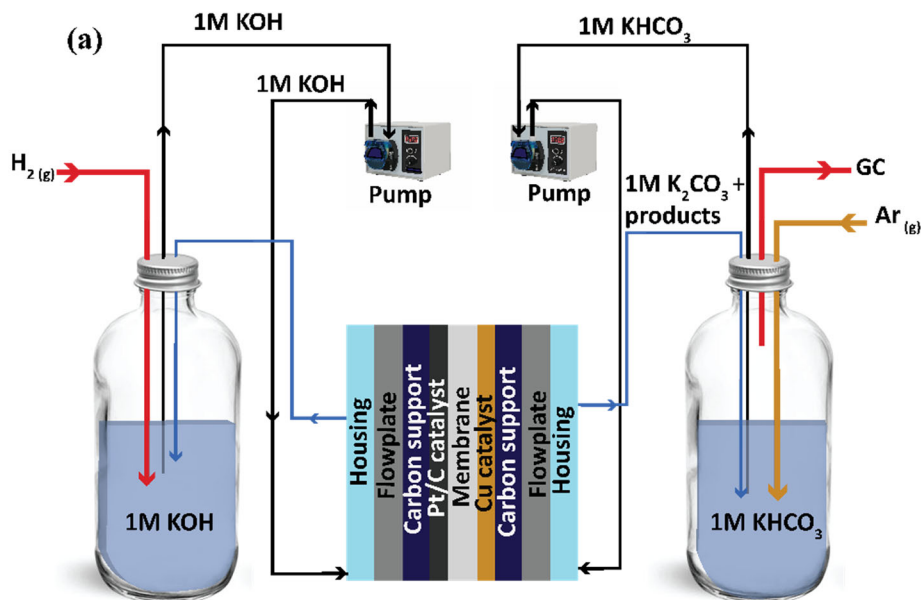
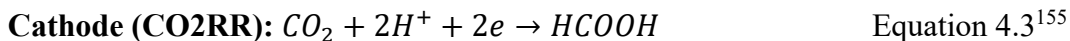
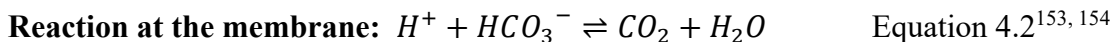


Figure 4.2 (a) A schematic of the bicarbonate electrolyzer, peristaltic pump, and the flow of the reactants and products. The peristaltic pump delivers both 1M KHCO₃ and 1M KOH at 15 sccm through the cathode flow plate to Cu catalyst and anode flow plate to the anode catalyst, respectively. (b) Diagrammatic representation of the electrolysis process in the electrolyzer. The experimental set up and the workstation have shown in Figure S4.1.

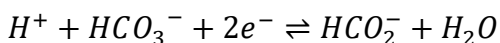
Figure 4.2a is a schematic representation of the electrolyzer. For bicarbonate conversion, 1 M KHCO₃ (pH 8.3) and 1 M KOH (pH 14) served as catholyte and anolyte,

respectively. Both electrolytes are circulated by peristaltic pumps. Pt/C ink was air-brushed on carbon paper support for anode. A thin copper layer (~300 nm) was sputtered on a carbon paper for cathode. After the coating of copper, Nafion ionomer was air-sprayed to provide a hydrophobicity and to enhance the mechanical integrity of the copper layer.¹⁵¹ Figure 4.2(b) illustrates electrochemical reactions occurring in a two-compartment cell. The anodic and cathodic reactions are shown in equations 4.1 – 4.3. During electrolysis, hydrogen oxidation reaction (HOR) occurs at the anode. This anode reaction provides protons (H^+) which diffuse through CEM to the cathode side. At the cathode, bicarbonate combines with H^+ to generate CO_2 , then CO_2RR takes place to generate gaseous and liquid. Equation 4.3 shows concerted proton transfer and electron transfer to produce formic acid.



The main idea of this work is performing the experiment in non- CO_2 saturated bicarbonate solution which will practically contain low concentration of CO_2 . Typically, the bicarbonate solution acts as an electrolyte which favors CO_2 dissolution and enhances the conductivity of the aqueous solution. However, aqueous bicarbonate is always in equilibrium with dissolved CO_2 .¹⁴⁸ Therefore, it is controversial whether the source of cathodic reaction is bicarbonate or CO_2 . One potential mechanism for the direct

conversion of bicarbonate to formate is shown in equation 4.4. Indirect conversion of bicarbonate to formate through CO₂ (g) is also possible (equation 4.3).



Equation 4.4¹⁴⁸

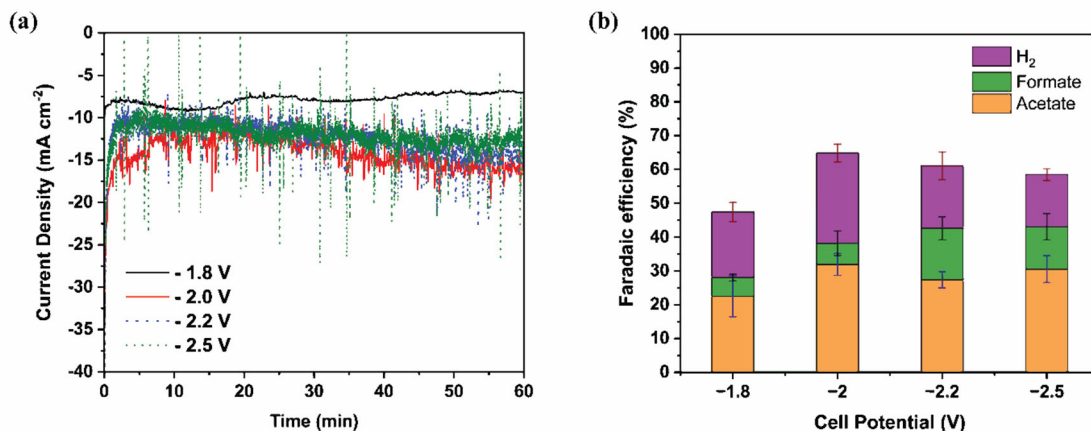


Figure 4.3 (a) Chronoamperometric curves recorded at fixed potentials under the flow of Ar in 1 M KHCO₃, (b) The FE's of H₂, formate, and acetate determined from GC and NMR analysis.

Electrochemical performance of copper cathode for bicarbonate reduction was examined by constant-potential electrolysis (chronoamperometry). The potentials of -1.8 V, -2 V, -2.2 V, and -2.5 V were chosen based on linear sweep potentiometric measurements (Figure S4.5). Figure 4.3(a) is the overlaid chronoamperometric curves of reduction current vs time recorded at the fixed potential. In the Cottrell plot of J vs. 1/t^{1/2}, the current was not strictly constant for 60 min.¹⁵⁶ After the initial decay of current for the first a few minutes, the current was gradually increased due to surface activation. During the electrolysis, bubble formation was observed. Some of the bubbles remained

on the working electrode, blocking the active sites. The noisy chronoamperometric curves are due to the bubble formation. The FE's of gaseous products and liquid products were determined by NMR and GC, respectively. These products were quantified using the equations given in the supporting information. Figure 4.3(b) summarizes the FE's of acetate, formate, and H₂ determined at different potentials. At -2 V, the FEs of acetate and formate are 32 % and 6 %, respectively.

According to the product analysis by using NMR and GC, acetate and formic acid were observed as liquid products and hydrogen as the only gaseous product. These products were quantified using their respective equations given in the supporting information. Figure 4.3(b) depicts the FE of 31% and 6% for acetate and formate, respectively. Both product formation increases when the potential is negatively shifted from -1.8 V to -2.5 V.

Bicarbonate reduction pathway is highly dependent on local pH.¹⁵⁷ At neutral pH, C1 and C2 products formation channels could share common intermediates. Products are formed via proton transfer and electron transfer. CO₂(g) from the protonation of bicarbonate is adsorbed on Cu surface and reduced to $CO_2^{\bullet -}$ radical ion. Bicarbonate ion serves as a proton donor due to its lower pKa value than H₂O (pKa of H₂O = 14, pKa of HCO₃⁻ = 10.3).¹⁴³ According to the results, higher FE of acetate production than that of formate is due to the rapid C-C coupling. A possible mechanism for bicarbonate conversion to acetate and formate is shown in Figure 4.4. In-situ Raman or infrared absorption spectroscopy may track intermediates formed during bicarbonate electrolysis. We also performed bicarbonate reduction with 0.1 M H₂SO₄ (anolyte) instead of 1 M KOH. In this experiment, the maximum current density of -5.2 mA cm² was acquired at -

3.2 V with H₂ as a predominant product. The FEs of H₂ and CO₂RR are 70 % and 2 %, respectively. It confirms that when high concentration of protons come to the cathode, it promotes HER and suppresses CO₂RR.

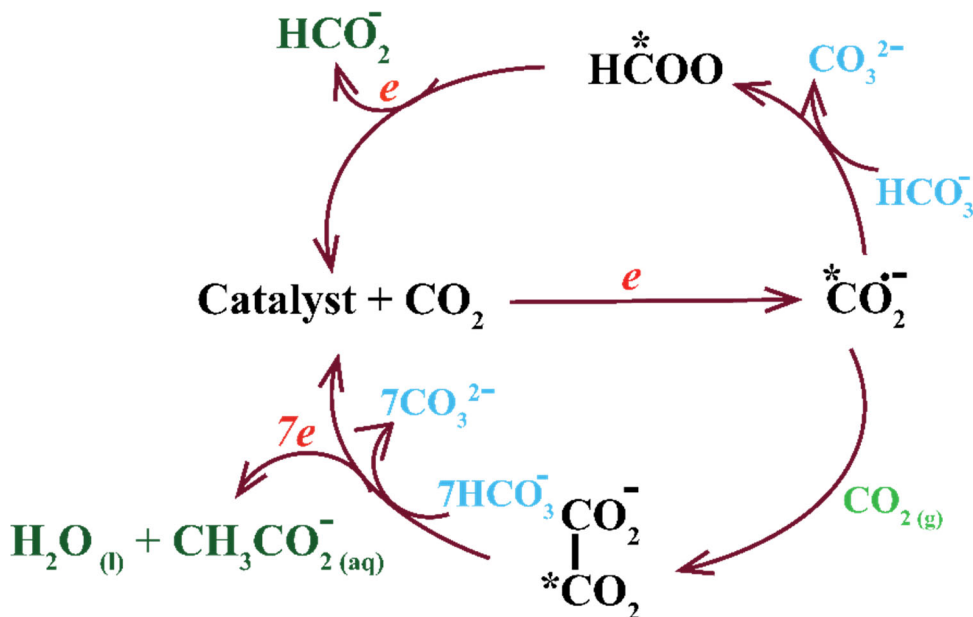


Figure 4.4 Possible mechanism to form acetic acid and formate during the bicarbonate electrolysis.

Based on the liquid and gas products, the possible mechanism for the bicarbonate conversion has been shown in Figure 4.3. The given pathway illustrates after the bicarbonate conversion into CO₂, transformation into products through electrocatalytic steps. Initially, HCO₃⁻ ions from the electrolyte capture protons diffused from the anode. Then, CO₂ forms at the cation exchange membrane and the catalyst interface. As shown in the figure, the first step is adsorption of CO₂ on to the Cu electrode surface and reduced to radical ion. In here, it is believed that these intermediates resided long

lifetime on the copper surface, consequently carbon-carbon bond formation takes place form acetate.

In Table 4.1, the performance of Cu/C is compared with other electrocatalysts reported in literature for CO₂ and bicarbonate reduction. Among those, Cu/C electrocatalyst has shown competitive current density and high selectivity for acetate formation.

Table 4.1 Comparison of previous reports and current study on the conversion of bicarbonate/CO₂ to acetate and formate.

| Catalyst | Membrane | Electrolyte | Feedstock | Potential vs. RHE (V) | Current density (mA cm ⁻²) | Faradaic efficiency (%) | | Ref. |
|-----------|-----------|------------------------------|-----------------------|-----------------------|--|-------------------------|---------|------------------|
| | | | | | | Acetate | Formate | |
| NDD/Si RA | Not given | 0.5 M NaHCO ₃ | CO ₂ sat'd | -1.30 | ~6.5 mA | 77.6 | 14.6 | 158 |
| Bi/C | BPM | 3M KHCO ₃ | CO ₂ sat'd | -4.00 ^a | -100 | NF | 62 | 143 |
| Pd/C | AEM | 0.5M NaHCO ₃ | CO ₂ sat'd | 0.35 | -6.5 | NF | 88 | 159 |
| Mn-Cor-CP | Not given | 0.1M phosphate buffer (pH=6) | CO ₂ sat'd | -1.25 vs. Ag/AgCl | -0.8 | 63 | NF | 160 |
| Fe/N-C | Not given | 0.05M KHCO ₃ | CO ₂ sat'd | -0.5 vs. Ag/AgCl | -0.36 | 60.9 | 36.5 | 161 |
| Cu/C | CEM | 1M KHCO ₃ | KHCO ₃ | -2.00 ^a | -14.4 | 31.9 | 6.3 | This work |

Note: ^acell potential, N-doped nanodiamond/Si rod array (NDD/Si RA), bipolar membrane (BPM), anion exchange membrane (AEM), cation exchange membrane (CEM), not found (NF).

4.3 Conclusion

This work demonstrates copper-catalyzed bicarbonate reduction. Bicarbonate was converted to acetate and formate with the total CO₂RR faradaic efficiency (FE) of 38 %. The FE's of acetate formation and formate formation at -2 V are 32 % and 6 %, respectively. Anodic catalyst, Pt/C, was to produce protons via hydrogen oxidation reaction (HOR). The protons were transported to catholyte through cation exchange membrane (CEM). Further studies are needed to track intermediate species and to increase the reduction current.

4.4 Supporting information

4.4.1 Experimental methods

4.4.1.1 Preparation of Cu catalyst

Cathodic catalyst material, copper (Cu ~300 nm thick) was deposited onto gas diffusion layers (GDL) (Freudenberg H23, FuelCell store) by a sputter coater (ATC-Orion 5 UHV sputtering system) using 99.995% pure Cu target. The sputtering rate was maintained at 5 nm min⁻¹ with a base pressure of 7.7 x 10⁻⁸ torr. The copper coated GDL was cut into 2.0 cm x 2.0 cm pieces. Then an ionomer solution was prepared by adding 94.5 μL of Nafion (5 wt %, D520 NafionTM dispersion, FuelCell store) to 3 mL of methanol (99.8%, anhydrous, Sigma Aldrich). Finally, the ionomer solution was airbrushed onto 1.5 x 1.7 cm² area of the sputtered Cu layer until the desired ionomer loading was achieved (~0.5 mgcm⁻²). The final loading of ionomer on the Cu-coated GDL was slightly varied in each airbrushed step and was determined from the electrode

mass before and after the airbrushing. Samples were dried for at least 24 h at room temperature in a vacuum chamber before operation.

4.4.1.2 Preparation of Pt/C anode electrode

To prepare Pt/C ink, 4 mg of Pt/C was added into a mixture of methanol (2 mL) and distilled water (1 mL) with 40 μL of Nafion. Then, the mixture was sonicated for 20 min to make a homogenous mixture. Finally, the ink was air-brushed onto a porous carbon support (Sigracet 39BB) until the required loading ($\sim 0.5 \text{ mg cm}^{-2}$) was achieved.

4.4.1.3 Flow cell setup

The flow cell has been integrated and consists of the housing, gaskets, anode, and cathode flow field plates, as well as a membrane electrode (MEA; Figure S4.1b, c). The anode and cathode housing were made of polypropylene for delivering the aqueous feedstock to the anode and cathode. The titanium cathode flow plate and the stainless-steel anode flow plate sandwiched the 2.55 cm^2 MEA. The anode (316 stainless steel) and cathode (grade 2 titanium) flow-field plates (active area = 2.55 cm^2) consisted of serpentine channels 1.5 mm wide and 1.5 mm deep with 1 mm ribs. The MEA is coated with Cu/ ionomer as the cathode (1.5 x 1.7 cm), a cation exchange membrane (CEM, 2.5 x 2.5 cm), and Pt/C anode electrode (1.5 x 1.7 cm). A PTFE layer with a window of 2.5 x 1.7 cm was sandwiched between the CEM and the Cu cathode to mask the inactive area of Cu. Then, the entire set-up was sandwiched between the two polypropylene housings screwed in with 4 bolts. The cathodic electrolyte (catholyte) was 50 ml of 1M KHCO_3 solution and the anode electrolyte (anolyte) was 50 ml of 1M KOH. The headspace of the

catholyte was purged with Ar (g) or CO₂ (g) at 20 sccm while the headspace of the anolyte flask was purged H₂ at 20 sccm. The cathode electrolyte (catholyte) was 50 ml of 1M KHCO₃ solution and the anode electrolyte (anolyte) was 50 ml of 1M KOH. The outlets of the cathode and anode compartments were directed separately to each sealed vial for recycling. Electrolyte was used in every set of experiments. Also, the headspace of the catholyte flask was connected to the gas sampling bag to collect gas products for the gas chromatography analysis.

4.4.1.4 Electrochemical test and electrolysis

The electrochemical experiments were conducted with a CHI 660D potentiostat. Linear sweep voltammograms (LSV) were collected under Ar at a scan rate of 20 mVs⁻¹ prior to the chronoamperometry measurements. Based on the LSV, the potentials were selected, and all electrolysis were performed by applying a constant potential (chronoamperometry) as -1.8, -2.0, -2.2, and -2.5 V to the working electrode (WE) in a two-electrode flow cell reactor. The electrolysis time was an hour for each potential and during that time, gas samples were collected every 20 minutes and analyzed by the gas chromatography (GC, SIRI.). After an hour electrolysis, liquid products were quantified by NMR (400 MHz Bruker Avance NEO). Phenol and DMSO were used as the internal standard for liquid product analysis.

4.4.1.5 Product quantification

4.4.1.5.1 NMR analysis for liquid products

After each electrolysis, the liquid electrolyte was collected to analyze and quantify liquid products by using a 400 MHz Bruker Avance NEO spectrometer. NMR samples were prepared by mixing 600 μL electrolyte with 200 μL D_2O , 10 μL GdCl_3 (7mM) (relaxing agent), and internal standards of 10 μL dimethyl sulfoxide (DMSO, 21 mM) and 20 μL phenol (21 mM). The water suppression method was applied to each sample to increase the visibility of other peaks. All spectra were collected by using 128 scans with a 10 second relaxation delay. Formic acid was quantified based on the integrated peak area of phenol while acetate was quantified by using the integrated peak area of DMSO. The correlation between the internal standards and liquid products was depicted in Figure S6 NMR spectra. The equation S1 and S2 were used to calculate the Faradaic efficiency (FE%) for liquid products.¹⁶²

$$\text{Faradaic efficiency} = \frac{e_{\text{output}} \times 100\%}{e_{\text{input}}} \quad \text{Equation S 4.1}$$

$$\text{Faradaic efficiency} = \frac{x (\text{mol}) \times n_e \times F \times 100\%}{I(A) \times t(s)} \quad \text{Equation S 4.2}$$

where,

e_{output} = the number of electrons in moles supplied for the generation of a specific liquid product (mol)

e_{input} = a total number of electrons in moles provided to the electrode during electrolysis (mol)

x = the quantity of a specific liquid product in moles determined by NMR analyses (mol)

n_e = the number of electrons in mol required to obtain 1 mol of formic acid

F = Faraday constant (96485.3329 A s mol⁻¹)

I = The average of chronoamperometric currents recorded during electrolysis (A)

t = Duration of electrolysis (second)

4.4.1.5.2 Gas chromatography for gas sample analysis

The gaseous products were quantified by gas chromatography (GC, SRI 8610C) with two columns (a silica gel HaySep D as column 1 and a Mole-Sieve 13X as column 2), a thermal conductivity detector (TCD), and a flame ionization detector (FID) interfaced to a methanizer. During electrolysis, gas samples were collected to analyze and quantify gaseous products that were collected in a gas bag. Gas samples (1 ml) were immediately injected into the GC. The FID was used for the analyses of CO, CO₂, and CH₄ using N₂ as the carrier gas (flow rate = 20 ml min⁻¹) and supplying H₂ to FID/methanizer at a flow rate of 25 ml min⁻¹. The analyses of H₂ used a TCD detector. The oven temperature was maintained at 40 °C for 10 min and then increased to 200 °C using a ramp of 20 °C min⁻¹. Faradaic efficiency for gas products was calculated by using the Equation S4.3 and S4.4.¹⁶²

$$\text{Faradaic efficiency} = \frac{e_{\text{output}} \times 100\%}{e_{\text{input}}} \quad \text{Equation S 4.3}$$

$$\text{Faradaic efficiency} = \frac{e_{\text{output}} \times 100\%}{e_{\text{input}}} \quad \text{Equation S 4.4}$$

e_{output} = the number of electrons in moles supplied for the generation of a specific liquid product (mol)

e_{input} = a total number of electrons in moles provided to the electrode during electrolysis (mol)

x = the quantity of a specific liquid product in moles determined by NMR analyses (mol)

n_e = the number of electrons in mol required to obtain 1 mol of formic acid

F = Faraday constant (96485.3329 A s mol⁻¹)

R = the flow rate of carbon dioxide carrier gas (sccm)

I = The average of chronoamperometric currents recorded during electrolysis (A)

V = The volume of gas injected into GC (cm³)

4.4.1.6 Material characterization

4.4.1.6.1 Scanning electron microscopy (SEM)

These images were taken on a FEI Helios NanoLab 660 dual beam SEM that utilized a secondary electron with an accelerating voltage from 1kV and a current of 50 pA. The working distance was 4 mm.

4.4.1.6.2 X-ray Diffraction (XRD) analysis

XRD patterns were acquired using a BRUCKER AXS D8 ADVANCE x-ray diffractometer equipped with CuK α radiation (1.54 Å) LYNXEYE (1D mode) detector with a step time of 1 s, and the increment of 0.01°.

4.4.1.6.3 X-ray photoelectron spectroscopy (XPS)

Elemental composition and the chemical states of elements in each sample were analyzed by XPS using a Thermo Scientific K-Alpha (α) photoelectron spectrometer. This measurement was conducted by focusing on monochromatic Al K- α radiation (energy of 1486.6 eV) onto a sample. The focused spot size was 400 μ m. Each sample was exposed to an electron flood gun to reduce surface charging during XPS measurement. This data was analyzed using an Avantage.Ink software. The analyzed samples were labeled as as-prepared Cu film (as-Cu), Cu film/Nafion ionomer (Cu/Nafion), and after the electrolysis (Cu-after electrolysis).

Figure 4.1c shows each part of the electrolyzer. After stacking these parts, silicon was used to seal everything. The schematic illustration of the whole set up is given in the main text Figure 4.2a. In Figure S4.2, SEM images show the morphology of the carbon support.

The structure of catalyst plays a significant role in determining efficiency and selectivity. Therefore, crystal facets exposed to the reaction interface have an impact on product selectivity. Based on DFT calculations conducted on Cu (100) and Cu(111), Garza et al. reported that the energy barriers of CO dimerization on Cu (111) and Cu(100) are low enough to such that C-C coupling occurs at the initial stage of the

CO₂RR.^{163, 164} However, there is insufficient information on bicarbonate electrolysis to understand the mechanism of C-C coupling on various Cu facets. In addition to the catalyst morphology, the CO₂/HCO₃⁻, H₂CO₃/HCO₃⁻, and HCO₃⁻/CO₃²⁻ equilibria in aqueous electrolytes are sensitive to (bulk) pH, buffer capacity, and electrolyte (cations and anions).¹⁶⁵ With that, most studies indicate that CO₂ is an active species as well as bicarbonate is also proposed as an active species, especially to produce formate.^{157, 166, 167} XRD obtained from the electrode before and after electrolysis exhibited clearly crystalline phases of Cu on carbon support (Figure S4.3). Those peaks correspond to Cu (111), Cu (100), and Cu (220). The electrode after the electrolysis did not show any additional peaks related to (bi)carbonate deposition at ~32, ~4, and ~50°.

The basic potentiostate sweep method, linear sweep voltammetry (LSV) in Figure S4.5 was conducted to study the kinetic behavior of the electron transfer process in the bicarbonate electrolyzer. The working electrode potential was swept linearly from -0.6 V to -3.0 V and the current was measured. LSV curves for both before and after electrolysis indicated current decaying at higher potentials. This effect could be due to the mass transport limitation at higher potentials. Also, there was a slight reduction current peak at around -1.2 V. Note that in the presence of air copper can be oxidized to form layers of Cu₂O, CuO or Cu(OH)₂.¹⁶⁸ The availability of these oxide configurations further confirmed XPS analysis in Figure S4.4. During the electrolysis copper reduction can act as another Faradaic reaction, thereby the total Faradaic efficiencies in Figure 4.3b is lower than that of 100%.

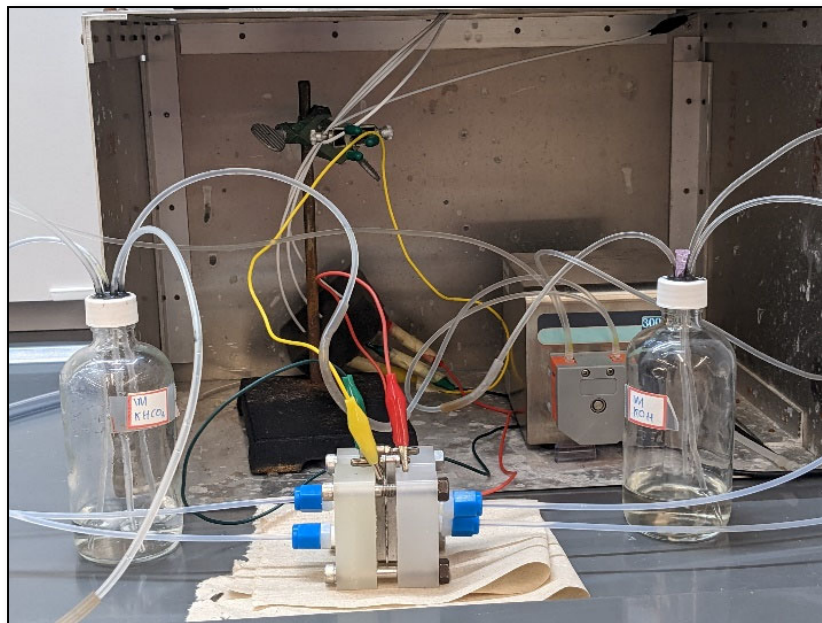


Figure S4.1 Experimental setup in the electrochemical workstation.

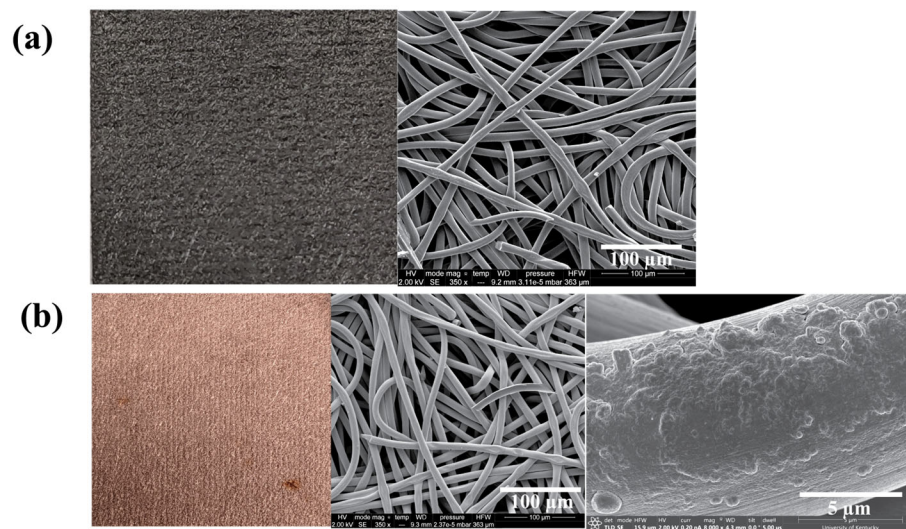


Figure S4.2 SEM images (a) carbon support (b) after Cu deposition on the carbon support.

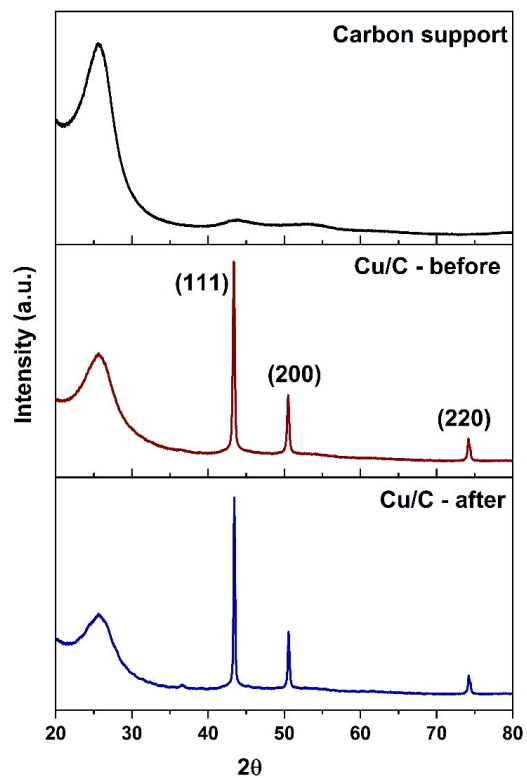


Figure S4.3 X-ray diffractograms of Cu/C electrocatalyst and the carbon support (control).

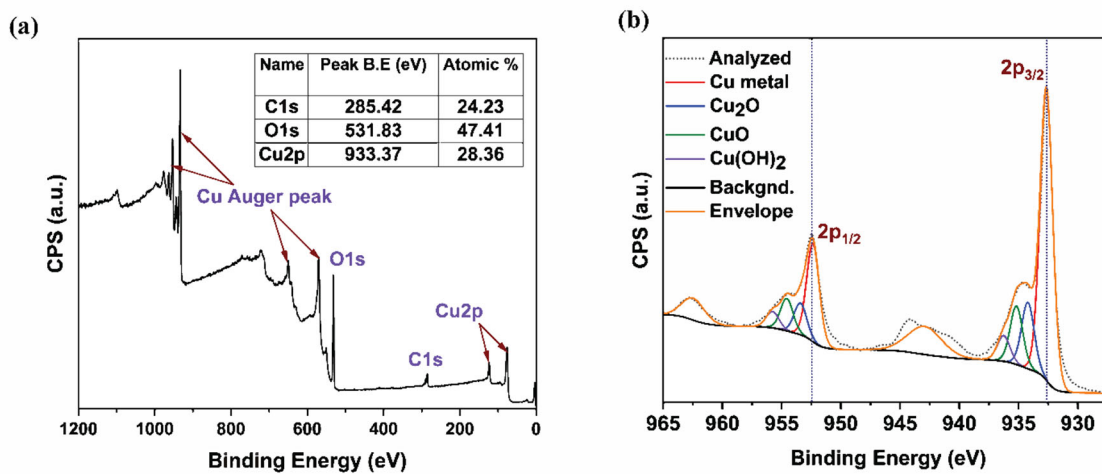


Figure S4.4 (a) XPS survey spectrum of Cu/C (b) high resolution Cu 2p spectrum.

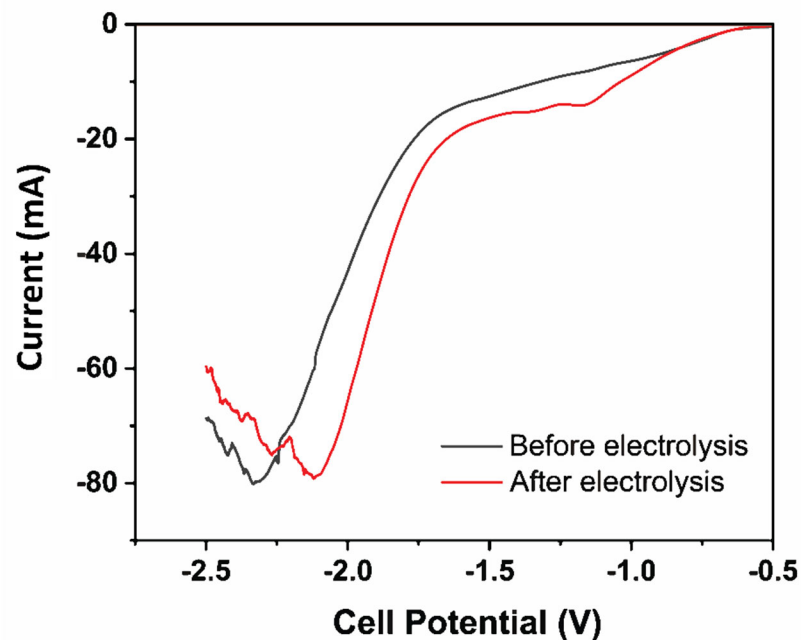


Figure S4.5 LSVs for Cu/C before and after electrolysis.

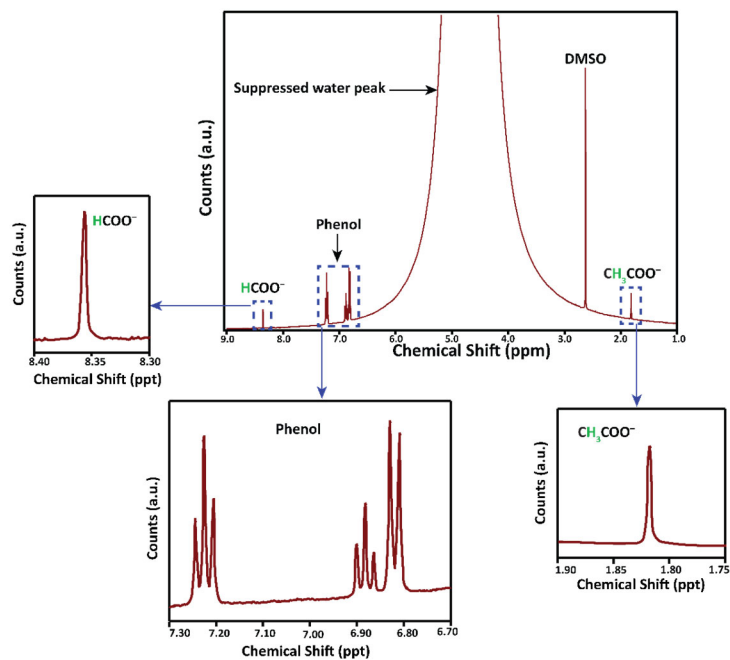


Figure S4.6 ^1H -NMR spectrum of catholyte after electrolysis at -2V for 1 hour. Phenol and DMSO are internal standards. Anolyte 1M KOH and catholyte 1M KHCO_3 .

CHAPTER 5. CONCLUSIONS AND FUTURE DIRECTIONS

Chapter 1 of this dissertation addresses the importance and fundamental aspects of electrochemical ORR and CO₂RR. Both processes are critical to meet global energy demands and to resolve global warming due to CO₂ emission. For the large-scale commercialization of both processes, electrocatalysts should be highly active, stable and cost-effective.

For ORR, precious metal catalysts are currently used in PEM and metal air batteries to gain the required high current density at low overpotential. One major challenge with precious metal catalysts is to reduce their loading amount while maintaining ORR activity. To date, considerable attention has been paid to the development of alternative electrocatalysts to resolve this challenge. One promising approach is to use heteroatom doped carbon materials as metal-free electrocatalysts. These catalysts have been recognized as promising candidates for ORR catalysis because of their unique surface and bulk properties, high availability of dopants, and environmental friendliness. The introduction of heteroatoms such as N or B, S, P into the surface of carbon materials can modulate surface electronic structures. Furthermore, use of co-dopants such as N and B dual doping can boost ORR performance due to their synergistic interaction. Furthermore, N dopants can act as nucleation sites for metal nanoparticles. The unique interaction between N and supported metal nanoparticle may promote stability and activity of metal nanoparticles. This dissertation reports the detailed study of heteroatom doped carbon materials as electrocatalysts as well as a support for metal catalysts for ORR. This dissertation also covers the electrochemical bicarbonate reduction that is catalyzed by copper-coated MEA.

Chapter 2 reports the effect of doping temperature on varying chemical states of N- and B-doped CNOs. The detailed XPS analysis unveils how chemical states of dopants are influenced by the doping temperature. Also, the dopant atoms, defects and associated chemical structures were identified and located by high-resolution STEM technique. Here, it was challenging to recognize boron atoms using STEM because of their low atomic number. Electrochemical performance test identified NB-CNOs prepared at 700 C as a promising catalyst for ORR compared to other NB-CNOs. In the future, this work may be extended as follows. The experimental results can be combined with theoretical calculations to understand the nature of active sites and adsorption/desorption mechanisms. The ORR activity and onset potentials of NB-CNO(700) can be further tuned by introducing non-precious metal nanoparticles which may generate new catalytic sites.

Chapter 3 reports the study to employ N-doped CNOs to support copper nanoparticles for ORR. Besides the issues of high cost and scarcity, one additional critical limitation of precious metal-based, state-of-the-art catalysts is the lack of stability due to detachment, dissolution, and agglomeration of metal catalysts during prolonged operation. To address these challenges, the use of functionalized carbon materials as support is an attractive approach because it may stabilize metal nanoparticles and reduce the amount of metals loaded in the catalyst. This study reports that N-related defects in NCNO provide nucleation sites for the growth of uniformly distributed copper nanoparticles. XPS, EDS and TEM analyses confirm the presence of Cu-N configuration and Cu nanoparticles as small as 2 nm.

In the future STEM study can be performed to visualize the interface of Cu-N and the distribution of copper nanoparticles. Furthermore, computational studies may shed light on the nature of active sites associated with Cu-N configurations. So as to further improve the activity of NCNO supported copper particles for ORR, copper nanoparticles and Cu-N_x/C environment can be modified. To this end, partial substitution of N in Cu-N_x/C structures with other non-metal elements such as B, P, or S is an interesting research direction. Because ORR activity and stability of Cu-N_x/C catalyst highly related to the metal center species and its coordination environment. In addition to this, designing a bimetallic electrocatalyst using NCNO is an exciting option to further promote the activity. Synergistic two metal elements can alter electronic properties of metals due to the coordinating environment and the interactions between them. Considering the amount of dopants that promote the nucleation of metal nanoparticles, CNOs may be limited because CNOs are relatively ordered with less defects and oxygen functional groups. CNOs can be replaced by more disordered carbon materials or dopants can be incorporated through a bottom-up approach (e.g., the pyrolysis of small hydrocarbon molecules with nitrogen precursor).

Chapter 4 focuses on bicarbonate conversion into valuable products using electrocatalysts and electrolyzers. This is pioneering research to convert bicarbonate feedstock to C₂⁺ products (acetate) with copper catalyst. In this work, sputter coated copper on carbon paper is employed as cathode catalyst while Pt/C on carbon is anode. Nafion was as an ionomer in this work. The ionomer in the electrolyzer is important in enhancing mechanical integrity of catalysts. More importantly, the ionomer greatly influences the local pH near electrode that determine the efficiency and selectivity of

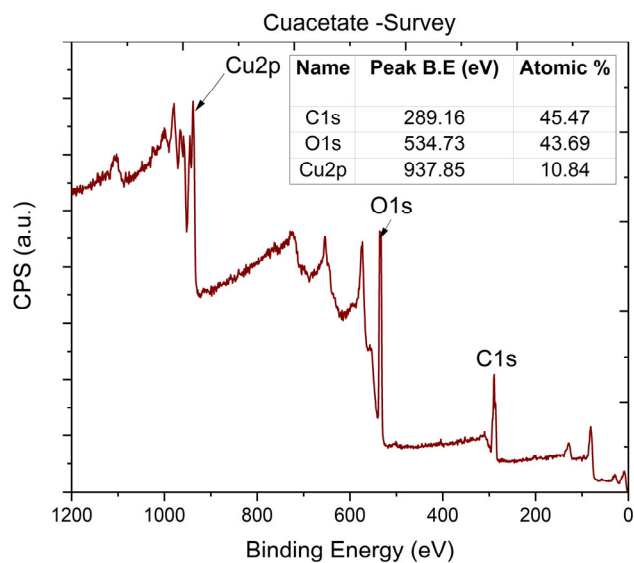
CO₂RR. Nafion has sulfonic groups which are highly acidic (pK_a ~ -6). In the future work, it is worth exploring different types of ionomers with neutral or basic pK_a. This study will shed light on how the local pH affects the efficiency and pathway of CO₂RR.

Our current study reveals the limited current density of bicarbonate reduction. One possible origin for this low current density is inefficient hydrogen oxidation at anode that leads to limited conversion of bicarbonate to CO₂ (g) at cathode. In the current flow cell, H₂ gas, a source of hydrogen oxidation, is fed through a field-flow plate and diffuses through the electrolyte to reach anode for hydrogen oxidation. To improve hydrogen oxidation process, mass transport of H₂ can be directly purged into electrolyte for a short travel to the anode.

This work can be extended by combining sputter coated copper with copper nanoparticles or bimetallic catalysts. Both are useful to stimulate CO₂ reduction activity. This catalyst can be air-brushed on to the sputter coated copper on carbon support. In that way the electrode active surface area and CO₂ mass transport can be increased. Also, the composition of bimetallic catalyst can be tuned to reduce the hydrogen evolution reaction while promoting CO₂ conversion. Although our study found the conversion of bicarbonate to acetate and formate, the mechanisms for the products are unclear. In-situ Spectro electrochemical studies will provide valuable information on reaction pathways. For this goal, in-situ Raman measurements and/or surface-enhanced infrared absorption spectroscopy (SEIRAS) can be performed to determine the nature of CO₂ reactants adsorbed on active sites and the temporal formation of intermediate species.

APPENDIX

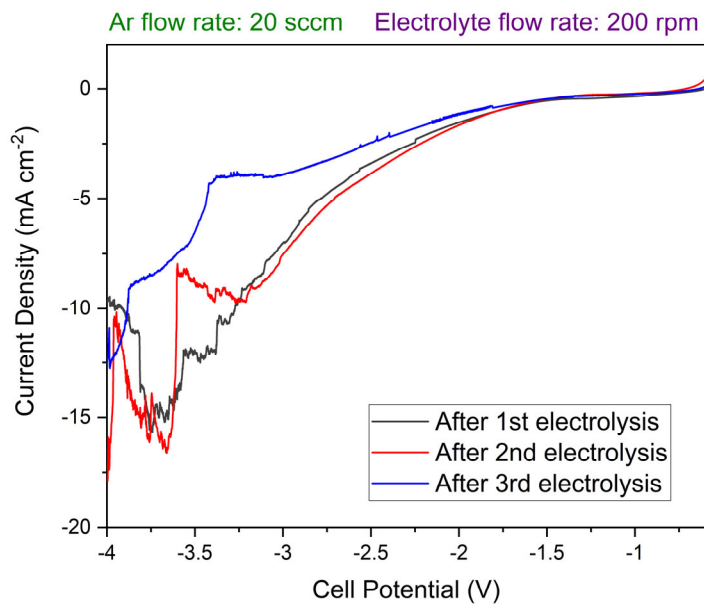
Copper acetate precursor was used as the precursor for the Cu-NCNO synthesis. **XPS survey of copper acetate**



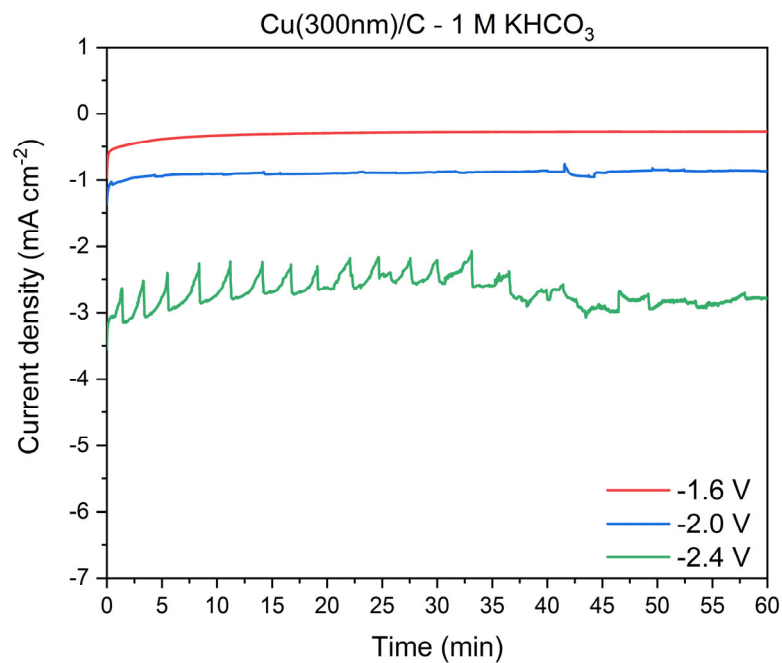
Bicarbonate conversion into valuable products using different membranes.

1. Bipolar membrane

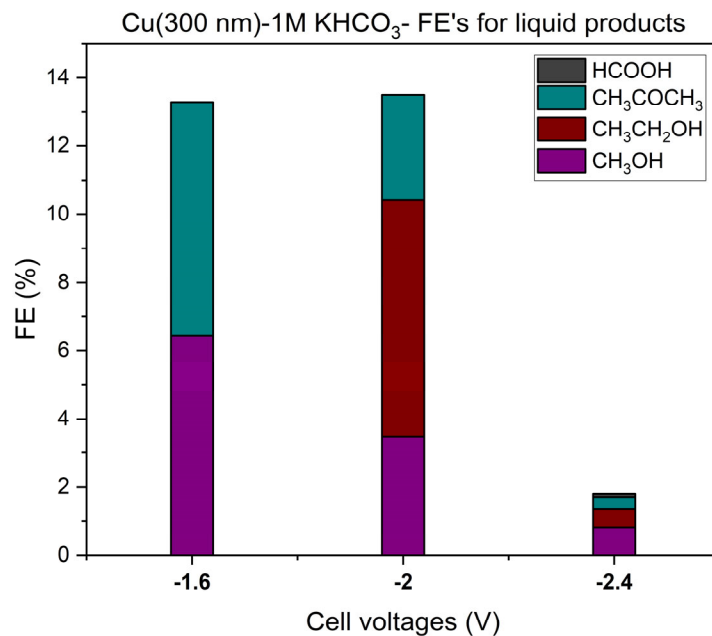
a. Linear sweep voltammogram (LSV)



b. Chronoamperometry (CA) at -1.6, -2.0, -2.4 V.

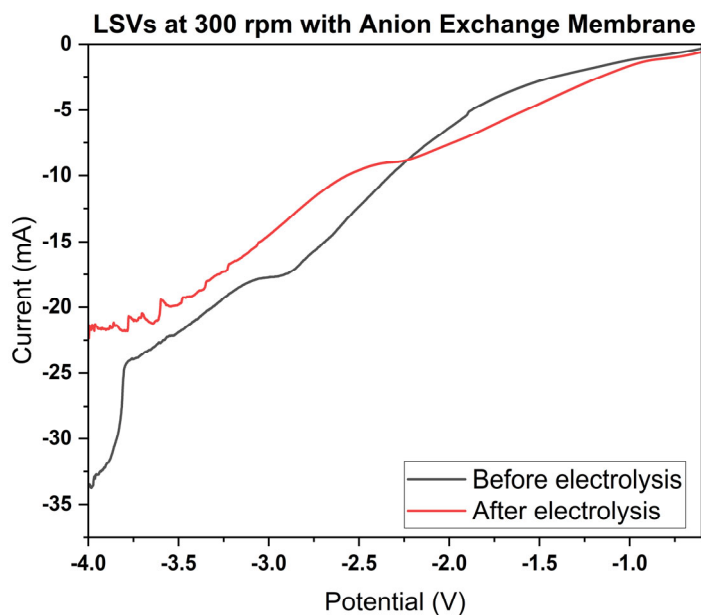


c. Faradaic efficiencies (FE%) for liquid products only.

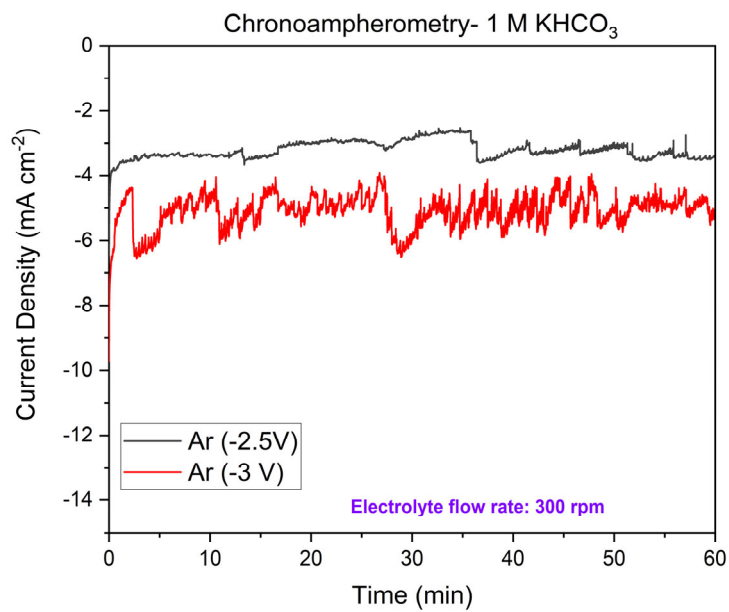


2. Anion exchange membrane (AEM)

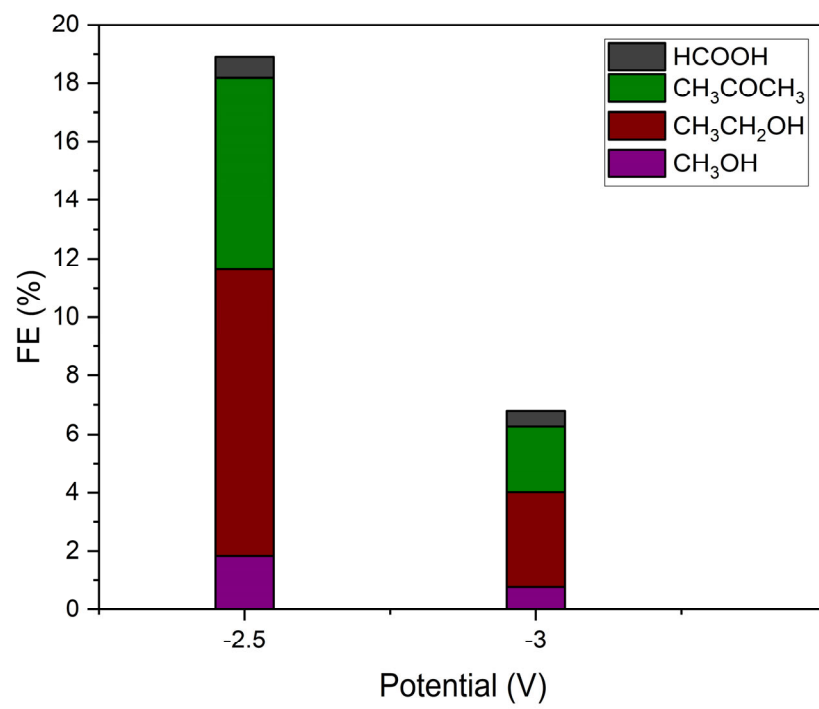
a. LSV



b. Chronoamperometry at -2.5 and -3 V.



c. Faradaic efficiencies only for liquid products.



REFERENCES

1. Ramaswamy, V.; Schwarzkopf, M. D.; Randel, W. J.; Santer, B. D.; Soden, B. J.; Stenchikov, G. L., Anthropogenic and Natural Influences in the Evolution of Lower Stratospheric Cooling. *Science* **2006**, *311* (5764), 1138-1141.
2. U.S. Transportation Sector Greenhouse Gas Emissions 1990 –2019. EPA, Ed. 2021.
3. Javaid, U.; Iqbal, J.; Mehmood, A.; Uppal, A. A., Performance improvement in polymer electrolytic membrane fuel cell based on nonlinear control strategies—A comprehensive study. *PLOS ONE* **2022**, *17* (2).
4. Ludwig, J. R.; Schindler, C. S., Catalyst: Sustainable Catalysis. *Chem* **2017**, *2* (3), 313-316.
5. Sinar Mashuri, S. I.; Ibrahim, M. L.; Kasim, M. F.; Mastuli, M. S.; Rashid, U.; Abdullah, A. H.; Islam, A.; Asikin Mijan, N.; Tan, Y. H.; Mansir, N.; Mohd Kaus, N. H.; Yun Hin, T.-Y., Photocatalysis for Organic Wastewater Treatment: From the Basis to Current Challenges for Society. *Catalysts* **2020**, *10* (11), 1260.
6. Duca, M.; Koper, M. T. M., Fundamental Aspects of Electrocatalysis. *Surface and Interface Science* **2020**, 773-890.
7. Sabatier, P., *La catalyse en chimie organique*. C. Béranger: 1920.
8. Medford, A. J.; Vojvodic, A.; Hummelshøj, J. S.; Voss, J.; Abild-Pedersen, F.; Studt, F.; Bligaard, T.; Nilsson, A.; Nørskov, J. K., From the Sabatier principle to a predictive theory of transition-metal heterogeneous catalysis. *Journal of Catalysis* **2015**, *328*, 36-42.
9. Sebastián-Pascual, P.; Jordão Pereira, I.; Escudero-Escribano, M., Tailored electrocatalysts by controlled electrochemical deposition and surface nanostructuring. *Chemical Communications* **2020**, *56* (87), 13261-13272.
10. Boettcher, S. W.; Oener, S. Z.; Lonergan, M. C.; Surendranath, Y.; Ardo, S.; Brozek, C.; Kempler, P. A., Potentially Confusing: Potentials in Electrochemistry. *ACS Energy Letters* **2021**, *6* (1), 261-266.
11. Brownson, D. A. C.; Banks, C. E., Introduction to Graphene. In *The Handbook of Graphene Electrochemistry*, 2014; pp 1-22.
12. Seeber, R.; Zanardi, C.; Inzelt, G., Links between electrochemical thermodynamics and kinetics. *ChemTexts* **2015**, *1* (4).
13. Bard, A. J.; Faulkner, L. R., *Electrochemical Methods: Fundamentals and Applications, 2nd Edition*. John Wiley & Sons, Incorporated: 2000.
14. Nguyen, T. N.; Dinh, C. T., Gas diffusion electrode design for electrochemical carbon dioxide reduction. *Chem Soc Rev* **2020**, *49* (21), 7488-7504.
15. Yan, W.-Y.; Zheng, S.-L.; Jin, W.; Peng, Z.; Wang, S.-N.; Du, H.; Zhang, Y., The influence of KOH concentration, oxygen partial pressure and temperature on the oxygen reduction reaction at Pt electrodes. *Journal of Electroanalytical Chemistry* **2015**, *741*, 100-108.
16. Krischer, K.; Savinova, E. R., Fundamentals of Electrocatalysis. In *Handbook of Heterogeneous Catalysis*. 2008; pp 1873-1905.
17. Swider-Lyons, K. E.; Campbell, S. A., Physical Chemistry Research Toward Proton Exchange Membrane Fuel Cell Advancement. *The Journal of Physical Chemistry Letters* **2013**, *4* (3), pp 393-401.

18. Dickinson, E. J. F.; Wain, A. J., The Butler-Volmer equation in electrochemical theory: Origins, value, and practical application. *Journal of Electroanalytical Chemistry* **2020**, *872*.
19. Ghassemi, M.; Kamvar, M.; Steinberger-Wilckens, R., Chapter 4 - Fundamentals of electrochemistry. In *Fundamentals of Heat and Fluid Flow in High Temperature Fuel Cells*, Ghassemi, M.; Kamvar, M.; Steinberger-Wilckens, R., Eds. Academic Press: 2020; pp 75-99.
20. Perez, N., Mass Transport by Diffusion and Migration. Springer International Publishing: 2016; pp 151-197.
21. Wanninayake, N.; Ai, Q.; Zhou, R.; Hoque, M. A.; Herrell, S.; Guzman, M. I.; Risko, C.; Kim, D. Y., Understanding the effect of host structure of nitrogen doped ultrananocrystalline diamond electrode on electrochemical carbon dioxide reduction. *Carbon* **2020**, *157*, 408-419.
22. Wang, S.; Jiang, S. P., Prospects of fuel cell technologies. *National Science Review* **2017**, *4* (2), pp 163-166.
23. Zhang, J.; Yang, H.; Liu, B., Coordination Engineering of Single-Atom Catalysts for the Oxygen Reduction Reaction: A Review. *Advanced Energy Materials* **2021**, *11* (3), 2002473.
24. Ma, R.; Lin, G.; Zhou, Y.; Liu, Q.; Zhang, T.; Shan, G.; Yang, M.; Wang, J., A review of oxygen reduction mechanisms for metal-free carbon-based electrocatalysts. *npj Computational Materials* **2019**, *5* (1).
25. Gong, Y.; Fei, H.; Zou, X.; Zhou, W.; Yang, S.; Ye, G.; Liu, Z.; Peng, Z.; Lou, J.; Vajtai, R.; Yakobson, B. I.; Tour, J. M.; Ajayan, P. M., Boron- and Nitrogen-Substituted Graphene Nanoribbons as Efficient Catalysts for Oxygen Reduction Reaction. *Chemistry of Materials* **2015**, *27* (4), pp 1181-1186.
26. Li, X.; Heryadi, D.; Gewirth, A. A., Electroreduction Activity of Hydrogen Peroxide on Pt and Au Electrodes. *Langmuir* **2005**, *21* (20), pp 9251-9259.
27. Wang, Y.; Zhang, D.; Liu, H., A study of the catalysis of cobalt hydroxide towards the oxygen reduction in alkaline media. *Journal of Power Sources* **2010**, *195* (10), pp 3135-3139.
28. Park, K. Y.; Sweers, M. E.; Berner, U.; Hirth, E.; Downing, J. R.; Hui, J.; Mailoa, J.; Johnston, C.; Kim, S.; Seitz, L. C.; Hersam, M. C., Mitigating Pt Loss in Polymer Electrolyte Membrane Fuel Cell Cathode Catalysts Using Graphene Nanoplatelet Pickering Emulsion Processing. *Advanced Functional Materials* **2022**.
29. Yang, J.; Kim, S. H.; Kwak, S. K.; Song, H. K., Curvature-Induced Metal-Support Interaction of an Islands-by-Islands Composite of Platinum Catalyst and Carbon Nano-onion for Durable Oxygen Reduction. *ACS Appl Mater Interfaces* **2017**, *9* (28), pp 23302-23308.
30. Zhang, S.; Shao, Y.; Yin, G.; Lin, Y., Recent progress in nanostructured electrocatalysts for PEM fuel cells. *Journal of Materials Chemistry A* **2013**, *1* (15), p 4631.
31. Nagappan, S.; Duraiavel, M.; Hira, S. A.; Prabakar, K.; Ha, C.-S.; Joo, S. H.; Nam, K. M.; Park, K. H., Heteroatom-doped nanomaterials/core-shell nanostructure based electrocatalysts for the oxygen reduction reaction. *Journal of Materials Chemistry A* **2022**, *10* (3), pp 987-1021.

32. Zhou, S.; Liu, N.; Wang, Z.; Zhao, J., Nitrogen-Doped Graphene on Transition Metal Substrates as Efficient Bifunctional Catalysts for Oxygen Reduction and Oxygen Evolution Reactions. *ACS Applied Materials & Interfaces* **2017**, *9* (27), pp 22578-22587.
33. Zhang, J.; Xia, Z.; Dai, L., Carbon-based electrocatalysts for advanced energy conversion and storage. *Science Advances* **2015**, *1* (7).
34. Gong, K.; Du, F.; Xia, Z.; Durstock, M.; Dai, L., Nitrogen-Doped Carbon Nanotube Arrays with High Electrocatalytic Activity for Oxygen Reduction. *Science* **2009**, *323* (5915), pp 760-764.
35. Hu, C.; Dai, L., Carbon-Based Metal-Free Catalysts for Electrocatalysis beyond the ORR. *Angewandte Chemie International Edition* **2016**, *55* (39), pp 11736-11758.
36. Jiao, Y.; Zheng, Y.; Jaroniec, M.; Qiao, S. Z., Origin of the Electrocatalytic Oxygen Reduction Activity of Graphene-Based Catalysts: A Roadmap to Achieve the Best Performance. *Journal of the American Chemical Society* **2014**, *136* (11), pp 4394-4403.
37. Jin, J.; Pan, F.; Jiang, L.; Fu, X.; Liang, A.; Wei, Z.; Zhang, J.; Sun, G., Catalyst-Free Synthesis of Crumpled Boron and Nitrogen Co-Doped Graphite Layers with Tunable Bond Structure for Oxygen Reduction Reaction. *ACS Nano* **2014**, *8* (4), pp 3313-3321.
38. Le Quéré, C.; Andrew, R. M.; Friedlingstein, P.; Sitch, S.; Hauck, J.; Pongratz, J.; Pickers, P. A.; Korsbakken, J. I.; Peters, G. P.; Canadell, J. G.; Arneeth, A.; Arora, V. K.; Barbero, L.; Bastos, A.; Bopp, L.; Chevallier, F.; Chini, L. P.; Ciais, P.; Doney, S. C.; Gkritzalis, T.; Goll, D. S.; Harris, I.; Haverd, V.; Hoffman, F. M.; Hoppema, M.; Houghton, R. A.; Hurtt, G.; Ilyina, T.; Jain, A. K.; Johannessen, T.; Jones, C. D.; Kato, E.; Keeling, R. F.; Goldewijk, K. K.; Landschützer, P.; Lefèvre, N.; Lienert, S.; Liu, Z.; Lombardozzi, D.; Metzl, N.; Munro, D. R.; Nabel, J. E. M. S.; Nakaoka, S.-I.; Neill, C.; Olsen, A.; Ono, T.; Patra, P.; Peregon, A.; Peters, W.; Peylin, P.; Pfeil, B.; Pierrot, D.; Poulter, B.; Rehder, G.; Resplandy, L.; Robertson, E.; Rocher, M.; Rödenbeck, C.; Schuster, U.; Schwinger, J.; Séférian, R.; Skjelvan, I.; Steinhoff, T.; Sutton, A.; Tans, P. P.; Tian, H.; Tilbrook, B.; Tubiello, F. N.; Van Der Laan-Luijkx, I. T.; Van Der Werf, G. R.; Viovy, N.; Walker, A. P.; Wiltshire, A. J.; Wright, R.; Zaehle, S.; Zheng, B., Global Carbon Budget 2018. *Earth System Science Data* **2018**, *10* (4), pp 2141-2194.
39. Kauw, M.; Benders, R. M. J.; Visser, C., Green methanol from hydrogen and carbon dioxide using geothermal energy and/or hydropower in Iceland or excess renewable electricity in Germany. *Energy* **2015**, *90*, pp 208-217.
40. Sharifian, R.; Wagterveld, R. M.; Digdaya, I. A.; Xiang, C.; Vermaas, D. A., Electrochemical carbon dioxide capture to close the carbon cycle. *Energy & Environmental Science* **2021**, *14* (2), pp 781-814.
41. Sullivan, I.; Goryachev, A.; Digdaya, I. A.; Li, X.; Atwater, H. A.; Vermaas, D. A.; Xiang, C., Coupling electrochemical CO₂ conversion with CO₂ capture. *Nature Catalysis* **2021**, *4* (11), pp 952-958.
42. Digdaya, I. A.; Sullivan, I.; Lin, M.; Han, L.; Cheng, W.-H.; Atwater, H. A.; Xiang, C., A direct coupled electrochemical system for capture and conversion of CO₂ from oceanwater. *Nature Communications* **2020**, *11* (1).

43. Welch, A. J.; Dunn, E.; DuChene, J. S.; Atwater, H. A., Bicarbonate or Carbonate Processes for Coupling Carbon Dioxide Capture and Electrochemical Conversion. *ACS Energy Letters* **2020**, *5* (3), pp 940-945.
44. Badwal, S. P. S.; Giddey, S. S.; Munnings, C.; Bhatt, A. I.; Hollenkamp, A. F., Emerging electrochemical energy conversion and storage technologies. *Frontiers in Chemistry* **2014**, *2*.
45. He, F.; Zheng, Y.; Fan, H.; Ma, D.; Chen, Q.; Wei, T.; Wu, W.; Wu, D.; Hu, X., Oxidase-Inspired Selective 2e/4e Reduction of Oxygen on Electron-Deficient Cu. *ACS Applied Materials & Interfaces* **2020**, *12* (4), pp 4833-4842.
46. Zhao, Y.; Yang, L.; Chen, S.; Wang, X.; Ma, Y.; Wu, Q.; Jiang, Y.; Qian, W.; Hu, Z., Can boron and nitrogen co-doping improve oxygen reduction reaction activity of carbon nanotubes? *J Am Chem Soc* **2013**, *135* (4), pp 1201-4.
47. Zhao, S.; Wang, D. W.; Amal, R.; Dai, L., Carbon-Based Metal-Free Catalysts for Key Reactions Involved in Energy Conversion and Storage. *Advanced Materials* **2019**, *31* (9), p 1801526.
48. Bag, S.; Mondal, B.; Das, A. K.; Raj, C. R., Nitrogen and Sulfur Dual-Doped Reduced Graphene Oxide: Synergistic Effect of Dopants Towards Oxygen Reduction Reaction. *Electrochimica Acta* **2015**, *163*, pp 16-23.
49. Thomas, M. P.; Wanninayake, N.; De Alwis Goonatileke, M.; Kim, D. Y.; Guiton, B. S., Direct imaging of heteroatom dopants in catalytic carbon nano-onions. *Nanoscale* **2020**, *12* (10), pp 6144-6152.
50. Zhang, M.; Tao, H.; Liu, Y.; Yan, C.; Hong, S.; Masa, J.; Robertson, A. W.; Liu, S.; Qiu, J.; Sun, Z., Ultrasound-Assisted Nitrogen and Boron Codoping of Graphene Oxide for Efficient Oxygen Reduction Reaction. *ACS Sustainable Chemistry & Engineering* **2019**, *7* (3), pp 3434-3442.
51. Bartelmeß, J.; Giordani, S., Carbon nano-onions (multi-layer fullerenes): chemistry and applications. *Beilstein Journal of Nanotechnology* **2014**, *5*, pp 1980-1998.
52. Zeiger, M.; Jäckel, N.; Mochalin, V. N.; Presser, V., Review: carbon onions for electrochemical energy storage. *Journal of Materials Chemistry A* **2016**, *4* (9), pp 3172-3196.
53. McDonough, J. K.; Gogotsi, Y., Carbon Onions: Synthesis and Electrochemical Applications. *Interface magazine* **2013**, *22* (3), pp 61-66.
54. Camisasca, A.; Sacco, A.; Brescia, R.; Giordani, S., Boron/Nitrogen-Codoped Carbon Nano-Onion Electrocatalysts for the Oxygen Reduction Reaction. *ACS Applied Nano Materials* **2018**, *1* (10), pp 5763-5773.
55. Mykhailiv, O.; Zubyk, H.; Plonska-Brzezinska, M. E., Carbon nano-onions: Unique carbon nanostructures with fascinating properties and their potential applications. *Inorganica Chimica Acta* **2017**, *468*, pp 49-66.
56. Frasconi, M.; Maffei, V.; Bartelmeß, J.; Echegoyen, L.; Giordani, S., Highly surface functionalized carbon nano-onions for bright light bioimaging. *Methods Appl Fluoresc* **2015**, *3* (4), p 044005.
57. Hashim, D. P.; Narayanan, N. T.; Romo-Herrera, J. M.; Cullen, D. A.; Hahn, M. G.; Lezzi, P.; Suttle, J. R.; Kelkhoff, D.; Muñoz-Sandoval, E.; Ganguli, S.; Roy, A. K.; Smith, D. J.; Vajtai, R.; Sumpter, B. G.; Meunier, V.; Terrones, H.; Terrones, M.; Ajayan, P. M., Covalently bonded three-dimensional carbon nanotube solids via boron induced nanojunctions. *Scientific Reports* **2012**, *2* (1).

58. Mykhailiv, O.; Brzezinski, K.; Sulikowski, B.; Olejniczak, Z.; Gras, M.; Lota, G.; Molina-Ontoria, A.; Jakubczyk, M.; Echegoyen, L.; Plonska-Brzezinska, M. E., Boron-Doped Polygonal Carbon Nano-Onions: Synthesis and Applications in Electrochemical Energy Storage. *Chemistry – A European Journal* **2017**, *23* (29), pp 7132-7141.
59. Lin, Y.; Zhu, Y.; Zhang, B.; Kim, Y. A.; Endo, M.; Su, D. S., Boron-doped onion-like carbon with enriched substitutional boron: the relationship between electronic properties and catalytic performance. *Journal of Materials Chemistry A* **2015**, *3* (43), pp 21805-21814.
60. Lu, X.; Chen, L., Boron-Doped Carbon Nano-/Microballs from Orthoboric Acid-Starch: Preparation, Characterization, and Lithium Ion Storage Properties. *Journal of Nanomaterials* **2018**, *2018*, pp 1-8.
61. Singh, A. K.; Yasri, N.; Karan, K.; Roberts, E. P. L., Electrocatalytic Activity of Functionalized Carbon Paper Electrodes and Their Correlation to the Fermi Level Derived from Raman Spectra. *ACS Applied Energy Materials* **2019**, *2* (3), pp 2324-2336.
62. Ferrari, A. C.; Basko, D. M., Raman spectroscopy as a versatile tool for studying the properties of graphene. *Nature Nanotechnology* **2013**, *8* (4), pp 235-246.
63. Beams, R.; Gustavo Cançado, L.; Novotny, L., Raman characterization of defects and dopants in graphene. *Journal of Physics: Condensed Matter* **2015**, *27* (8), p 083002.
64. Tang, B.; Guoxin, H.; Gao, H., Raman Spectroscopic Characterization of Graphene. *Applied Spectroscopy Reviews* **2010**, *45* (5), pp 369-407.
65. Parambath, V. B.; Nagar, R.; Ramaprabhu, S., Effect of Nitrogen Doping on Hydrogen Storage Capacity of Palladium Decorated Graphene. *Langmuir* **2012**, *28* (20), pp 7826-7833.
66. Kim, Y. A.; Fujisawa, K.; Muramatsu, H.; Hayashi, T.; Endo, M.; Fujimori, T.; Kaneko, K.; Terrones, M.; Behrends, J.; Eckmann, A.; Casiraghi, C.; Novoselov, K. S.; Saito, R.; Dresselhaus, M. S., Raman Spectroscopy of Boron-Doped Single-Layer Graphene. *ACS Nano* **2012**, *6* (7), pp 6293-6300.
67. Lin, Y.-C.; Teng, P.-Y.; Yeh, C.-H.; Koshino, M.; Chiu, P.-W.; Suenaga, K., Structural and Chemical Dynamics of Pyridinic-Nitrogen Defects in Graphene. *Nano Letters* **2015**, *15* (11), pp 7408-7413.
68. Lee, Y.-J.; Uchiyama, Y.; Radovic, L. R., Effects of boron doping in low- and high-surface-area carbon powders. *Carbon* **2004**, *42* (11), pp 2233-2244.
69. Li, Z. Q.; Lu, C. J.; Xia, Z. P.; Zhou, Y.; Luo, Z., X-ray diffraction patterns of graphite and turbostratic carbon. *Carbon* **2007**, *45* (8), pp 1686-1695.
70. Moussa, G.; Matei Ghimbeu, C.; Taberna, P.-L.; Simon, P.; Vix-Guterl, C., Relationship between the carbon nano-onions (CNOs) surface chemistry/defects and their capacitance in aqueous and organic electrolytes. *Carbon* **2016**, *105*, pp 628-637.
71. Kim, S.-M.; Heo, Y.-K.; Bae, K.-T.; Oh, Y.-T.; Lee, M.-H.; Lee, S.-Y., In situ formation of nitrogen-doped onion-like carbon as catalyst support for enhanced oxygen reduction activity and durability. *Carbon* **2016**, *101*, pp 420-430.
72. Zheng, Y.; Jiao, Y.; Ge, L.; Jaroniec, M.; Qiao, S. Z., Two-Step Boron and Nitrogen Doping in Graphene for Enhanced Synergistic Catalysis. *Angewandte Chemie* **2013**, *125* (11), pp 3192-3198.
73. Tian, Z.; Zhang, Q.; Thomsen, L.; Gao, N.; Pan, J.; Daiyan, R.; Yun, J.; Brandt, J.; López-Salas, N.; Lai, F.; Li, Q.; Liu, T.; Amal, R.; Lu, X.; Antonietti, M.,

Constructing Interfacial Boron-Nitrogen Moieties in Turbostratic Carbon for Electrochemical Hydrogen Peroxide Production. *Angewandte Chemie International Edition* **2022**.

74. Rao, C. N. R.; Gopalakrishnan, K.; Govindaraj, A., Synthesis, properties and applications of graphene doped with boron, nitrogen and other elements. *Nano Today* **2014**, *9* (3), pp 324-343.

75. Li, X.; Wang, X.; Xiao, G.; Zhu, Y., Identifying active sites of boron, nitrogen co-doped carbon materials for the oxygen reduction reaction to hydrogen peroxide. *Journal of Colloid and Interface Science* **2021**, *602*, pp 799-809.

76. Scardamaglia, M.; Bittencourt, C., Metal-free catalysis based on nitrogen-doped carbon nanomaterials: a photoelectron spectroscopy point of view. *Beilstein J Nanotechnol* **2018**, *9*, pp 2015-2031.

77. Ning, X.; Li, Y.; Ming, J.; Wang, Q.; Wang, H.; Cao, Y.; Peng, F.; Yang, Y.; Yu, H., Electronic synergism of pyridinic- and graphitic-nitrogen on N-doped carbons for the oxygen reduction reaction. *Chem Sci* **2019**, *10* (6), pp 1589-1596.

78. Wang, S.; Zhang, L.; Xia, Z.; Roy, A.; Chang, D. W.; Baek, J.-B.; Dai, L., BCN Graphene as Efficient Metal-Free Electrocatalyst for the Oxygen Reduction Reaction. *Angewandte Chemie International Edition* **2012**, *51* (17), pp 4209-4212.

79. Wu, J.; Rodrigues, M.-T. F.; Vajtai, R.; Ajayan, P. M., Tuning the Electrochemical Reactivity of Boron- and Nitrogen-Substituted Graphene. *Advanced Materials* **2016**, *28* (29), pp 6239-6246.

80. Tripković, A. V.; Popović, K. D.; Lović, J. D.; Jovanović, V. M.; Kowal, A., Methanol oxidation at platinum electrodes in alkaline solution: comparison between supported catalysts and model systems. *Journal of Electroanalytical Chemistry* **2004**, *572* (1), pp 119-128.

81. Cançado, L. G.; Jorio, A.; Ferreira, E. H. M.; Stavale, F.; Achete, C. A.; Capaz, R. B.; Moutinho, M. V. O.; Lombardo, A.; Kulmala, T. S.; Ferrari, A. C., Quantifying Defects in Graphene via Raman Spectroscopy at Different Excitation Energies. *Nano Letters* **2011**, *11* (8), pp 3190-3196.

82. Chae, S.; Panomsuwan, G.; Bratescu, M. A.; Teshima, K.; Saito, N., p-Type Doping of Graphene with Cationic Nitrogen. *ACS Applied Nano Materials* **2019**, *2* (3), pp 1350-1355.

83. Guo, D.; Shibuya, R.; Akiba, C.; Saji, S.; Kondo, T.; Nakamura, J., Active sites of nitrogen-doped carbon materials for oxygen reduction reaction clarified using model catalysts. *Science* **2016**, *351* (6271), pp 361-365.

84. Li, Y. Probing the Response of Two-Dimensional Crystals by Optical Spectroscopy. Columbia University, 2014.

85. Yutomo, E. B.; Noor, F. A.; Winata, T., Effect of the number of nitrogen dopants on the electronic and magnetic properties of graphitic and pyridinic N-doped graphene – a density-functional study. *RSC Advances* **2021**, *11* (30), pp 18371-18380.

86. Roy, D.; Chhowalla, M.; Wang, H.; Sano, N.; Alexandrou, I.; Clyne, T. W.; Amaratunga, G. A. J., Characterisation of carbon nano-onions using Raman spectroscopy. *Chemical Physics Letters* **2003**, *373* (1-2), pp 52-56.

87. Duan, X.; Son, H.; Gao, B.; Zhang, J.; Wu, T.; Samsonidze, G. G.; Dresselhaus, M. S.; Liu, Z.; Kong, J., Resonant Raman Spectroscopy of Individual Strained Single-Wall Carbon Nanotubes. **2007**, *7* (7), pp 2116-2121.

88. Zheng, Y.; Ma, Y.; Tao, Q.; Li, Y.; Ma, S.; Cui, T.; Wang, X.; Dong, S.; Zhu, P., Pressure induced structural transition of small carbon nano-onions. *RSC Advances* **2016**, *6* (4), 2914-2919.
89. Chatterjee, K.; Ashokkumar, M.; Gullapalli, H.; Gong, Y.; Vajtai, R.; Thanikaivelan, P.; Ajayan, P. M., Nitrogen-rich carbon nano-onions for oxygen reduction reaction. *Carbon* **2018**, *130*, pp 645-651.
90. Wang, Y.; Wang, D.; Li, Y., A fundamental comprehension and recent progress in advanced Pt-based ORR nanocatalysts. *SmartMat* **2021**, *2* (1), pp 56-75.
91. Holade, Y.; Servat, K.; Tingry, S.; Napporn, T. W.; Remita, H.; Cornu, D.; Kokoh, K. B., Advances in Electrocatalysis for Energy Conversion and Synthesis of Organic Molecules. *ChemPhysChem* **2017**, *18* (19), 2573-2605.
92. Li, Y.; Wang, H.; Priest, C.; Li, S.; Xu, P.; Wu, G., Advanced Electrocatalysis for Energy and Environmental Sustainability via Water and Nitrogen Reactions. *Advanced Materials* **2021**, *33* (6), p 2000381.
93. Fei, H.; Dong, J.; Chen, D.; Hu, T.; Duan, X.; Shakir, I.; Huang, Y.; Duan, X., Single atom electrocatalysts supported on graphene or graphene-like carbons. *Chemical Society Reviews* **2019**, *48* (20), pp 5207-5241.
94. Ponomarev, I. I.; Zhigalina, O. M.; Skupov, K. M.; Modestov, A. D.; Basu, V. G.; Sufiyanova, A. E.; Ponomarev, I. I.; Razorenov, D. Y., Preparation and thermal treatment influence on Pt-decorated electrospun carbon nanofiber electrocatalysts. *RSC Advances* **2019**, *9* (47), 27406-27418.
95. Bai, L.; Hou, C.; Wen, X.; Guan, J., Catalysis of Oxygen Reduction Reaction on Atomically Dispersed Copper- and Nitrogen-Codoped Graphene. *ACS Applied Energy Materials* **2019**, *2* (7), pp 4755-4762.
96. Sugimoto, W.; Takimoto, D., Platinum Group Metal-based Nanosheets: Synthesis and Application towards Electrochemical Energy Storage and Conversion. *Chemistry Letters* **2021**, *50* (6), pp 1304-1312.
97. Tachibana, N.; Yukawa, Y.; Morikawa, K.; Kawaguchi, M.; Shimano, K., Pt nanoparticles supported on nitrogen-doped porous carbon as efficient oxygen reduction catalysts synthesized via a simple alcohol reduction method. *SN Applied Sciences* **2021**, *3* (3).
98. Kodama, K.; Nagai, T.; Kuwaki, A.; Jinnouchi, R.; Morimoto, Y., Challenges in applying highly active Pt-based nanostructured catalysts for oxygen reduction reactions to fuel cell vehicles. *Nature Nanotechnology* **2021**, *16* (2), pp 140-147.
99. Shao-Horn, Y.; Sheng, W. C.; Chen, S.; Ferreira, P. J.; Holby, E. F.; Morgan, D., Instability of Supported Platinum Nanoparticles in Low-Temperature Fuel Cells. *Topics in Catalysis* **2007**, *46* (3-4), pp 285-305.
100. Hughes, A. E.; Haque, N.; Northey, S. A.; Giddey, S., Platinum Group Metals: A Review of Resources, Production and Usage with a Focus on Catalysts. *Resources* **2021**, *10* (9), 93.
101. Gawande, M. B.; Goswami, A.; Felpin, F.-X.; Asefa, T.; Huang, X.; Silva, R.; Zou, X.; Zboril, R.; Varma, R. S., Cu and Cu-Based Nanoparticles: Synthesis and Applications in Catalysis. *Chemical Reviews* **2016**, *116* (6), pp 3722-3811.
102. He, J.; Zheng, T.; Wu, D.; Zhang, S.; Gu, M.; He, Q., Insights into the Determining Effect of Carbon Support Properties on Anchoring Active Sites in Fe-N-C

Catalysts toward the Oxygen Reduction Reaction. *ACS Catalysis* **2022**, *12* (3), pp 1601-1613.

103. Li, F.; Han, G.-F.; Noh, H.-J.; Kim, S.-J.; Lu, Y.; Jeong, H. Y.; Fu, Z.; Baek, J.-B., Boosting oxygen reduction catalysis with abundant copper single atom active sites. *Energy & Environmental Science* **2018**, *11* (8), 2263-2269.

104. Li, J.; Zhou, N.; Song, J.; Fu, L.; Yan, J.; Tang, Y.; Wang, H., Cu-MOF-Derived Cu/Cu₂O Nanoparticles and Cu_NxCy Species to Boost Oxygen Reduction Activity of Ketjenblack Carbon in Al-Air Battery. *ACS Sustainable Chemistry & Engineering* **2018**, *6* (1), pp 413-421.

105. Li, W.; Min, C.; Tan, F.; Li, Z.; Zhang, B.; Si, R.; Xu, M.; Liu, W.; Zhou, L.; Wei, Q.; Zhang, Y.; Yang, X., Bottom-Up Construction of Active Sites in a Cu-N₄-C Catalyst for Highly Efficient Oxygen Reduction Reaction. *ACS Nano* **2019**, *13* (3), pp 3177-3187.

106. Yang, X.-F.; Wang, A.; Qiao, B.; Li, J.; Liu, J.; Zhang, T., Single-Atom Catalysts: A New Frontier in Heterogeneous Catalysis. *Accounts of Chemical Research* **2013**, *46* (8), pp 1740-1748.

107. Liu, J.-C.; Tang, Y.; Wang, Y.-G.; Zhang, T.; Li, J., Theoretical understanding of the stability of single-atom catalysts. *National Science Review* **2018**, *5* (5), pp 638-641.

108. Lee, J. A.; Lee, W. J.; Lim, J.; Kim, S. O., N-Dopant-Mediated Growth of Metal Oxide Nanoparticles on Carbon Nanotubes. *Nanomaterials* **2021**, *11* (8), p 1882.

109. Zhang, Y.; Ye, S.; Gao, M.; Li, Y.; Huang, X.; Song, J.; Cai, H.; Zhang, Q.; Zhang, J., N-Doped Graphene Supported Cu Single Atoms: Highly Efficient Recyclable Catalyst for Enhanced C-N Coupling Reactions. *ACS Nano* **2022**, *16* (1), pp 1142-1149.

110. Morales-Torres, S.; Pérez-Cadenas, A. F.; Carrasco-Marín, F., Element-Doped Functional Carbon-Based Materials. *Materials* **2020**, *13* (2), p 333.

111. Zhou, R.; Zheng, Y.; Hulicova-Jurcakova, D.; Qiao, S. Z., Enhanced electrochemical catalytic activity by copper oxide grown on nitrogen-doped reduced graphene oxide. *Journal of Materials Chemistry A* **2013**, *1* (42), p 13179.

112. Thanh, N. T. K.; Maclean, N.; Mahiddine, S., Mechanisms of Nucleation and Growth of Nanoparticles in Solution. *Chemical Reviews* **2014**, *114* (15), pp 7610-7630.

113. Mabena, L. F.; Sinha Ray, S.; Mhlanga, S. D.; Coville, N. J., Nitrogen-doped carbon nanotubes as a metal catalyst support. *Applied Nanoscience* **2011**, *1* (2), pp 67-77.

114. Ramu, V. G.; Bordoloi, A.; Nagaiah, T. C.; Schuhmann, W.; Muhler, M.; Cabrele, C., Copper nanoparticles stabilized on nitrogen-doped carbon nanotubes as efficient and recyclable catalysts for alkyne/aldehyde/cyclic amine A₃-type coupling reactions. *Applied Catalysis A: General* **2012**, *431-432*, pp 88-94.

115. Chen, X.; Deng, D.; Pan, X.; Hu, Y.; Bao, X., N-doped graphene as an electron donor of iron catalysts for CO hydrogenation to light olefins. *Chemical Communications* **2015**, *51* (1), pp 217-220.

116. He, L.; Weniger, F.; Neumann, H.; Beller, M., Synthesis, Characterization, and Application of Metal Nanoparticles Supported on Nitrogen-Doped Carbon: Catalysis beyond Electrochemistry. *Angewandte Chemie International Edition* **2016**, *55* (41), pp 12582-12594.

117. Jin, J.; Pan, F.; Jiang, L.; Fu, X.; Liang, A.; Wei, Z.; Zhang, J.; Sun, G., Catalyst-Free Synthesis of Crumpled Boron and Nitrogen Co-Doped Graphite Layers with Tunable Bond Structure for Oxygen Reduction Reaction. **2014**, *8* (4), pp 3313-3321.

118. Tsybizova, A.; Ryland, B. L.; Tsierkezos, N.; Stahl, S. S.; Roithová, J.; Schröder, D., Speciation Behavior of Copper(II) Acetate in Simple Organic Solvents – Revealing the Effect of Trace Water. *European Journal of Inorganic Chemistry* **2014**, *2014* (8), 1407-1412.
119. Guo, K.; Rowland, L. J.; Isherwood, L. H.; Glodan, G.; Baidak, A., Photon-induced synthesis of ultrafine metal nanoparticles on graphene as electrocatalysts: impact of functionalization and doping. *Journal of Materials Chemistry A* **2020**, *8* (2), pp 714-723.
120. Parish, E. J.; Kizito, S. A., Copper(I) Acetate. *Encyclopedia of Reagents for Organic Synthesis* **2001**.
121. Li, W.; Min, C.; Tan, F.; Li, Z.; Zhang, B.; Si, R.; Xu, M.; Liu, W.; Zhou, L.; Wei, Q.; Zhang, Y.; Yang, X., Bottom-Up Construction of Active Sites in a Cu–N₄–C Catalyst for Highly Efficient Oxygen Reduction Reaction. *ACS Nano* **2019**, *13* (3), 3177-3187.
122. Selvakumar, K.; Senthil Kumar, S. M.; Thangamuthu, R.; Ganesan, K.; Murugan, P.; Rajput, P.; Jha, S. N.; Bhattacharyya, D., Physicochemical Investigation of Shape-Designed MnO₂ Nanostructures and Their Influence on Oxygen Reduction Reaction Activity in Alkaline Solution. *The Journal of Physical Chemistry C* **2015**, *119* (12), pp 6604-6618.
123. Kokawa, R.; Ohta, M.; Sasahara, A.; Onishi, H., Kelvin Probe Force Microscopy Study of a Pt/TiO₂ Catalyst Model Placed in an Atmospheric Pressure of N₂ Environment. *Chemistry - An Asian Journal* **2012**, *7* (6), pp 1251-1255.
124. Datta, A.; Ziadi, Z.; Kumar, P.; Sasaki, T.; Danielson, E.; Porkovich, A. J., Utilizing ballistic nanoparticle impact to reconfigure the metal support interaction in Pt-TiN electrocatalysts. *Nanoscale Horiz* **2020**, *5* (10), pp 1407-1414.
125. *Kelvin Probe Force Microscopy*. Springer Berlin, Heidelberg: 2012.
126. Peljo, P.; Manzanares, J. A.; Girault, H. H., Contact Potentials, Fermi Level Equilibration, and Surface Charging. *Langmuir* **2016**, *32* (23), pp 5765-5775.
127. Yan, X.-Y.; Tong, X.-L.; Zhang, Y.-F.; Han, X.-D.; Wang, Y.-Y.; Jin, G.-Q.; Qin, Y.; Guo, X.-Y., Cuprous oxide nanoparticles dispersed on reduced graphene oxide as an efficient electrocatalyst for oxygen reduction reaction. *Chemical Communications* **2012**, *48* (13), p 1892.
128. Lee, H.; Lee, W.; Lee, J. H.; Yoon, D. S., Surface Potential Analysis of Nanoscale Biomaterials and Devices Using Kelvin Probe Force Microscopy. *Journal of Nanomaterials* **2016**, *2016*, pp 1-21.
129. Li, F.; Han, G.-F.; Noh, H.-J.; Kim, S.-J.; Lu, Y.; Jeong, H. Y.; Fu, Z.; Baek, J.-B., Boosting oxygen reduction catalysis with abundant copper single atom active sites. *Energy & Environmental Science* **2018**, *11* (8), pp 2263-2269.
130. Cui, L.; Cui, L.; Li, Z.; Zhang, J.; Wang, H.; Lu, S.; Xiang, Y., A copper single-atom catalyst towards efficient and durable oxygen reduction for fuel cells. *Journal of Materials Chemistry A* **2019**, *7* (28), pp 16690-16695.
131. Tong, M.; Sun, F.; Xie, Y.; Wang, Y.; Yang, Y.; Tian, C.; Wang, L.; Fu, H., Operando Cooperated Catalytic Mechanism of Atomically Dispersed Cu–N and Zn–N for Promoting Oxygen Reduction Reaction. *Angewandte Chemie International Edition* **2021**, *60* (25), pp 14005-14012.

132. Yang, J.; Liu, W.; Xu, M.; Liu, X.; Qi, H.; Zhang, L.; Yang, X.; Niu, S.; Zhou, D.; Liu, Y.; Su, Y.; Li, J.-F.; Tian, Z.-Q.; Zhou, W.; Wang, A.; Zhang, T., Dynamic Behavior of Single-Atom Catalysts in Electrocatalysis: Identification of Cu-N₃ as an Active Site for the Oxygen Reduction Reaction. *Journal of the American Chemical Society* **2021**, *143* (36), pp 14530-14539.
133. Stojilovic, N., Using Cu K α 1/K α 2 Splitting and a Powder XRD System To Discuss X-ray Generation. *Journal of Chemical Education* **2018**, *95* (4), pp 598-600.
134. Overa, S.; Ko, B. H.; Zhao, Y.; Jiao, F., Electrochemical Approaches for CO₂ Conversion to Chemicals: A Journey toward Practical Applications. *Accounts of Chemical Research* **2022**.
135. Zhang, X.; Guo, S.-X.; Gandionco, K. A.; Bond, A. M.; Zhang, J., Electrocatalytic carbon dioxide reduction: from fundamental principles to catalyst design. *Materials Today Advances* **2020**, *7*.
136. Ross, M. B.; De Luna, P.; Li, Y.; Dinh, C.-T.; Kim, D.; Yang, P.; Sargent, E. H., Designing materials for electrochemical carbon dioxide recycling. *Nature Catalysis* **2019**, *2* (8), pp 648-658.
137. Xiang, K.; Shen, F.; Fu, Y.; Wu, L.; Wang, Z.; Yi, H.; Liu, X.; Wang, P.; Liu, M.; Lin, Z.; Liu, H., Boost CO₂ Electroreduction towards C₂+ Products via CO* Intermediate Manipulation on Copper-based Catalysts. *Environmental Science: Nano* **2022**.
138. Xiao, H.; Cheng, T.; Goddard, W. A.; Sundararaman, R., Mechanistic Explanation of the pH Dependence and Onset Potentials for Hydrocarbon Products from Electrochemical Reduction of CO on Cu (111). *Journal of the American Chemical Society* **2016**, *138* (2), pp 483-486.
139. Ye, R.-P.; Ding, J.; Gong, W.; Argyle, M. D.; Zhong, Q.; Wang, Y.; Russell, C. K.; Xu, Z.; Russell, A. G.; Li, Q.; Fan, M.; Yao, Y.-G., CO₂ hydrogenation to high-value products via heterogeneous catalysis. *Nature Communications* **2019**, *10* (1).
140. Chang, F.; Xiao, M.; Miao, R.; Liu, Y.; Ren, M.; Jia, Z.; Han, D.; Yuan, Y.; Bai, Z.; Yang, L., Copper-Based Catalysts for Electrochemical Carbon Dioxide Reduction to Multicarbon Products. *Electrochemical Energy Reviews* **2022**, *5* (3).
141. Lees, E. W.; Goldman, M.; Fink, A. G.; Dvorak, D. J.; Salvatore, D. A.; Zhang, Z.; Loo, N. W. X.; Berlinguette, C. P., Electrodes Designed for Converting Bicarbonate into CO. *ACS Energy Letters* **2020**, *5* (7), pp 2165-2173.
142. García de Arquer, F. P.; Dinh, C.-T.; Ozden, A.; Wicks, J.; McCallum, C.; Kirmani, A. R.; Nam, D.-H.; Gabardo, C.; Seifitokaldani, A.; Wang, X.; Li, Y. C.; Li, F.; Edwards, J.; Richter, L. J.; Thorpe, S. J.; Sinton, D.; Sargent, E. H., CO₂ electrolysis to multicarbon products at activities greater than 1 A cm⁻². *Science* **2020**, *367* (6478), pp 661-666.
143. Li, T.; Lees, E. W.; Zhang, Z.; Berlinguette, C. P., Conversion of Bicarbonate to Formate in an Electrochemical Flow Reactor. *ACS Energy Letters* **2020**, *5* (8), pp 2624-2630.
144. Keith, D. W.; Holmes, G.; St. Angelo, D.; Heidel, K., A Process for Capturing CO₂ from the Atmosphere. *Joule* **2018**, *2* (8), 1573-1594.
145. Dunwell, M.; Lu, Q.; Heyes, J. M.; Rosen, J.; Chen, J. G.; Yan, Y.; Jiao, F.; Xu, B., The Central Role of Bicarbonate in the Electrochemical Reduction of Carbon Dioxide on Gold. *Journal of the American Chemical Society* **2017**, *139* (10), 3774-3783.

146. Zhang, Z.; Lees, E. W.; Ren, S.; Huang, A.; Berlinguette, C. P., Electrolytic Conversion of Bicarbonate Solutions to CO at $>500 \text{ mA cm}^{-2}$ and 2.2 V. American Chemical Society (ACS): 2021.
147. Li, T.; Lees, E. W.; Goldman, M.; Salvatore, D. A.; Weekes, D. M.; Berlinguette, C. P., Electrolytic Conversion of Bicarbonate into CO in a Flow Cell. *Joule* **2019**, *3* (6), pp 1487-1497.
148. Bonet Navarro, A.; Nogalska, A.; Garcia-Valls, R., Direct Electrochemical Reduction of Bicarbonate to Formate Using Tin Catalyst. *Electrochem* **2021**, *2* (1), pp 64-70.
149. Salmón, I.; Cambier, N.; Luis, P., CO₂ Capture by Alkaline Solution for Carbonate Production: A Comparison between a Packed Column and a Membrane Contactor. *Applied Sciences* **2018**, *8* (6), 996.
150. Li, Y. C.; Zhou, D.; Yan, Z.; Gonçalves, R. H.; Salvatore, D. A.; Berlinguette, C. P.; Mallouk, T. E., Electrolysis of CO₂ to Syngas in Bipolar Membrane-Based Electrochemical Cells. *ACS Energy Letters* **2016**, *1* (6), pp 1149-1153.
151. Kibria, M. G.; Edwards, J. P.; Gabardo, C. M.; Dinh, C. T.; Seifitokaldani, A.; Sinton, D.; Sargent, E. H., Electrochemical CO₂ Reduction into Chemical Feedstocks: From Mechanistic Electrocatalysis Models to System Design. *Advanced Materials* **2019**, *31* (31), p 1807166.
152. Garg, S.; Li, M.; Weber, A. Z.; Ge, L.; Li, L.; Rudolph, V.; Wang, G.; Rufford, T. E., Advances and challenges in electrochemical CO₂ reduction processes: an engineering and design perspective looking beyond new catalyst materials. *Journal of Materials Chemistry A* **2020**, *8* (4), pp 1511-1544.
153. König, M.; Vaes, J.; Klemm, E.; Pant, D., Solvents and Supporting Electrolytes in the Electrocatalytic Reduction of CO₂. *iScience* **2019**, *19*, pp 135-160.
154. Diaz, L. A.; Gao, N.; Adhikari, B.; Lister, T. E.; Dufek, E. J.; Wilson, A. D., Electrochemical production of syngas from CO₂ captured in switchable polarity solvents. *Green Chemistry* **2018**, *20* (3), pp 620-626.
155. Hu, W.; Li, J.; Ma, L.; Su, W.; Zhu, Y.; Li, W.; Chen, Y.; Zou, L.; Zou, Z.; Yang, B.; Wen, K.; Yang, H., Electrochemical Reduction of CO₂ to HCOOH over Copper Catalysts. *ACS Appl Mater Interfaces* **2021**.
156. Kamat, A.; Huth, A.; Klein, O.; Scholl, S., Chronoamperometric Investigations of the Electrode-Electrolyte Interface of a Commercial High Temperature PEM Fuel Cell. *Fuel Cells* **2010**, *10* (6), pp 983-992.
157. Kortlever, R.; Tan, K. H.; Kwon, Y.; Koper, M. T. M., Electrochemical carbon dioxide and bicarbonate reduction on copper in weakly alkaline media. *Journal of Solid State Electrochemistry* **2013**, *17* (7), pp 1843-1849.
158. Liu, Y.; Chen, S.; Quan, X.; Yu, H., Efficient Electrochemical Reduction of Carbon Dioxide to Acetate on Nitrogen-Doped Nanodiamond. *Journal of the American Chemical Society* **2015**, *137* (36), pp 11631-11636.
159. Min, X.; Kanan, M. W., Pd-Catalyzed Electrohydrogenation of Carbon Dioxide to Formate: High Mass Activity at Low Overpotential and Identification of the Deactivation Pathway. *Journal of the American Chemical Society* **2015**, *137* (14), pp 4701-4708.
160. De, R.; Gonglach, S.; Paul, S.; Haas, M.; Sreejith, S. S.; Gerschel, P.; Apfel, U. P.; Vuong, T. H.; Rabeah, J.; Roy, S.; Schöfberger, W., Electrocatalytic Reduction

- of CO₂ to Acetic Acid by a Molecular Manganese Corrole Complex. *Angewandte Chemie International Edition* **2020**, *59* (26), pp 10527-10534.
161. Genovese, C.; Schuster, M. E.; Gibson, E. K.; Gianolio, D.; Posligua, V.; Grau-Crespo, R.; Cibir, G.; Wells, P. P.; Garai, D.; Solokha, V.; Krick Calderon, S.; Velasco-Velez, J. J.; Ampelli, C.; Perathoner, S.; Held, G.; Centi, G.; Arrigo, R., Operando spectroscopy study of the carbon dioxide electro-reduction by iron species on nitrogen-doped carbon. *Nature Communications* **2018**, *9* (1).
162. Chen, C. S.; Handoko, A. D.; Wan, J. H.; Ma, L.; Ren, D.; Yeo, B. S., Stable and selective electrochemical reduction of carbon dioxide to ethylene on copper mesocrystals. *Catalysis Science & Technology* **2015**, *5* (1), 161-168.
163. Garza, A. J.; Bell, A. T.; Head-Gordon, M., Mechanism of CO₂ Reduction at Copper Surfaces: Pathways to C₂ Products. *ACS Catalysis* **2018**, *8* (2), pp1490-1499.
164. Wu, Z.-Z.; Zhang, X.-L.; Niu, Z.-Z.; Gao, F.-Y.; Yang, P.-P.; Chi, L.-P.; Shi, L.; Wei, W.-S.; Liu, R.; Chen, Z.; Hu, S.; Zheng, X.; Gao, M.-R., Identification of Cu(100)/Cu(111) Interfaces as Superior Active Sites for CO Dimerization During CO₂ Electroreduction. *Journal of the American Chemical Society* **2021**.
165. Zhong, H.; Fujii, K.; Nakano, Y.; Jin, F., Effect of CO₂ Bubbling into Aqueous Solutions Used for Electrochemical Reduction of CO₂ for Energy Conversion and Storage. *The Journal of Physical Chemistry C* **2015**, *119* (1), pp 55-61.
166. Sreekanth, N.; Phani, K. L., Selective reduction of CO₂ to formate through bicarbonate reduction on metal electrodes: new insights gained from SG/TC mode of SECM. *Chem. Commun.* **2014**, *50* (76), pp 11143-11146.
167. Innocent, B.; Pasquier, D.; Ropital, F.; Hahn, F.; Léger, J. M.; Kokoh, K. B., FTIR spectroscopy study of the reduction of carbon dioxide on lead electrode in aqueous medium. *Applied Catalysis B: Environmental* **2010**, *94* (3), pp 219-224.
168. Nakayama Shigeyoshi, J. S. T. R., Highly Selective Determination of Copper Corrosion Products by Voltammetric Reduction. **2016**, (82), p 97.

VITA
UDARI KODITHUWAKKU

Education

BSc, Chemistry, Physics, Zoology 2013
University of Ruhuna, Matara Sri Lanka

Master of Philosophy (M.Phil.) 2018
University of Sri Jayewardenepura, Nugegoda Sri Lanka

Professional positions

President, ECS-UK student chapter 2020-2021

Publications

Jin, J.; Habeger, R.; Yoder, T.; Coulliette, D.; Eisenhart, A.; Beck, T.; **Kodithuwakku, U.S.**; Kim, D. Y.; Benmore, C.; Hart, R.; Shafer, W. D., Molecular Structure Models of Amorphous Bismuth and Cerium Carboxylate Catalyst Precursors. *Catalysis Today* 2022.

Namal Wanninayake, Qianxiang Ai, Melonie Thomas, **Udari S. Kodithuwakku**, Md Ariful Hoque, Marcelo I. Guzman, Beth Guiton, Chad Risko, Doo Young Kim, Nitrogen and Sulfur Co-doped Carbon Nano-Onions for the Low Potential Electrochemical Conversion of Carbon Dioxide - Submitted.

Udari S. Kodithuwakku, Namal Wanninayake, Melonie Thomas, Beth Guiton, Doo Young Kim, Synergistic Interaction of Edge Nitrogen and Boron Dopants in Carbon Nano Onions for Efficient Oxygen Reduction Reaction - To be submitted.

Udari S. Kodithuwakku, Namal Wanninayake, Jacob Hempel, Yang-Tse Cheng, Doo Young Kim, Effect of Nitrogen dopant on CNO for Cu Nanoparticles and Cu-N Formation-Catalytic Activity for Oxygen Reduction Reaction - To be submitted.

Udari S. Kodithuwakku, Prakhar Sharma, Doo Young Kim, Conversion of Bicarbonate to Acetate and Formate in an Electrochemical Flow Reactor – In preparation.